Fall 1-31-2000

A mathematical model of wheelchair racing

Susan J. Schenk
New Jersey Institute of Technology

ABSTRACT

A MATHEMATICAL MODEL OF WHEELCHAIR RACING

by
Susan J. Schenk

Wheelchair racing strokes are very complicated movements, which involve a coupling between the athlete and his or her racing chair. Each body segment, as well as the wheel, follows a distinct trajectory as the motion is performed. Understanding the kinematics and kinetics of various stroke techniques would provide the athletes and their coaches with information, which could help guide the racers toward improved performances.

In this thesis, a mathematical model is developed, which is capable of providing such valuable kinematic and kinetic information. This two-dimensional model represents the body segments as a coupled pendulum system of point masses and the wheel as a distributed-mass disk. Furthermore, the model incorporates several fundamental assumptions, including that the stroke cycle can be divided into an arbitrary number of consecutive ballistic phases such that segment positions are continuous at phase boundaries.

Each phase is mathematically a second-order, nonlinear ordinary boundary value problem (BVP). Numerical methods are used to solve the BVPs independently, resulting in velocity discontinuities at the phase boundaries. These instantaneous velocity increases or decreases must be caused by impulsive forces. In turn, these impulsive forces are interpreted as muscular input and/or physical impacts.

In this research, the model is used to produce numerous stroke techniques, which are consistent with a given racer's structural parameters and prescribed stroke characteristics (racing speed, cycle time, recovery cycle time, the athlete's orientation in the racing chair, and wheel contact and release angles). The kinematics of these different techniques are contrasted. In addition, the muscular mechanical energy costs of these strokes are determined and an interpretation as to the mechanical energy efficiency of each technique is given.

The model is used to provide insight into the intricacies of an actual wheelchair racing stroke. In this thesis, the kinematics and energetics of model-produced techniques guide the analysis of these characteristics of an empirical stroke. One conclusion of this analysis is that this model may be able to provide more mechanically efficient alternative strokes from which the athlete can choose. Finally, suggestions are offered toward improving the model.

A MATHEMATICAL MODEL OF WHEELCHAIR RACING

by
Susan J. Schenk

A Dissertation
Submitted to the Faculty of
New Jersey Institute of Technology and
Rutgers, The State University of New Jersey – Newark
in Partial Fulfillment of the Requirements for the Degree of
Doctor of Philosophy in Mathematical Sciences

Department of Mathematical Sciences, New Jersey Institute of Technology
Department of Mathematics and Computer Sciences, Rutgers – Newark

January 2000

APPROVAL PAGE

A MATHEMATICAL MODEL OF WHEELCHAIR RACING

Susan J. Schenk

Dr. H. Michael Lacker, Thesis Advisor — Date
Professor, Department of Mathematical Sciences, NJIT

Dr. John Bechtold, Committee Member — Date
Associate Professor, Department of Mathematical Sciences, NJIT

Dr. Denis Blackmore, Committee Member — Date
Professor, Department of Mathematical Sciences, NJIT

Dr. Ellen Ross, Committee Member — Date
Associate Professor of Clinical Physical Therapy, UMDNJ

Dr. Michael Siegel, Committee Member — Date
Associate Professor, Department of Mathematical Sciences, NJIT

BIOGRAPHICAL SKETCH

Author: Susan J. Schenk

Degree: Doctor of Philosophy

Date: January 2000

Undergraduate and Graduate Education:

- Doctor of Philosophy in Mathematical Sciences,
  New Jersey Institute of Technology, Newark, NJ, 2000

- Master of Science in Mathematics,
  Stevens Institute of Technology, Hoboken, NJ, 1991

- Bachelor of Science in Mathematics,
  Stevens Institute of Technology, Hoboken, NJ, 1990

Publications:

Redling, J. D., S. J. Schenk, S. A. Sisto, L. M. Studer, and H. M. Lacker. submitted June 1999. "An Overview of Mathematical Models of Human Movement: Inverse and Forward Dynamics." *Gait & Posture.*

Schenk, S., W. Roman, R. Narcessian, M. Lacker, J. Redling, S. A. Sisto, and M. Gerdes. 1998. Abstract: "Mechanical Energy Efficiency of a Wheelchair Racing Stroke." *Gait & Posture.* 7: 152.

Lacker, H. M., T. H. Choi, S. Schenk, B. Gupta, R. P. Narcessian, S. A. Sisto, S. Massood, J. Redling, P. Engler, F. Ghobadi, and V. K. McInerney. 1997. Abstract: "A Mathematical Model of Human Gait Dynamics." *Gait & Posture.* 5: 176.

Presentations:

Schenk, S. "A Mathematical Model of Human Motion," *Essex County College BioSeminars.* Newark, NJ, October 1998.

BIOGRAPHICAL SKETCH
(continued)

Schenk, S., W. Roman, S. A. Sisto, H. M. Lacker, L. Studer, R. Narcessian, and M. Gerdes. Poster: "A Mathematical Model of Wheelchair Racing", Emerging Technologies: New Frontiers in Medical Rehabilitation. West Orange, NJ, September 1998.

Schenk, S., W. Roman, R. Narcessian, M. Lacker, J. Redling, S. A. Sisto, and M. Gerdes. "Mechanical Energy Efficiency of a Wheelchair Racing Stroke," *North American Society of Gait and Clinical Movement Analysis, 3rd Annual Meeting.* San Diego, CA, April 1998.

Schenk, S. "A Mathematical Model of Human Gait," *Essex County College Convocation Activity Presentation.* Newark, NJ, August 1997.

Schenk, S., and H. M. Lacker. "A Two-Dimensional Model of Human Walking," *Fourth SIAM Conference on Applications of Dynamical Systems.* Snowbird, UT, May 1997.

Schenk, S. "A Model of Human Gait," *Essex County College Department of Mathematics and Physics Seminar.* Newark, NJ, April 1997.

This thesis is dedicated to Zoey

ACKNOWLEDGMENT

I would like to express my appreciation to many people who offered support toward the production of this research. First, I must acknowledge the significant contribution and guidance provided by my advisor and committee members. Thank you Michael Lacker, John Bechtold, Denis Blackmore, Michael Porter, Ellen Ross, and Michael Siegel. Your input was crucial to the completion of this work.

Second, I would like to express my gratitute to everyone in the HPMAL at KMRREC. Specifically, thanks to Sue Ann Sisto, Bill Roman, Theresa D'Errico, and Matt Gerdes for providing assistance and enthusiasm, which was invaluable to me as I proceeded with my research. Also, thanks to the Eastern Paralyzed Veterans Association for providing funds toward the wheelchair racing study at KMRREC.

Third, I must appreciate my colleagues and the students at Essex County College. I am very lucky to be associated with such wonderful people and to work in such a caring environment. Special thanks go to Tim Stafford, Ray Zenere, and many former students for all their interest and motivation.

Last, but by no means least, I must acknowledge my friends and family members for offering me encouragement through this long journey. I am blessed by having such strong, supportive people in my life. You are too many to name, but you know who you are. Thanks.

TABLE OF CONTENTS

TABLE OF CONTENTS
(continued)

TABLE OF CONTENTS
(continued)

TABLE OF CONTENTS
(continued)

LIST OF TABLES

LIST OF FIGURES

LIST OF FIGURES
(continued)

Figure **Page**

LIST OF FIGURES
(continued)

Figure **Page**

LIST OF FIGURES
(continued)

Figure **Page**

CHAPTER 1

INTRODUCTION

1.1 Purpose of Proposed Work

Many people are interested in the science of human motion, including surgeons operating on those who have movement difficulties, physical therapists who assist patients undergoing rehabilitation, coaches who guide athletes to maximal performance, and others. A model of human motion, which is able to analyze accomplished motions and possibly predict optimal motions, would be of great benefit to these people.

If *better* movements could be determined, surgeons would be certain that the procedures they were about to perform would produce desired results: for example, whether performing surgery to lengthen the hamstring muscles in a child with cerebral palsy would enable the child to walk more stably. In addition, physical therapists would know in what direction a client undergoing rehabilitation should be directed: for example, teaching a post-operative knee surgery patient how to walk so that minimal forces and moments are produced at the affected knee. Furthermore, coaches could train athletes to produce optimal sport performances: for example, training an athlete to use a wheelchair racing stroke that consumes the least amount of mechanical energy per unit distance traveled.

In order to address these situations and others, researchers have made numerous attempts at modeling all different types of human motion (Beckett and Chang 1968, Cooper 1990, Hatze 1977, Mochon and McMahon 1980, Siegler, Seliktar, and Hyman

1982). At present, it seems that there are two distinct approaches followed to model movement: that which employs the inverse dynamics method and that which is based on forward (direct) dynamics. In fact, most existing models seem to be based on inverse dynamics (Winter 1984).

Inverse models ultimately determine the forces needed to cause a given motion; that is, given the actual movement, the forces are found ($m\vec{a} = \vec{F}$). They require a performed motion – specific locations of each body segment as functions of time – as input. This input is easily obtained in a laboratory by using a motion analysis system, which records segment locations via camera measurements sampled at a prescribed frequency. Velocities and accelerations can then be calculated using finite difference schemes on the provided segment locations at each instant. Equations provided by Newton's Second Law of Motion (in both linear and angular forms) use these segment accelerations, along with measured ground reaction forces and moments, to determine joint reaction forces and moments at each joint in the body. One significant limitation of inverse modeling is that because it requires detailed motion as input, it cannot be used to predict new possible movements. That is, it can only compare existing (performed) movements. Therefore, it is inappropriate to use inverse modeling if the goal is to predict *optimal*, or even *better*, motions.

Forward models, on the other hand, determine the motion that results when given forces are applied to a mechanical system; that is, given the acting forces, the motion is found ($\vec{F} = m\vec{a}$). The clear advantage of this approach is that it can be used to predict new motions. However, this technique is not easy to use because there are no straightforward means of measuring forces applied to the segments (including joint

reaction forces). In fact, the authors of one textbook on human gait state that, "The direct measurement of the forces and moments transmitted by human joints, the tension in muscle groups, and the activation of the peripheral and central nervous systems is fraught with methodological problems. That is why we in gait analysis have adopted the indirect or inverse approach." (Vaughan, Davis, and O'Connor 1992)

The descriptions of each modeling approach given above emphasize that, if the goal is to predict *better* motions, a new method of modeling must be developed. The model described in this thesis is such a model. In order to allow for motion-predicting capabilities without requiring forces as input, this model employs an alternative to forward and inverse approaches, namely, the *boundary-point* method, which was first utilized by Lacker *et al.* (1997).

The basic idea behind the boundary-point approach is that the motion to be modeled can be approximated as a small number of consecutive *ballistic phases*. Mathematically, each phase is a two-point boundary value problem consisting of the following elements:

- equations of motion determined by the Lagrangian dynamics approach
- the positions and orientations of the body segments at an initial time (the initial configuration)
- the positions and orientations of the segments at a final time (the final configuration)
- the phase duration

Each phase is ballistic in that only gravitational forces and joint viscous forces act on the system for the duration of the phase. This means that muscle forces are *not* present during the phases. As will be explained shortly, in the boundary-point method muscle activity occurs only at the interface times separating contiguous phases. Therefore, claiming that a small number of phases will capture the essence of the motion to be modeled means then that the muscles need be active only at a few salient instances throughout the motion. If these few prescribed times and configurations could be identified, then the remainder of the motion could be accomplished without additional muscle activity but rather by the natural spontaneous flow of physical momentum and energy between pendular segments and the gravitational field. If this is the case for mechanically energy efficient solutions to a desired movement task, the boundary method may be useful to find these optimal motions, the associated salient times and configurations, and the net muscle input required to accomplish them.

Also note that, because body configurations are required only at two distinct times of each phase, it is not necessary to input an *entire* motion to the model, as is the case in inverse modeling. In this way, the model can be used in a predictive capacity, as it will need to establish the segment configurations at all time steps between the given initial and final times of each phase, and thus will produce a new motion.

Each phase's boundary value problem is solved independently via a shooting and/or relaxation method routine, which requires preliminary guesses of the initial velocity or the dynamic trajectory of each segment, respectively. Because each phase's solution is found independently, segment velocities will not be continuous at the boundary of consecutive phases, despite the fact that segment positions will match here in

order for the entire motion to be continuous. These model-output velocity discontinuities correspond to instantaneous changes in momentum at the phase boundaries, which in turn must be produced by impulsive forces. Muscular activity and/or the imposition of a constraint produce these impulsive forces. Thus, muscles are active only at the phase boundaries.

Varying the phases of a motion by changing initial configurations, final configurations, and/or durations will produce different model solutions (that is, possible movements). Evaluating each of the model solutions in terms of a specified characteristic might help indicate a *best* solution. For example, a number specifying the consumption of mechanical energy by the body segments per unit distance traveled of each model-found wheelchair racing motion can be used to designate which of these strokes is most mechanical energy efficient.

In this dissertation, a model is developed, which is based on the two-dimensional model proposed by Lacker (1997) that has been used primarily in gait and lower-body motion analysis. Lacker's model is expanded upon in this thesis. The extended model is then applied to upper-body motion, namely wheelchair racing, a relatively unexplored area of human movement. Model-generated solutions are presented and compared to analyses of actual wheelchair racing stroke techniques. Furthermore, the model's capability to identify the *best* wheelchair racing stroke when only a few of the model parameters are varied (the upper arm angle at a given variable time in the recovery phase and the maximal elbow angle attained during the recovery phase) is investigated in this research.

1.2 Outline of Proposed Work

The model in this research is restricted to two dimensions and is, therefore, a first approximation. By ignoring motion outside of the plane, the results of the model will compare most favorably with actual wheelchair racing strokes that are dominantly planar in nature. One such racing technique is the *piston stroke*, so named for its likeness to a mechanical piston. In contrast, the *butterfly stroke*, which resembles the butterfly stroke in swimming, is characterized by significant excursions outside the plane (that is, having considerable abduction/adduction components). Therefore, model output is compared to experimental data of piston strokes and not butterfly strokes.

Assuming symmetry in the wheelchair racing stroke allows the model to consider only one side of the upper body. This specified side of the upper body is represented in this model by a multi-segment (n-coupled) pendulum system. The linked pendulum system consists of body segments represented as point masses and a wheel segment modeled as a uniform, distributed-mass disk.

The equations of motion used in this model are written in a very general form, which allows for the inclusion of n segments, where n is a specified integer. This makes it possible to effortlessly adjust the model for different spinal-cord-injured individuals with diverse functionalities. For example, a wheelchair racer with a high level spinal cord injury, who has virtually no muscular control of his trunk, is modeled with a triple pendulum system ($n = 3$) where one pendulum represents the upper arm, one is the forearm, and the other is the wheel. On the other hand, an athlete with a lower level injury, who has more use of his trunk, is described with a four-coupled system ($n = 4$), where the additional segment is the trunk. In both cases, the model automatically produces appropriate equations of motion.

One of the fundamental assumptions of the model is that muscle impulsive forces are present only at the onset of each defined phase of the motion, and therefore, provide the initial velocities to the body and wheel segments. This means that muscle forces act *only* at the beginning of each phase. The segments then move through the rest of each phase without any muscle input, making the only active forces during these intermediate times those due to gravity and joint viscosities. (Joint reaction forces, ground reaction forces, and, in general, forces that maintain implicit system constraints are not used in the Lagrangian method.) Clearly this is not quite realistic because muscles are active continuously throughout an entire motion. Fortunately, experimentally-collected electromyographic (EMG) data offers insight as to the times in the motion where the muscles are most active. This corresponds to how the motion should be divided into phases when the model is developed in order to agree with this primary assumption in a first-approximation sense. Thus, EMG data must be collected on the upper body while performing a piston wheelchair racing stroke.

Other experimental data helpful to the model is segment path data (positions of each segment as a function of time) collected with a VICON 370 Motion Analysis System. This data can be used to prescribe the necessary segment initial and final configurations and the durations of the phases. As mentioned above, this experimental data is analyzed to determine whether the motion in question is predominantly planar for a given stroke technique and can therefore be captured for the most part by a two-dimensional analysis. Experimental data is also compared with theoretical model output in order to confirm the validity of the model. For these reasons, VICON data of the appropriate upper body segments and the wheel must be collected for a piston stroke.

Some parameters present in the model's equations of motion include measurable anthropometric (body structure) data and structural racing wheelchair data. The lengths of all included segments (upper arm, forearm, etc.) are taken on the athlete being modeled. The masses and the locations of the centers of mass of the segments are determined from tables generated by cadaver studies (Dempster 1955) or from shape-dependent formulae. The wheel's full radius and pushrim radius, along with its mass, are measured too. The viscosity of the wheel as a function of its velocity is found by performing a simple experiment in which the wheel is allowed to slow from a given speed and VICON data is collected. The decrease of wheel velocity as a function of time is a measure of its viscosity.

In order to investigate the model's capability of identifying an energy-efficient stroke technique, the model is then used to produce numerous different wheelchair racing strokes. The mechanical energy cost to the body segments per unit distance traveled, an approximation of required net muscle force input, is determined for each stroke technique. Mechanical energy not supplied by muscular forces, *impact energy loss*, is lost at various instances during the racing stroke cycle, including the following:

- at the ends of joint ranges of motion – when the arm segments are positioned so that their included joint is at its extreme range of motion causing an inelastic collision
- at pushrim impact – when the hand lands on the wheel's pushrim at the onset of the *push period* causing an inelastic collision

Mechanical energy cost per unit distance traveled is defined as the quotient of the muscular mechanical energy cost, that is the amount of mechanical energy that the body (muscles) must supply in order to perform a given stroke cycle, and the distance covered during one stroke. This muscular mechanical energy cost is found by adding the absolute value of all impulsive changes in mechanical energy throughout one stroke cycle, which are not impact energy losses. The distance traveled is determined by first finding the cycle's change in wheel angle, $\Delta\theta$, and then multiplying by the ratio of the wheel circumference and 360°. Since wheel viscosity is assumed to be constant, $\Delta\theta$ can be calculated.

Finally, model output strokes are compared as to their mechanical energy costs per unit distance and their impact energy losses, as well as to an elite wheelchair racer's actual stroke. An interpretation of energy efficiency of wheelchair racing techniques is offered.

Once the proposed work outlined above is completed, it will provide several original contributions to the fields of motional analysis and applied mathematics. Specifically, new information that is offered by work contained in this thesis includes the following:

- the limitations caused by the two-dimensional nature of the model are established
- the model is used in an inverse fashion to calculate the muscular mechanical energy cost of a performed wheelchair racing stroke

- model output is used to guide the biomechnical analysis of an actual stroke technique
- both coupled *and* uncoupled motion of components of the athlete/chair system are modeled
- a geometric derivation of the equations of motion of the system and the projection theorem (when constraints are imposed) is given
- improvements upon the shooting method boundary-value-problem solving technique are made

CHAPTER 2

PREVIOUS WORK DONE

The significant amount of work published examining the biomechanical and physiological characteristics of many different types of human movement has been reviewed (Winter 1984). Some researchers have even studied the mechanics of standard wheelchair propulsion via inverse modeling (Boninger *et al.* 1997, Coutts 1990, Hofstad and Patterson 1994, Rao *et al.* 1996, Robertson *et al.* 1996, Ruggles *et al.* 1994, Sanderson and Sommer 1985, Shimada *et al.* 1998, van der Woude *et al.* 1989, Vanlandewijck *et al.* 1994, and Veeger *et al.* 1989). To a lesser extent, wheelchair racing technique has been investigated through inverse models (Higgs 1984, Ridgway *et al.* 1988, van der Woude *et al.* 1988, and Wang *et al.* 1995). A large majority of this literature seems to report analyses of experimental data via inverse modeling. A four-link kinematic inverse model is often used.

The most cited wheelchair propulsion kinematic analyses are those of Higgs (1984), Ridgway *et al.* (1988), and Sanderson and Sommer (1985). These researchers and several others (Boninger *et al.* 1997, Coutts 1990, Rao *et al.* 1996, Ruggles *et al.* 1994, Shimada *et al.* 1998, van der Woude *et al.* 1988 and 1989, Vanlandewijck *et al.* 1994, Veeger *et al.* 1989, and Wang *et al.* 1995) applied inverse models to experimental data to describe wheelchair propulsion characteristics including motion patterns, segment and joint kinematics, cycle timing parameters, and some joint kinetics. Robertson, Boninger, Cooper, and Shimada (1996) used an inverse solution with a Newton-Euler method and a back propagation algorithm in order to calculate net joint reaction forces and moments involved in propelling a standard (non-racing) wheelchair. An abstract by

Rodgers, Tummarakota, Lieh, and Schrag (1994) described a model employing the Newton-Euler method on a three-rigid-segment system, which used a recursive inverse dynamics approach to investigate standard propulsion. Some of the above-mentioned studies (Sanderson and Sommer 1985, Shimada *et al.* 1998, and Veeger *et al.* 1989) have tried to compare propulsion techniques, but these works are limited in that they only remark differences and offer hypotheses as to why these disparities exist. These authors have emphasized the need for more research in this area.

Cooper (*J. Rehab. Res. Dev.* 1990) modeled wheelchair racing by using a systems approach (Newton's method), which is in turn dependent on determining joint torques and forces via inverse dynamics. Hofstad and Patterson (1994) attempted to improve on Cooper's models by determining which environmental effects were insignificant and could, therefore, be neglected in the calculations. Their modified model equated force with both acceleration and the resistance terms due to the environment. These modifications permitted the use of simplified linear, first-order differential equations. The addition of wheelchair acceleration and velocity as model input consequently enabled the model to predict force output. This is again an inverse modeling approach, relying on experimental data. Cooper (*IEEE* 1990) later reported some results on optimizing the forces and energy associated with the wheelchair stroke by representing force as the control variable and energy as the constraint in an optimal control problem.

The model in this thesis is based on the model of human gait developed by Lacker and colleagues (1997). Lacker's model blended concepts from Mochon's and McMahon's gait model (conservative ballistic swing phase – both swing and stance legs, Mochon and McMahon 1980) and Beckett and Chang's gait model (nonconservative

swing phase – swing leg only, Beckett and Chang 1968). Lacker also included the effect of joint viscosities on the swing phase of gait. In his doctoral dissertation, Choi (1997) extended Lacker's model to include the double support phase of gait, which along with the existing swing phase, accounted for the entire walking motion.

CHAPTER 3

PROCEDURE FOR THE COLLECTION AND PROCESSING OF EXPERIMENTAL DATA

3.1 Data Collection

3.1.1 The VICON Motion Analysis System

Data is collected in the Human Performance Motion Analysis Laboratory at Kessler Medical Rehabilitation Research and Education Corporation in West Orange, New Jersey. The lab is equipped with an Oxford Metrics Ltd. VICON 370 Motion Analysis System, which is an instrument specifically designed to record human motion. The device consists of a six-camera/computer setup, as well as retroreflective spherical markers, which are adhered to the subject's body at desired locations. The six cameras, positioned at various points around the lab space, are first calibrated to recognize a known, marked-off volume and origin point in the lab. Once this calibration is completed, the cameras are able to generate (x,y,z)-coordinates for the locations of the markers at each recorded time frame. In this experiment, VICON was set to collect data at a frequency of 120 Hertz.

The athlete, seated in his racing chair, is positioned on an inertial-roller system called a CompuTrainer, which is described in the next section. A total of fourteen markers are taped onto the individual at the palpable anatomical locations indicated in Figure 3.1. All markers except C7 and L5 are on both the left and right sides of the body.

C7	seventh vertebrae of cervical spine	MEP	medial epicondyle of humerus
L5	fifth vertebrae of lumbar spine	RAD	radius
TUB	greater tubercle of humerus	ULN	ulna
LEP	lateral epicondyle of humerus	MET1	the first metacarpal

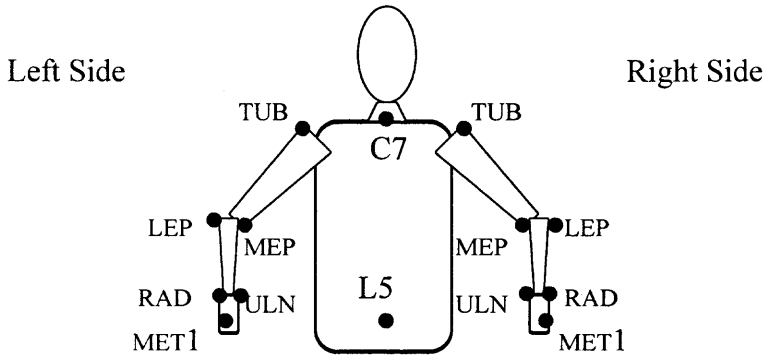

Figure 3.1 Location of the VICON markers on the wheelchair racer (as seen from behind with palms facing into the page)

As can be seen in Figure 3.1, the markers are used to define the body segments. For data analysis, all body segments are idealized as point masses or as rigid bodies (frustrums). Both the trunk and the sagittal plane are created by C7, L5, and the average of the tubercle markers. The upper arm is obtained from the tubercle, the lateral epicondyle, and the medial epicondyle. The forearm is defined by the lateral epicondyle, the medial epicondyle, the radius, and the ulna. The hand is created by the radius, the ulna, and the first metacarpal. These definitions of body segments are summarized in Table 3.1.

Table 3.1 Definition of the body segments by the VICON markers

Body Segment	**Markers**
Trunk and Sagittal Plane	C7, L5, Average of left and right TUB's
Upper Arm	TUB, LEP, MEP
Forearm	LEP, MEP, RAD, ULN
Hand	RAD, ULN, MET1

In addition, two markers are placed on each wheel. One is adhered to the wheel hub and the other is taped onto the wheel itself. (The wheel is a solid disk.) The distance between the hub marker and the marker on the wheel is measured.

VICON records the *x*-, *y*-, and *z*-positions (relative to the lab, or *global*, coordinate axes) of the centers of the spherical markers as the athlete races his wheelchair. Each measurement is accurate to within a few millimeters (VICON 1998), and the data is filtered to remove noise and reflection artifacts. Data is actually captured for only a few seconds of the entire trial once the motion is steady. Because the athlete races at roughly eight meters per second and VICON records coordinates at the speed of 120 frames per second, each data capture will contain several stroke cycles.

Identifying one complete racing stroke cycle is possible by analyzing recorded VICON data. In this thesis, a cycle is defined from wheel contact to wheel contact. As a first approximation, assume that the wrist joint center (the average of the RAD and ULN

markers) is the part of the athlete's body that makes contact with the pushrim. During push, the wrist center remains on the pushrim, which is a fixed distance from the wheel hub. Mathematically, this means that the distance between the wrist joint center and the hub is constant during push.

The information presented in Figure 3.2 is based on experimentally recorded VICON data. Figure 3.2 graphs the wrist-hub distance of the empirical data. Circled in the figure are the first push period and the next push period, which last from VICON frame 55 to 59 and frame 113 to 117, respectively. Thus, one complete cycle is approximately from frame 57 to 115. This cycle will be referred to as *Piston Cycle 1* for the remainder of this thesis.

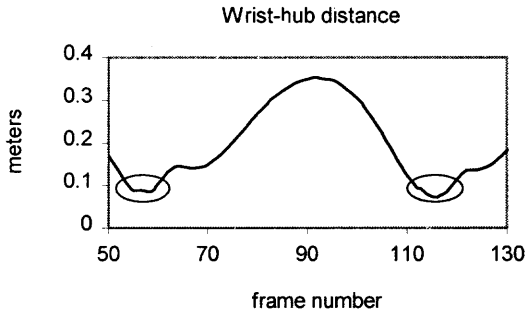

Figure 3.2 The wrist-hub distance of empirical VICON data

3.1.2 The CompuTrainer Inertial-Roller System

To simulate road-racing conditions, a CompuTrainer setup is used. The racing chair is positioned so that its wheels sit on top of inertial rollers, and the athlete/chair system, therefore, does not translate in the lab. This means that there will be no translational kinetic energy present in the athlete/chair system, only rotational kinetic energy.

The rollers can be programmed to simulate the effect of resistance. It is necessary to determine how much frictional dissipative force acts to slow down the wheel in the experimental setup. To quantify the effect of wheel friction, a simple experiment is performed where the moving wheel is allowed to slow down on its own. The results of such a trial are depicted below in Figure 3.3.

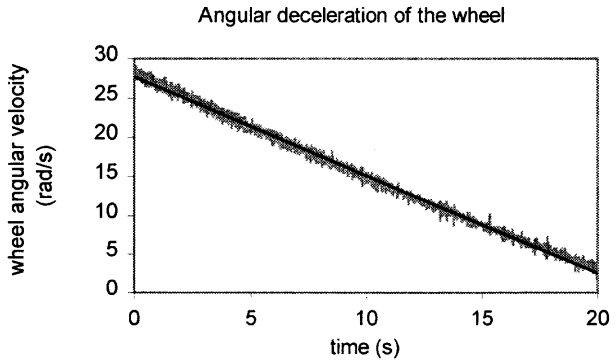

Figure 3.3 The angular deceleration of a racing chair wheel on the CompuTrainer

Note that the wheel is decelerating linearly at a constant rate of 1.26 rad/s^2, which is approximately 72.19 degs/s^2. Mathematically, this is expressible as the following second-order, linear ordinary differential equation: $\ddot{\theta}_{wh} = -72.19$. Solving this equation produces expressions for the wheel velocity and the wheel angle as functions of time, respectively given in Equations 3.1 and 3.2.

$$\dot{\theta}_{wh}(t) = -72.19t + \dot{\theta}_{wh}(0) \tag{3.1}$$

$$\theta_{wh}(t) = \frac{1}{2}(-72.19)t^2 + \dot{\theta}_{wh}(0)t + \theta_{wh}(0) \tag{3.2}$$

3.1.3 Electromyography

Electromyography (EMG) data is recorded during the experiment. Electromyography is the recording of electrical signals, which accompanies the chemical stimulation of muscle fibers. These signals can be analyzed to determine the timing and relative intensity of the muscular effort. Upper quadrant muscle activity is determined using surface electrodes in standard muscle belly-tendon configurations wherever possible. The exceptional muscle definition of the wheelchair athlete is exploited to identify and standardize suitable electrode placements for those muscles, which have traditionally been difficult to characterize using surface electromyography.

The sternal portion of the pectoralis major, the anterior, middle and posterior portion of the deltoids, middle trapezius, supraspinatus, infraspinatus, biceps brachii, and triceps brachii are all investigated in this research. For filtering purposes, five seconds of EMG data is collected to determine background noise prior to the wheelchair racing trial while the subject is at rest. The noise check is followed by the collection of EMG activity (coincident with VICON data capture) during the wheelchair racing.

3.1.4 The Entire Experimental Setup

A photograph of an actual data collection session is found below in Figure 3.4. During this trial, VICON, EMG, and maximal VO_2 intake data were being recorded.

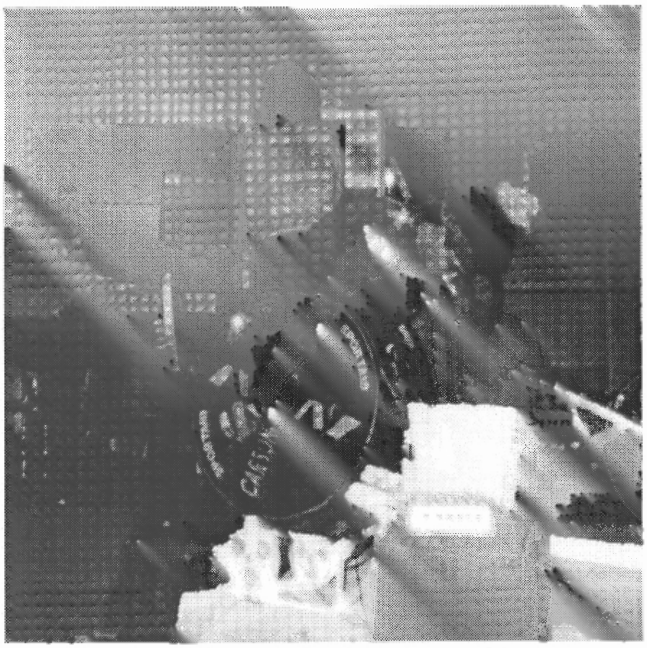

Figure 3.4 An actual trial of data collection where VICON, EMG, and VO_2 intake are being collected

3.2 Processing of Data

3.2.1 Filtering

Recording human motion by using the VICON Motion Analysis System described in Section 3.1.1 involves sampling a continuous motion at a given frequency (120 Hertz) to produce a discrete sequence of marker spatial positions. In doing so, there are several possible sources of distortion to the collected data. One source of error is the accuracy limitations of the VICON cameras. Another is noise in the signal received by the VICON cameras. One common example of such noise is when the position of a marker's reflection is identified, as opposed to the actual marker's location. Whatever the source of error, as much of it as possible should be removed before the data is analyzed.

A lot of this error can be removed by filtering the data. In order to determine an appropriate filter, the *spectrum* of the collected data must be reviewed. According to basic signal processing theory (Kuc 1988), the distinguishing characteristics of a signal are most easily interpreted in the frequency domain. A Fourier transform of a data sequence produces its spectrum and, in doing so, defines the frequency content of the signal. To determine the frequency contents of the raw VICON data, fast Fourier transforms (*ffts*) are applied to the x-position data of the markers, the y-position data of the markers, and the z-position data of the markers separately. A typical spectrum of raw VICON x-position data of all markers is given in Figure 3.5.

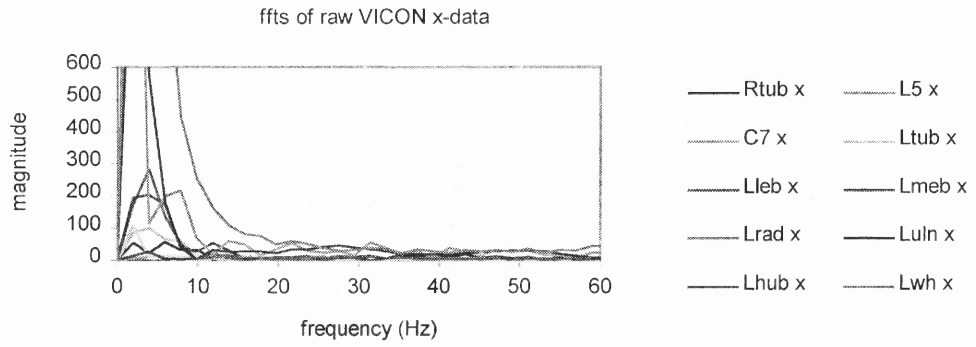

Figure 3.5 The spectrum of typical raw VICON x-position data

Once the x-data, y-data, and z-data *ffts* are obtained for a given set of raw VICON data, the cutoff frequency (ω_c) of each must be decided upon. Cutoff frequencies are used to determine how to filter the data. First the spectrum of the x-data is reviewed to see in what frequency range most of the signal lies. Since the data collected in this

research is low-frequency data, the filtered range will be from 0 to ω_c Hertz. For the data collected in this thesis, cutoff frequencies typically are between eight and fourteen Hertz.

A *second-order, lowpass digital Butterworth filter* is then applied to the raw x-data, which causes the frequency components in the raw data from zero to the ω_c to be passed through the filter unaffected, while the higher frequencies are eliminated. This will remove any high-frequency noise or instrumentation error from the VICON x-data. This filtered VICON position x-data will be smoother than the raw x-data and will be used for analysis purposes. The y-data and z-data also undergo this whole process of filtering. Figure 3.6 illustrates the affect of filtering on the raw VICON data.

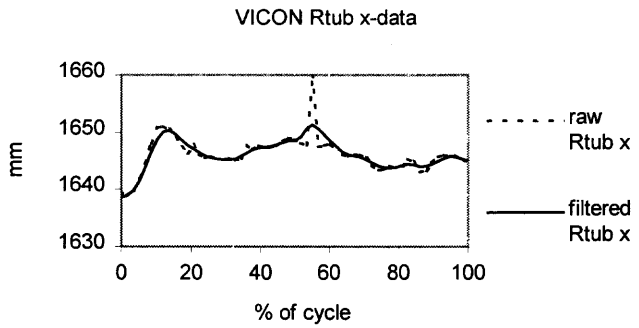

Figure 3.6 A comparison of VICON x-position data of the right tubercle marker in its raw form and its filtered form (with ω_c = 12 Hertz)

3.2.2 Projecting VICON Data into Two Dimensions

The three-dimensional VICON data is projected into the sagittal plane of the athlete to make it two-dimensional. This allows for the comparison of actual motion to model output. Since the CompuTrainer/athlete is set up in the direction of the lab's x-axis, the

projected data is more or less parallel to the lab's *xz*-plane. (Because of slight tilting of the athlete, the sagittal plane is not *exactly* parallel to the lab's *xz*-plane.) The algorithm implemented in this thesis to project the three-dimensional data into the sagittal plane is explained in detail in Section 5.2.

CHAPTER 4

OUTLINE OF THREE-DIMENSIONAL VICON DATA ANALYSIS (INCLUDING INVERSE MODELING)

4.1 A Brief Overview of VICON Data Analysis

Once filtered VICON data is obtained on a wheelchair racing athlete, data analysis is carried out on the collected data. It is assumed that the body, the chair, and the stroke technique are symmetric allowing for the consideration of only one side of the body. Mathematical analysis of filtered kinematic data provides the anatomical joint angles, the pushrim contact angle, and the mechanical energy in the system throughout the performed stroke cycle. These stroke characteristics are used to provide evidence that two-dimensional mathematical modeling is able to capture the dominant characteristics of this truly three-dimensional motion and will also contribute insight as to what exactly happens during a racing stroke cycle.

Furthermore, inverse modeling is capable of determining the net joint reaction forces and moments present throughout an observed stroke cycle. Input required by inverse modeling consists of basic anthropometric parameters and wheelchair structural characteristics, as well as the kinematics of the entire stroke cycle and the pushrim contact forces and moments acting during push.

4.2 Structural Parameters

Required parameters for analyzing performed motions, as well as for modeling new motions, include structural measurements of both the body segments and the wheelchair.

Throughout this chapter, the wheel segment is represented as a solid disk. However, the body segments are presented in two different ways, namely as point masses or as distributed masses. Therefore, the following two alternative models are being considered here: the *point-mass body segment / disk wheel* system and the *distributed-mass body segment / disk wheel* system.

Regarding anthropometric data, segment masses and lengths are needed in both model cases indicated above. Moreover, locations of the centers of mass are needed for point-mass body segments, whereas the proximal and distal radii of each body segment are required when distributed masses are being considered. The distributed mass model assumes each segment to be an appropriate frustrum. These radii enable the calculation of a segment's center of mass location, as well as its moments of inertia.

The most easily obtained of these required parameters are the segment lengths and radii, which can be found simply by measuring them on the individual whose motion is being examined. Of course, the masses of the segments cannot be obtained in such a straightforward manner, as it is impossible to weigh each piece of the body separately. However, previous research studies on cadavers (Dempster 1955) provide these numbers by supplying each segment's percentage of the subject's total body mass. Such research also furnishes the location of the center of mass of each body part. Listed below, in Table 4.1 are these data for the upper body segments. In Table 4.2, the necessary anthropometric data is given for the athlete whose motion is being modeled in this research.

Table 4.1 Anthropometric data on mean segments' percents of body mass and locations of centers of mass (Dempster 1955)

Body Segment	Percent of Total Body Mass	Location of Center of Mass (% from proximal end of segment)
Head/Neck	7.9	43.3
Trunk	56.5	60.4
Upper Arm	2.7	43.6
Forearm	2.2	43.0
Hand	0.6	50.6

Table 4.2 Structural body segment parameters for the left side of the wheelchair racer modeled in this dissertation

Body Segment	Mass (kg)	Length (m)	Location of Center of Mass (m) (from the proximal end)	Proximal Radius (m)	Distal Radius (m)
Upper Arm	2.077	0.275	0.120	0.054	0.042
Forearm	1.692	0.253	0.109	0.038	0.029

In addition, information about the wheelchair must be known. There are two possible wheelchair racing circumstances, namely that which occurs under experimental (lab) conditions, as well as that which takes place under actual, road-racing conditions. As mentioned in the previous chapter, experimental data collection was done on a CompuTrainer inertial-roller device. In this case, the only wheelchair components that move and are, therefore, considered dynamic in both data analysis and modeling are the wheels. This is because the rest of the racing wheelchair apparatus is held fixed in place by the CompuTrainer and does not contribute to the overall motion of the athlete/wheelchair system. In this case, the needed structural parameters, namely the wheel's mass, full radius, and pushrim radius and the mass of the entire racing wheelchair, are readily measurable.

On the other hand, road-racing conditions necessitate the inclusion of the entire racing chair, which impacts on the motion of the athlete/wheelchair system. In this case, the overall design of the chair is important. A simplified diagram of a typical racing chair is given in Figure 4.1. Some of the important structural parameters are given in Table 4.3.

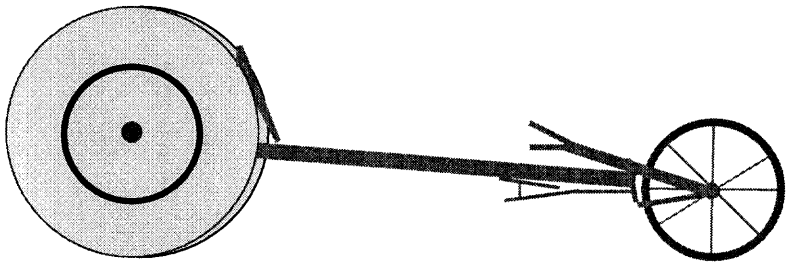

Figure 4.1 A simple illustration of a typical racing wheelchair

Table 4.3 Structural parameters for the racing chair modeled in this dissertation

Wheel Mass (kg)	Wheel Full Radius and Pushrim Radius (m)	Chair Mass (kg)	Racing Chair Length (m)
1.538	0.328 0.191	3.167	1.74

4.3 Angle Calculations

Throughout the racing stroke cycle, the angular orientation of a given segment can be described relative to a fixed coordinate system or else relative to another specified segment. In the latter case, the segment's position is explained in terms of defined planes of the body by stating anatomical joint angles. Human motion professionals frequently use anatomical joint angles to describe body segment movement while performing a prescribed task. Furthermore, the interaction between the athlete and the racing chair during the stroke's push phase can be described by the pushrim contact angle.

4.3.1 Anatomical Joint Angles

Anatomical joint angle measurements, often of interest to clinicians, provide information concerning the motion involved in completing a prescribed task. These joint angles can be of use in comparing wheelchair racing stroke techniques. They will also be helpful in determining how planar (two-dimensional) a given experimentally performed stroke is, and therefore, provide some insight as to what extent two-dimensional model output will be comparable to empirical data.

Most joints allow for some degree of movement of attached segments relative to one another. This movement is often described by referring to the three basic anatomical planes. These planes are as follows: the sagittal, the frontal (or coronal), and the transverse (horizontal). Figure 4.2 illustrates these planes.

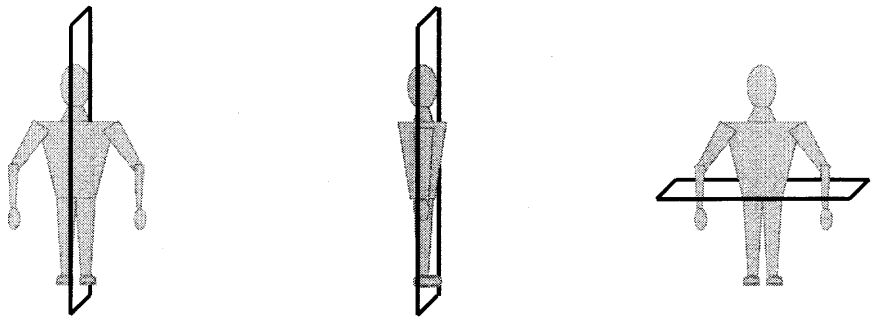

Figure 4.2 The three anatomical planes of the body

In modeling the athlete used in this research, the body segments included are the upper arm and the forearm. Therefore, the joints considered will be the shoulder joint and the elbow joint. The shoulder connects the trunk (proximal segment) with the upper arm (distal segment). The elbow attaches the upper arm (proximal segment) and forearm (distal segment). The movement capabilities of these two joints are discussed below (Nordin and Frankel 1989).

For the shoulder joint, *flexion* is defined as movement of the upper arm away from the trunk in the sagittal plane. *Extension*, where the motion brings the upper arm closer to the trunk, is the opposite of flexion in the sagittal plane. Shoulder *abduction* is movement of the upper arm away from the trunk in the frontal plane. *Adduction* is the

opposite of abduction, in which motion is toward the trunk in the frontal plane. (Flexion and abduction are considered positive and extension and adduction are negative.) Lastly, motion occurring about the long axis of the upper arm is known as *internal* (positive, toward the trunk) or *external* (negative, away from the trunk) *rotation.*

The elbow joint is hinge-like and has only two degrees of freedom. It can undergo *flexion* (positive) and *extension* (negative), which brings the forearm closer to or further away from the upper arm, respectively, in the sagittal plane. The elbow is also capable of *pronation* (positive) and *supination* (negative), which is caused by rotation along the long axis of the forearm. Note that the palm of the hand faces down (pronation) or upward (supination) if the elbow is flexed so that the forearm and upper arm are perpendicular.

In order to determine these joint angles from given filtered VICON position data, fixed local coordinate systems must first be embedded in the trunk, the upper arm, and the forearm (Vaughan, Davis, and O'Connor 1992). The differences between the orientation of the proximal segment's coordinate system and that of the distal segment enable the calculation of these joint angles.

In general, the local z-axis is the longitudinal axis of the segment, the local x-axis of the segment is directed anteriorly, and the segment's local y-axis is directed laterally on the left side of the body (and medially on the right side of the body). Specifically, $\hat{i}_{seg}, \hat{j}_{seg}, \hat{k}_{seg}$, which define the local coordinate system for a given segment, are determined as indicated in Table 4.4.

Table 4.4 The determination of each segment's local coordinate system

Segment	Coordinate Axes	Direction
Trunk	$\hat{k}_{tr}$	from L5 to C7
	$\hat{j}_{tr}$	Perpendicular to the sagittal plane toward the left side of the body
	$\hat{i}_{tr}$	Perpendicular to $\hat{j}_{tr}$ and $\hat{k}_{tr}$ toward the front of the body
Upper Arm	$\hat{k}_{up}$	from the elbow joint center to the shoulder joint center
	$\hat{i}_{up}$	Perpendicular to the plane of the upper arm markers toward the front of the body
	$\hat{j}_{up}$	Perpendicular to $\hat{k}_{up}$ and $\hat{i}_{up}$ toward the left side of the body
Forearm	$\hat{k}_{fore}$	from the wrist joint center to the elbow joint center
	$\hat{i}_{fore}$	Perpendicular to the plane of the forearm markers toward the front of the body
	$\hat{j}_{fore}$	Perpendicular to $\hat{k}_{fore}$ and $\hat{i}_{fore}$ toward the left side of the body

The local coordinate systems for the trunk-upper arm-forearm linked system are shown in Figure 4.3.

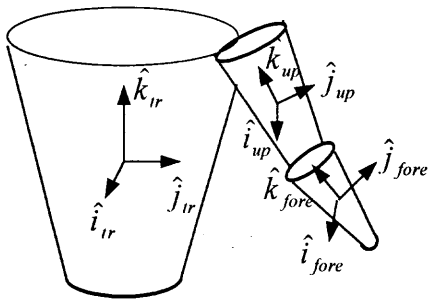

Figure 4.3 An illustration of the local coordinate systems

Next, each *joint*'s coordinate system is defined. One coordinate axis is the $\hat{j}_{prox}$ axis of the proximal segment. The second coordinate axis is the $\hat{k}_{dist}$ axis of the distal segment. The third coordinate axis, denoted $\hat{l}_{jt}$, is a floating axis perpendicular to the first two coordinate axes. That is, the shoulder joint's coordinate system consists of $\hat{j}_{tr}$, $\hat{k}_{up}$, and $\hat{l}_{sh}$, where $\hat{l}_{sh} = \hat{j}_{tr} \times \hat{k}_{up}$, and the elbow joint's coordinate system is made up of $\hat{j}_{up}$, $\hat{k}_{fore}$, and $\hat{l}_{eb}$, where $\hat{l}_{eb} = \hat{j}_{up} \times \hat{k}_{fore}$.

The relative orientation of two adjoining segments provides the anatomical joint angles. In accordance with the convention developed by Grood and Suntay (1983), the definitions below, which are illustrated by the accompanying figures, are employed in this analysis. Flexion, abduction, and internal rotation/pronation are denoted positive, while extension, adduction, and external rotation/supination are negative.

Note that in the given formulae for the calculation of these anatomical angles the arcsine function is used. This is because most of these joint angles are between $^{-}90^{o}$ and $^{+}90^{o}$ when measured from the vertical. One exception is elbow flexion/extension, which takes on values between 0^{o} (total flexion) and $^{-}180^{o}$ (full extension) from the vertical.

- Flexion^{+}/extension^{-} is defined as the angular displacement of the proximal segment when it is rotated about its $\hat{j}_{prox}$ axis while the distal segment remains stationary. The angle, α, is measured between $\hat{l}_{jt}$ and $\hat{i}_{prox}$.

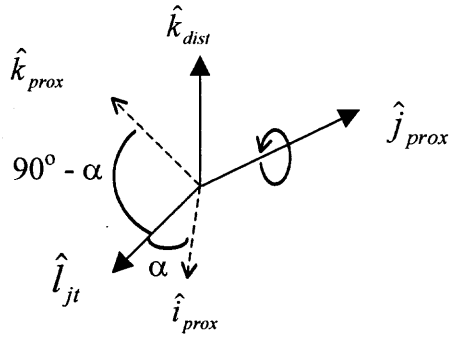

$$\sin\alpha = \cos\left(90^{o} - \alpha\right) = \hat{l}_{jt} \cdot \hat{k}_{prox} \Rightarrow \alpha = \sin^{-1}\left(\hat{l}_{jt} \cdot \hat{k}_{prox}\right)$$

(for shoulder flexion/extension)

or

$$\cos\alpha = \hat{l}_{jt} \cdot \hat{i}_{prox} \Rightarrow \alpha = \cos^{-1}\left(\hat{l}_{jt} \cdot \hat{k}_{prox}\right) - 180^{o} \text{ (for elbow extension)}$$

- Abduction^{+}/adduction^{-} is the angular rotation about the floating joint axis, $\hat{l}_{joint}$. The angle between $\hat{j}_{prox}$ and $\hat{k}_{dist}$ is actually $\beta + 90^{o}$.

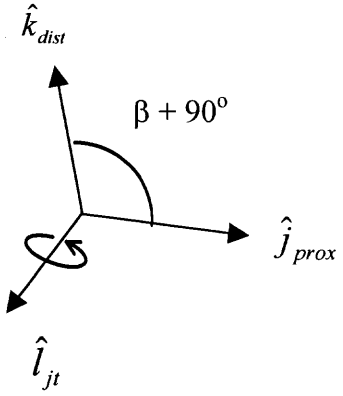

$$\sin(-\beta) = -\sin(\beta) = \cos(\beta + 90^{o}) = \hat{k}_{dist} \cdot \hat{j}_{prox} \Rightarrow \beta = -\sin^{-1}(\hat{k}_{dist} \cdot \hat{j}_{prox})$$

- Internal^{+}/external^{-} rotation is the angular displacement of the distal segment when it is rotated about its $\hat{k}_{dist}$ axis while the proximal segment remains stationary. The angle, γ, is measured between $\hat{l}_{jt}$ and $\hat{i}_{dist}$.

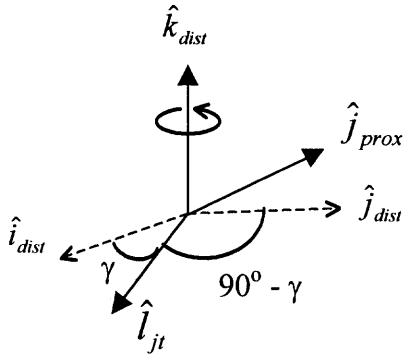

$$\sin\gamma = \cos(90^{o} - \gamma) = \hat{l}_{jt} \cdot \hat{j}_{dist} \Rightarrow \gamma = \sin^{-1}(\hat{l}_{jt} \cdot \hat{j}_{dist})$$

Thus, for a given configuration of body segments, the shoulder and elbow anatomical joint angles (flexion/extension, abduction/adduction, and internal rotation-pronation/external rotation-supination) are determinable. Clearly, these angles will vary with time. Moreover, the flexion/extension angles should be similar to the joint angles obtained when the position data is projected into the sagittal plane (see Section 5.2).

Graphs of the shoulder and elbow angles of Piston Cycle 1 are shown in Figure 4.4 on the next page. Recall that a cycle lasts from wheel contact to wheel contact.

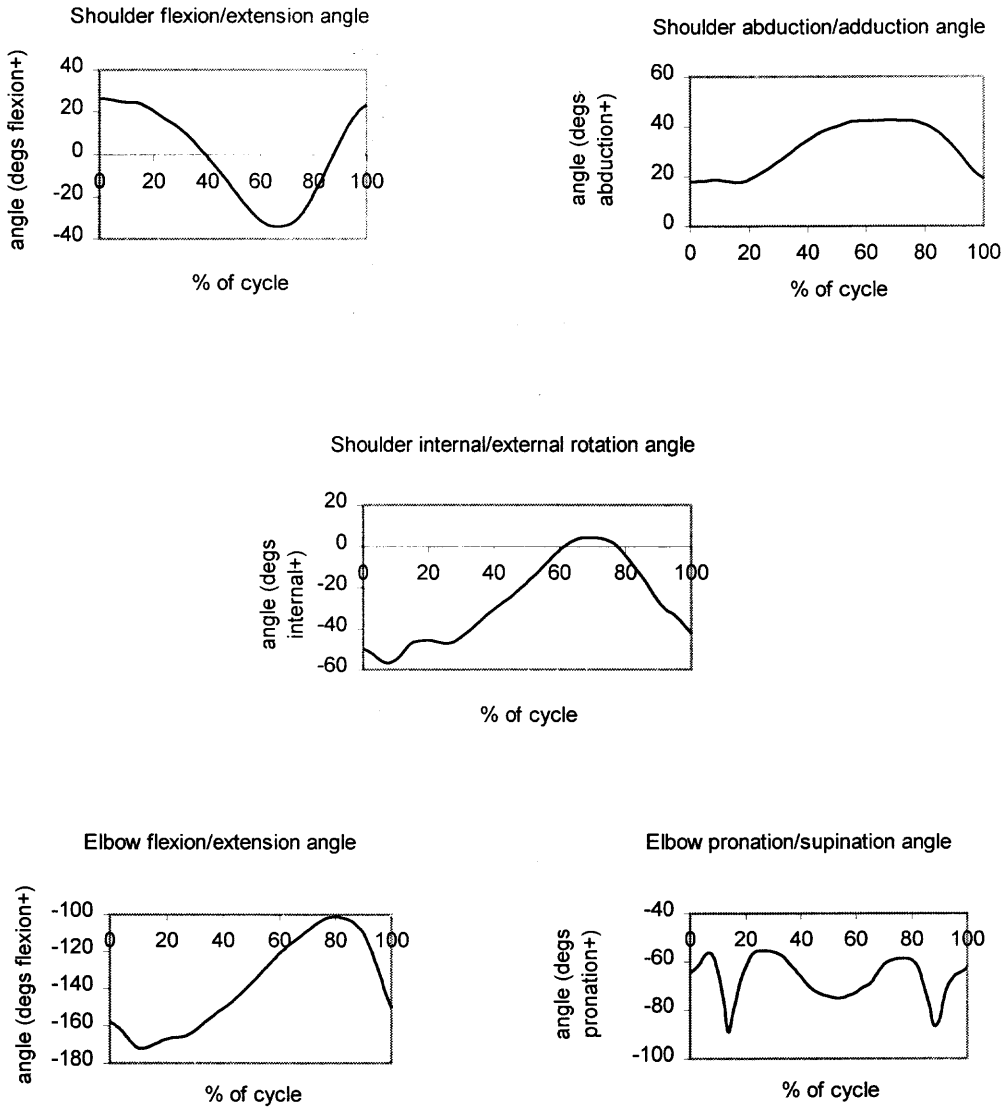

Figure 4.4 The dynamic angles of the shoulder and elbow during Piston Cycle 1

From Figure 4.4 above, it is interesting to note the joint motion throughout the stroke cycle. At push, the shoulder is maximally flexed, minimally abducted, and almost maximally externally rotated, whereas the elbow is nearly fully extended and minimally supinated. Shortly after push, the upstroke part of the cycle begins. Upstroke continues

until the arm segments move toward their maximal height at about 65 – 70 % of the cycle. During upstroke, the following joint motion occurs:

- The shoulder continues to extend, abduct, and internally rotate (causing the upper arm to upward in the sagittal plane, away from the trunk in the frontal plane, and rotate inward toward the trunk).
- The elbow becomes less extended (causing the sagittal-plane angle between the forearm and the upper arm to decrease) and is used right after push to flick the wrist producing a burst of supination.

Once the arm segments reach maximum height, the downstroke part of the cycle commences. Downstroke lasts until the pushrim is contacted. During downstroke, the following joint motion occurs:

- The shoulder flexes, adducts, and externally rotates (causing the upper arm to move downward in the sagittal plane, closer to the trunk in the frontal plane, and rotate outward away from the trunk).
- The elbow extends (causing the sagittal-plane angle between the forearm and the upper arm to increase) and flicks the wrist again, producing a burst of supination.

Also of interest is the relatively small shoulder abduction/adduction range of motion throughout the cycle. This is consistent with a piston-style wheelchair racing

stroke. It will be important to compare the experimental sagittal-plane joint motion behaviors with that indicated by model output.

4.3.2 Pushrim Contact Angle

At the onset of the push phase of the stroke, the athlete and the racing wheelchair contact each other when the racer hits the pushrim of the wheel. This racer/chair contact continues throughout the duration of push. If the wheel is considered as a segment, it clearly cannot internally or externally rotate nor can it abduct or adduct at any time in the cycle, since it is secured on its axle in a fixed manner which does not allow movement in these directions. However, the wheel can *flex* or *extend* (produced by rotating about the hub axle) relative to the athlete's forearm segment during push. That is, there is a dynamic angle between the forearm segment and the line segment connecting the wheel hub to the point of contact on the pushrim throughout push. Since this angle is analogous to flexion/extension, it is called α_{wh}. Figure 4.5 illustrates the pushrim contact angle.

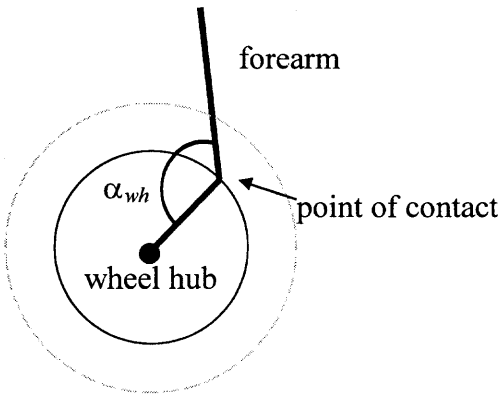

Figure 4.5 The pushrim contact angle, α_{wh}

To calculate the pushrim contact angle at an instant in the push phase of the racing stroke, the point of contact is first approximated by the location of the wrist joint center relative to the global axes. Since the coordinates of the wheel hub are also known, the vector from the point of contact to the hub, $\vec{a}_{wh}$, is determinable. The vector from the point of contact to the elbow joint center, $\vec{a}_{fore}$, is also calculable. The pushrim contact angle is then found using Equation 4.1.

$$\alpha_{wh} = \cos^{-1}\left(\frac{\vec{a}_{wh} \cdot \vec{a}_{fore}}{|\vec{a}_{wh}||\vec{a}_{fore}|}\right) \tag{4.1}$$

In the case of Piston Cycle 1, the three-dimensional wheel contact angle was determined to be approximately 80.2 degrees. The configuration of push in this trial, as determined from filtered VICON data, is illustrated in Figure 4.6.

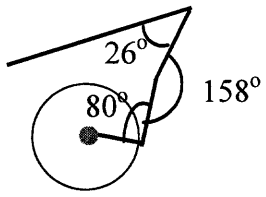

Figure 4.6 Push configuration of Piston Cycle 1

4.4 Joint Reaction Forces and Moments

When the body segments must remain in contact with the pushrim of the wheel during the push phase, forces of constraint (pushrim contact forces) are present, as are moments. These forces, in turn, cause reaction forces and moments at each of the body joints. Inverse modeling allows for the computation of joint reaction forces and moments by using the linear and angular forms of Newton's Second Laws if it is possible to clinically measure these forces/moments of constraint. Many labs are equipped with ground reaction force plates, which will record such data when a subject walks over them, performs a squat while standing on them, etc. However, similar instrumentation, which would record forces and moments applied to a wheelchair pushrim, has only recently been developed and is still being improved (Asato *et al.* 1993).

In several studies (Boninger *et al.* 1997, Robertson *et al.* 1996, and Shimada *et al.* 1998), the SMART Wheel (developed by Cooper's group) or a similar device, which has strain gauges attached to a wheel's pushrim, was used to determine these constraint forces/moments during standard (non-racing) wheelchair propulsion. Subjects had to propel a lab chair outfitted with the SMART Wheel and not their own chair in these investigations. Wheelchair racing athletes, like most athletes, are quite particular about their chairs and wheels, which are custom-made to suit the individual in most cases. Therefore, a portable device, as opposed to an instrumented SMART Racing Wheel, would be necessary for racing studies to allow the athlete to use his or her own chair and wheels. Such a device is not yet available. Perhaps this is because during wheelchair racing at moderate to fast speeds, the percentage of time spent in the push phase is relatively small, often only about five percent. Thus, even if a portable device were designed to measure

pushrim impact forces and moments, it would only provide information during a small amount of the stroke cycle.

Because such portable instrumentation was not available in this experiment, required input for inverse modeling of experimental data could not be furnished. Therefore, this dissertation does not include the determination of joint reaction forces and moments during push. However, the procedure for calculating these kinetic data via inverse modeling is outlined here for completeness of discussion (Vaughan, Davis, and O'Connor 1992). To begin the determination of the reaction forces and moments existing at the wrist, elbow, and shoulder, it is necessary to create free-body diagrams for the whole system showing all forces/moments acting on the necessary segments. Such a free-body diagram of the forces acting on the system is shown in Figure 4.7 below.

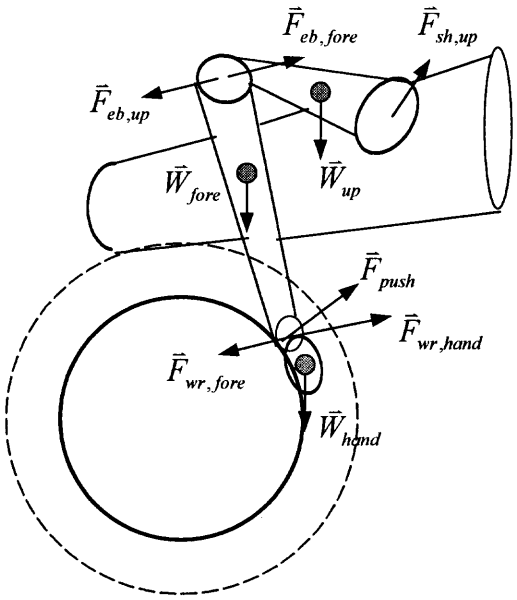

Figure 4.7 A free-body diagram of the forces present in the system during push

Note from the free-body diagram, $\vec{F}_{wr,fore} = -\vec{F}_{wr,hand}$ and $\vec{F}_{eb,up} = -\vec{F}_{eb,fore}$. Applying the linear form of Newton's Second Law to the free-body force diagram gives the vector equations below.

$$\text{hand}: \quad \vec{F}_{wr,hand} = m_{hand}\vec{a}_{handCG} - m_{hand}\vec{g} - \vec{F}_{push}$$

$$\text{forearm}: \quad \vec{F}_{eb,fore} = m_{fore}\vec{a}_{foreCG} - m_{fore}\vec{g} - \vec{F}_{wr,fore}$$

$$\text{upper arm}: \quad \vec{F}_{sh,up} = m_{up}\vec{a}_{upCG} - m_{up}\vec{g} - \vec{F}_{eb,up}$$

The following symbols are used above: $\vec{F}_{push}$ is the measured pushrim contact force, $\vec{g}$ is the gravitational vector, m_{seg} is the mass of the segment, and $\vec{a}_{segCG}$ is the acceleration of each segment's center of gravity, which can be found by using a finite difference scheme on center-of-gravity position data. In this way, the joint reaction forces at the wrist, elbow, and shoulder are found consecutively.

An analogous technique is used to determine the joint reaction moments. The wrist reaction moment equals the calculable change of angular momentum of the hand[1] minus the sum of measured moments and those produced by the pushrim contact forces and the wrist joint reaction force on the hand. Once the moment at the wrist is found, it is possible to calculate those at the elbow and shoulder in similar fashion.

[1] expressible in terms of the moments of inertia, angular velocities, and angular accelerations, all of which are known or determinable quantities

4.5 Energy Calculations on Experimental Data

Analysis of experimental data also includes calculating mechanical energies of the body segments and of the racing chair during a given motion. In the following sections, details are given for determining the total mechanical energies of both the wheelchair and the body segments under *experimental* racing conditions (and not actual road-racing conditions). For a given segment, total mechanical energy includes the sum of its potential and kinetic energies. Details are provided on calculating the energies of a disk wheel, a point-mass body segment, and a distributed-mass body segment.

4.5.1 Wheelchair Energy Calculations

The energies of the wheelchair will be examined first. Again, only one side is considered, as symmetry is assumed to exist. The wheel is a solid disk of given radius, constant density, and mass, which locates the center of mass at the hub. The racing wheelchair is a combination of wheels and rigid bodies maintained at fixed orientations to each other. As noted above, experimental wheelchair racing conditions – and not actual road-racing circumstances – are examined here. Therefore, the only dynamic part of the racing chair in the experimental setup case is the wheels.

Because the athlete is seated in the wheelchair, wheel motion is affected by the mass of the entire athlete/chair system. This mass, m_{rest}, consisting of the body mass and chair mass not accounted for by specific segments included in the model, is idealized to be equally-distributed at the wheels' hubs as a point mass on each side. That is, half m_{rest} (total body mass plus chair mass minus the masses of the segments already included in the model) is located at each hub. Therefore, the masses involved in computing the

mechanical energy of one side of the racing wheelchair are actually the mass of one wheel and half m_{rest}.

To compute the potential energy, half m_{rest} plus the mass of one wheel and the wheel hub's height from the floor, which is recorded during the VICON trial, will be used. Moreover, since the chair is fixed in the CompuTrainer device for experimental data collection, the hub height will remain relatively constant throughout the cycle. Potential energy equals the product of the sum of half m_{rest} and the mass of one wheel, the gravitational constant (9.81 m/s^2), and the hub height.

As for the wheel's translational kinetic energy, its component is zero in experimental racing conditions because the chair is held fixed in place, and therefore, the hub remains stationary. The wheel can move in only one direction, namely it rotates about the wheel axle. Computation of the wheel's rotational kinetic energy requires the moment of inertia and the angular velocity of the wheel about its axle.

To determine this angular velocity, the velocity of the marker on the wheel is first found. For empirical data, this velocity is determined by applying a finite difference scheme to the wheel marker's position data to obtain the *x*-, *y*-, and *z*-components of the marker's velocity. The finite difference method used to obtain these velocity components is given by Equation 4.2 where $x_1(j)$, $x_2(j)$, and $x_3(j)$ are used to denote the *x*-, *y*-, and *z*-position of the wheel marker, respectively, at time *j*.

$$v_{x_i}(t) = \frac{dx_i(t)}{dt} = \frac{x_i(t+\Delta t) - x_i(t-\Delta t)}{2(\Delta t)} \quad \text{for } i = 1, 2, 3 \qquad (4.2)$$

The linear velocity of the marker on the wheel is then given by Equation 4.3.

$$v_{mrkr}(t) = \sqrt{\sum_{i=1}^{3} v_{x_i}{}^2(t)} \tag{4.3}$$

The angular velocity of the wheel, ω_{wh}, is determined by calculating the quotient of the marker's velocity and the distance from the hub to the marker, as indicated in Equation 4.4.

$$\omega_{wh}(t) = \frac{v_{mrkr}(t)}{r_{mrkr}} \tag{4.4}$$

This angular velocity, ω_{wh}, is used to determine the rotational component of kinetic energy provided by the motion of each wheel. A solid, uniform disk has moment of inertia (about an axis through its center and perpendicular to the disk) equal to half the product of the radius squared and the mass. Rotational kinetic energy is calculated as one-half the moment of inertia times the angular velocity squared.

Therefore, the chair's rotational kinetic energy at time t is determined by Equation 4.5, where m_{wh} is the mass of one wheel and v_{wh} is the wheel's velocity. Recall that $v = r\omega$. Also, no-slip conditions have been assumed.

$$T_{wh}(t) = \frac{1}{2} I_{wh} \omega_{wh}{}^2(t) = \frac{1}{2}\left(\frac{m_{wh} r_{wh}{}^2}{2}\right)\omega_{wh}{}^2(t) = \frac{1}{4} m_{wh} v_{wh}{}^2(t) \tag{4.5}$$

Figures 4.8 and 4.9 indicate the results of an analysis of Piston Cycle 1 data. Fixing the racing chair on the CompuTrainer results in the hub being almost stationary, which in turn causes the wheelchair potential energy to be almost constant as seen in Figure 4.8. If the athlete contacts the pushrim and his hands are moving slower than the wheel, the wheel will lose speed. This explains the initial lower kinetic energy of the wheel evident in Figure 4.9. This effect was also described by Sanderson and Sommer (1985).

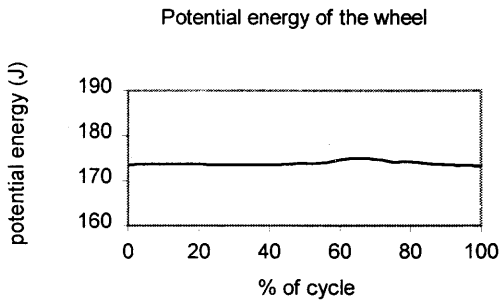

Figure 4.8 The wheel's potential energy in Piston Cycle 1

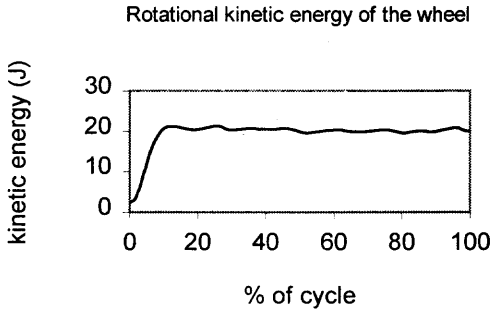

Figure 4.9 The wheel's rotational kinetic energy in Piston Cycle 1

4.5.2 Body Segment Energy Calculations

The energies of the body segments will now be examined. Again, only one side of the body will be considered. Each segment's mass and center of mass's height from the floor will be used to compute its potential energy. When the segment is represented as a point-mass, its mass, the location of its center of mass, and its velocity are needed to determine its kinetic energy. On the other hand, when the segment is idealized as a distributed-mass, the moments of inertia about its three segment (*local*) coordinate axes through its center of mass and the angular velocities about its segment axes are also required to find its kinetic energy due to rotation. Since the athlete/chair is not translating under experimental conditions, the segments' translational kinetic energies are zero.

The masses of each segment are found, as explained in Section 4.2, by using information from anthropometric tables (Dempster 1955), once the total body mass is determined by weighing the individual. Each segment's center of mass's height from the floor is resolved from marker position data and either table information (point-mass case) or a mathematical formula, which is dependent on segment structural data (distributed-mass case). Potential energy, mass times gravitational constant (9.81 m/s^2) times height of the center of mass, is then found.

If the body segments are assumed to be point masses, then a segment's kinetic energy is calculated as half its mass times the square of the velocity of its center of mass. This velocity is obtained by applying a finite difference scheme to center of mass position data, which can be calculated from recorded marker kinematic data. The finite difference method used in this research is supplied below by Equation 4.6 where $x_1(j)$, $x_2(j)$, and

$x_3(j)$ are used to denote the x-, y-, and z-position, respectively, of the segment's center of mass at time j.

$$v_{x_i}(t) = \frac{dx_i(t)}{dt} = \frac{x_i(t+\Delta t) - x_i(t-\Delta t)}{2(\Delta t)} \quad \text{for } i = 1, 2, 3 \tag{4.6}$$

The velocity of the center of mass of the segment is then given by Equation 4.7.

$$v_{seg,\,cm}(t) = \sqrt{\sum_{i=1}^{3} {v_{x_i}}^2(t)} \tag{4.7}$$

The point-mass segment's kinetic energy is now calculated via Equation 4.8, where m_{seg} is the mass of the segment.

$$T_{pt\ mass\ seg}(t) = \frac{1}{2} m_{seg} {v_{seg,cm}}^2(t) \tag{4.8}$$

The kinetic energy of a distributed mass is found by adding the kinetic energy of its center of mass and the rotational kinetic energy of the distributed mass about its center of mass (Mansour *et al.* 1982). In order to find this supplementary rotational kinetic energy, its moments of inertia about its three axes will be needed. An assumption necessary to make at this point is that all segments can be thought of as *rigid bodies*. A rigid body, as defined by Goldstein (1980), is "a system of particles in which the distances (between every two particles) are fixed and cannot vary with time."

It is assumed that the distributed-mass body segments are shaped like frustrums. Below are the formulae used to calculate the moments of inertia about the segment local axes through the center of mass, as well as the locations of the centers of mass, which are notably comparable to those supplied by anthropometric table data (Dempster 1955). These formulae are derived in Appendix A.

Moments of Inertia:

$$I_{x,cm} = I_{y,cm} = \frac{3m_{seg}}{80\sigma^2}\left[4\sigma\left(R_S{}^2\sigma + R_S R_B + R_B{}^2\right) + L^2\left(\mu^4 + 4\mu^3 + 10\mu^2 + 4\mu + 1\right)\right]$$

and

$$I_{z,cm} = \frac{3m_{seg}}{10\sigma}\left(R_S{}^2\sigma + R_S R_B + R_B{}^2\right)$$

Location of Center of Mass (from the proximal end):

$$z_{cm} = L - \frac{L}{4\sigma}\left(\mu^2 + 2\mu + 3\right)$$

The variables used in the above formulae are as follows:

m_{seg} = segment mass (kg)

L = segment length (m)

R_S = small radius of segment (m)

R_B = big radius of segment (m)

$\mu = \frac{R_S}{R_B}$

$\sigma = 1 + \mu + \mu^2$

Table 4.5 lists the moments of inertia and the locations of the center of mass pertaining to the individual modeled in this thesis. As can be seen, the calculated values are in reasonable agreement with table data.

Table 4.5 Moments of inertia about the segment axes through the centers of mass and locations of the centers of mass from anthropometric tables (Dempster 1955) and as calculated for frustrums

Segment	I_x (kg m^2)	I_y (kg m^2)	I_z (kg m^2)	Location of Center of Mass (% from proximal end) (table data in parentheses)
Upper Arm	0.0139	0.0139	0.00247	45.9 (43.6)
Forearm	0.00931	0.00931	0.000994	45.7 (43.0)

Now that the moments of inertia about the segment axes are known, the angular velocities of the segments about these axes are needed in order to calculate the additional rotational kinetic energies. When considering three dimensions (which is the case of empirical data), the concept of *rigid body rotation* must be examined in detail (Goldstein 1980). There are six degrees of freedom available to locate a rigid body in three-dimensional space: a point (x,y,z) that locates the body's center of mass and three angles that orient it relative to some fixed global coordinate axes xyz (an inertial frame of reference). Embedding a fixed local coordinate system $x'y'z'$ in each segment so that the origin coincides with the segment's center of mass, provides an important non-inertial

frame of reference. In fact, the rotations that are needed to determine the rotational energies of each segment are those about the three *local* coordinate axes, which mandates the determination of transformation equations relating the inertial (global *xyz*) and non-inertial (local *x'y'z'*) coordinates.

There are many different sequences of rotations, which can relate the global and local set of axes. These are called *Euler schemes*. The following explanation considers the *Euler xyz scheme,* which is illustrated below. All rotations are assumed positive if they occur in a counterclockwise direction. Both sets of axes begin coincident with one another. The local axes are then rotated an angle θ_1 about the global *x*-axis. This produces intermediate axes ξ, η, and ζ. The next rotation of an angle θ_2 about the intermediate η-axis creates the *line of nodes* (the intersection of the *yz*-plane and the $\eta\zeta$-plane). Once again, transitional axes, ξ', η', and ζ', are formed. The last rotation through an angle θ_3 about the ζ'-axis completes the orientation of the local axes denoted *x'y'z'*, and hence, completes the orientation of the body segment. The scheme is denoted *xyz* because of the order of the three rotations.[1] Anatomically, this scheme can be thought of as "tilt, somersault, twist." It is illustrated in Figure 4.10 on the next page.

[1] Twelve Euler schemes exist: *xyz*, *xyx*, *xzy*, *xzx*, *yxz*, *yxy*, *yzx*, *yzy*, *zxy*, *zxz*, *zyx*, and *zyz*. (Note that no two consecutive rotations are permitted about the same axis.)

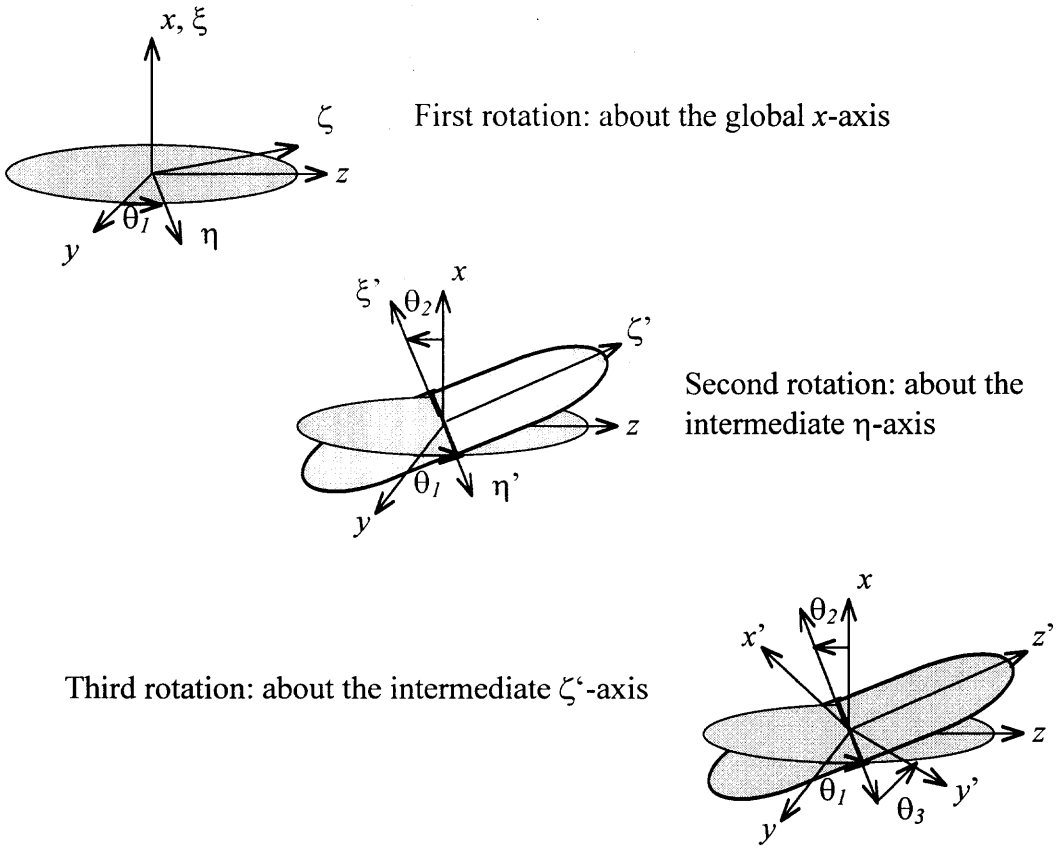

Figure 4.10 The *xyz* Euler scheme ("tilt, somersault, twist")

Thus, to relate global *xyz*-coordinates to local *x'y'z'*-coordinates, the complete transformation equations are obtained by multiplying the three individual rotations together in the appropriate order. This rotation is given by Equation 4.9 below where *cj* and *sj* are abbreviations for $\cos\theta_j$ and $\sin\theta_j$, respectively, and *E* denotes the rotation matrix for the Euler angles.

$$\begin{pmatrix} x' \\ y' \\ z' \end{pmatrix} = \begin{pmatrix} \cos\theta_3 & \sin\theta_3 & 0 \\ -\sin\theta_3 & \cos\theta_3 & 0 \\ 0 & 0 & 1 \end{pmatrix} \begin{pmatrix} \cos\theta_2 & 0 & \sin\theta_2 \\ 0 & 1 & 0 \\ -\sin\theta_2 & 0 & \cos\theta_2 \end{pmatrix} \begin{pmatrix} 1 & 0 & 0 \\ 0 & \cos\theta_1 & \sin\theta_1 \\ 0 & -\sin\theta_1 & \cos\theta_1 \end{pmatrix} \begin{pmatrix} x \\ y \\ z \end{pmatrix} \tag{4.9}$$

$$= \begin{pmatrix} c2c3 & c1s3 - s1s2c3 & s1s3 + c1s2c3 \\ -c2s3 & c1c3 + s1s2s3 & s1c3 - c1s2s3 \\ -s2 & -s1c2 & c1c2 \end{pmatrix} \begin{pmatrix} x \\ y \\ z \end{pmatrix} = E \begin{pmatrix} x \\ y \\ z \end{pmatrix}$$

To extract the Euler angles from experimentally-collected position data, the idealization of each body segment as a rigid body must first be carefully considered. First, define a segment's *local data* as its filtered VICON position minus the location of its center of mass. Examining local data reduces the rigid body motion to pure rotation, as the linear displacement of its center of mass is already removed. If the segment was a true rigid body and its marker positions were measured exactly, then the rotation matrix required to match the marker position data from time t to time t+1 could be found by solving the linear system $R(t)\vec{x}_t = \vec{x}_{t+1}$, where $x_j(t)$, an element of vector $\vec{x}_t$, represents the j^{th}-marker's local position at time t.

However, this straightforward approach cannot be immediately undertaken in the case of empirical data. VICON data, even after filtering, has some measurement error and each segment's markers, which are attached to the skin, tend to not remain at constant fixed distances from one another, so that the segment position data recorded experimentally does not *exactly* represent a rigid body. That is, there is no exact rotation solution, $R(t)$, to the matrix equation $R(t)\vec{x}_t = \vec{x}_{t+1}$. Therefore, the *closest* rotation matrix, $R(t)$, that can be found which fits local marker data at time t to local data at time t+1 needs to be determined.

This problem of finding a rotation matrix at time t that will best solve $R(t)\vec{x}_t = \vec{x}_{t+1}$ involves minimizing the error between the local data at time t+1 and the rotated time-t data, which is given by $R(t)\vec{x}_t$ (Arun, Huang, and Blostein 1987). The details of the solution to this problem are given in Appendix B. At each time step, the closest rotation matrix, R, is given by Equation 4.10 below. In Equation 4.10, P and Q are components of the singular value decomposition, $P\Gamma Q^T$, of the matrix BA^T, where the j^{th} columns of A and B contain the local j^{th}-marker data at time t and at time t+1, respectively.

$$R = P\begin{bmatrix} 1 & 0 & \cdots & 0 \\ 0 & 1 & \cdots & 0 \\ \vdots & \vdots & \ddots & \vdots \\ 0 & 0 & \cdots & \det(PQ^T) \end{bmatrix} Q^T \qquad (4.10)$$

Once the closest rotation matrix at each time step, $R(t)$, has been found, the time-t Euler angles are obtained by equating $R(t)$ with E, the rotation matrix for the Euler angles given above in Equation 4.9. A direct comparison of the elements of these matrices gives the following formulae for the determination of the Euler angles, $\theta_1(t)$, $\theta_2(t)$, and $\theta_3(t)$, where r_{ij} denotes the ij^{th} element of $R(t)$:

$$\theta_1(t) = \arctan\left(\frac{-r_{32}}{r_{33}}\right)$$

$$\theta_2(t) = \arcsin(-r_{31})$$

$$\theta_3(t) = \arctan\left(\frac{-r_{21}}{r_{11}}\right)$$

Having a relationship, *E*, between coordinates in the inertial reference system (global) and coordinates in the non-inertial frame (local) enables the calculation of the required angular velocities of a given segment about its local axes through its center of mass (Goldstein 1980). These velocities are expressible in terms of the segment's Euler angles and their time-derivatives. Each angle is first examined separately.

Since ω_{θ_1} is parallel to the global x-axis, the complete rotation transformation must be applied to obtain local coordinates and the component in the *x*-direction is selected to get the following:

$$\left(\omega_{\theta_1}\right)_{x'} = \dot{\theta}_1 c2c3 \qquad \left(\omega_{\theta_1}\right)_{y'} = -\dot{\theta}_1 c2s3 \qquad \left(\omega_{\theta_1}\right)_{z'} = -\dot{\theta}_1 s2$$

To find ω_{θ_2} only the final rotation needs to be used to obtain local coordinates since its direction is the same as the η' axis. This gives the following η'-direction components for ω_{θ_2}:

$$\left(\omega_{\theta_2}\right)_{x'} = \dot{\theta}_2 s3 \qquad \left(\omega_{\theta_2}\right)_{y'} = \dot{\theta}_2 c3 \qquad \left(\omega_{\theta_2}\right)_{z'} = 0$$

Finally, since ω_{θ_2} lies along the local z'-axis, it only has one non-zero component which is in the z'-direction:

$$\left(\omega_{\theta_3}\right)_{x'} = 0 \qquad \left(\omega_{\theta_3}\right)_{y'} = 0 \qquad \left(\omega_{\theta_3}\right)_{z'} = \dot{\theta}_3$$

These separate contributions to the *local* angular velocities are combined to give the components of ω with respect to the body axes written below in Equation 4.11.

$$\omega_{x'} = \dot{\theta}_1 \cos\theta_2 \cos\theta_3 + \dot{\theta}_2 \sin\theta_3$$

$$\omega_{y'} = -\dot{\theta}_1 \cos\theta_2 \sin\theta_3 + \dot{\theta}_2 \cos\theta_3 \qquad (4.11)$$

$$\omega_{z'} = -\dot{\theta}_1 \sin\theta_2 + \dot{\theta}_3$$

To calculate the needed velocities of the Euler angles, a finite difference scheme is used. This scheme is given by Equation 4.12 below, where $\theta_1(j)$, $\theta_2(j)$, and $\theta_3(j)$ are used to denote the three Euler angles at time j.

$$\dot{\theta}_i(t) = \frac{\theta_i(t+\Delta t) - \theta_i(t-\Delta t)}{2(\Delta t)} \quad \text{for } i = 1, 2, 3 \qquad (4.12)$$

Therefore, the components of a rigid body's additional distributed-mass rotational kinetic energy are given by Equations 4.13 – 4.15 below where *cj* and *sj* are abbreviations for cosine and sine of θj, respectively. To obtain the total kinetic energy of a rigid body, these quantities are added to the segment's center of mass kinetic energy (as calculated in the point-mass case via Equation 4.8).

$$T_{x,\,seg} = \frac{1}{2} I_{x,\,cm} \omega^{2}_{x,\,seg} = \frac{3m_{seg}\left(\dot{\theta}_1 c2c3 + \dot{\theta}_2 s3\right)^2}{160\sigma^2}\left[4\sigma\left(R_S{}^2\sigma + R_S R_B + R_B{}^2\right) + L^2\left(\mu^4 + 4\mu^3 + 10\mu^2 + 4\mu + 1\right)\right] \tag{4.13}$$

$$T_{y,\,seg} = \frac{1}{2} I_{y,\,cm} \omega^{2}_{y,\,seg} = \frac{3m_{seg}\left(-\dot{\theta}_1 c2s3 + \dot{\theta}_2 c3\right)^2}{160\sigma^2}\left[4\sigma\left(R_S{}^2\sigma + R_S R_B + R_B{}^2\right) + L^2\left(\mu^4 + 4\mu^3 + 10\mu^2 + 4\mu + 1\right)\right] \tag{4.14}$$

$$T_{z,\,seg} = \frac{1}{2} I_{z,\,cm} \omega^{2}_{z,\,seg} = \frac{3m_{seg}\left(-\dot{\theta}_1 s2 + \dot{\theta}_3\right)^2}{20\sigma}\left(R_S{}^2\sigma + R_S R_B + R_B{}^2\right) \tag{4.15}$$

In summary, to obtain the total energy present in a given segment at time *t*, its potential energy and its rotational kinetic energy must be calculated. The potential energy is calculated from recorded position data and the kinetic energy is found by using velocities from position data (point mass), as well as Euler angles and their derivatives (distributed mass).

Figures 4.11 through 4.14 present Piston Cycle 1 body segment and total system (athlete/chair) energies. In all cases, results from both the point-mass body segment / disk wheel system and the distributed-mass body segment / disk wheel system are included.

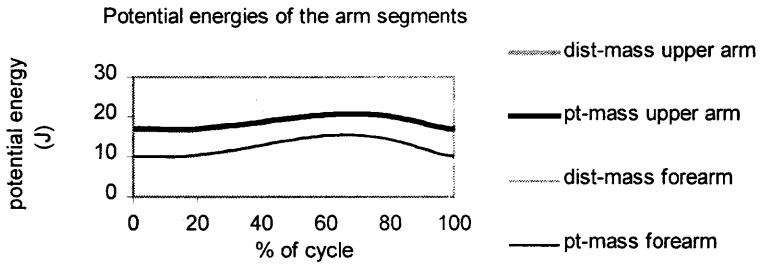

Figure 4.11 Potential energies of the arm segments in Piston Cycle 1

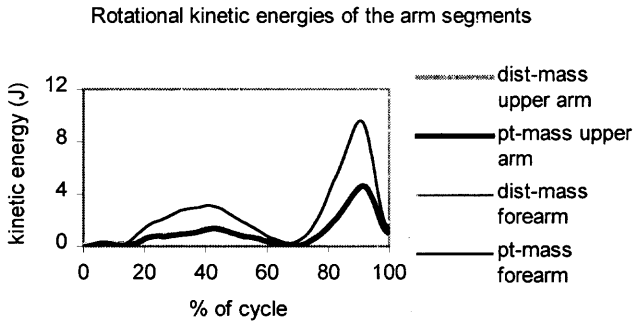

Figure 4.12 Rotational kinetic energies of the arm segments in Piston Cycle 1

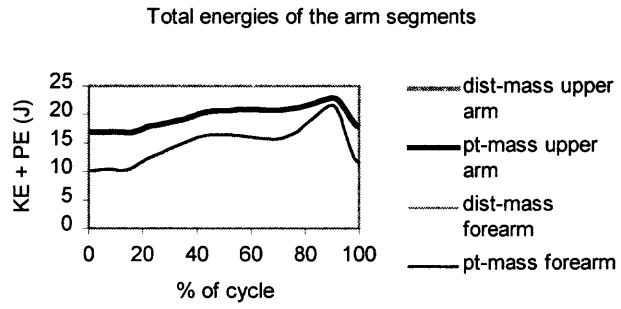

Figure 4.13 Total energies of the arm segments in Piston Cycle 1

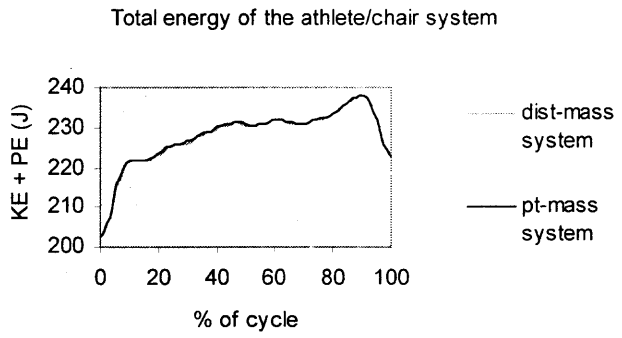

Figure 4.14 Total energy of the athlete/chair system in Piston Cycle 1

Although the point-mass and distributed-mass energies seem to be nearly identical, as evidenced by the graphs above, it is important to note that there are meaningful differences. Close examination of the arm segments' kinetic energies in the distributed-mass case reveals that the additional component of rotational kinetic energy about the segment's center of mass is quite significant during specific moments of the racing stroke cycle. These additional kinetic energy amounts are graphed in Figure 4.15 and their percentages of the overall rotational kinetic energies in the arm segments are shown in Figure 4.16.

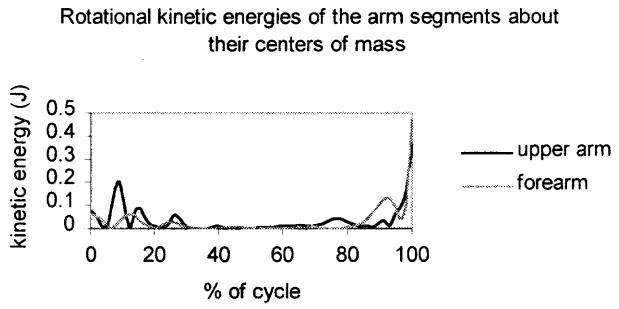

Figure 4.15 The rotational kinetic energy of the arm segments about their centers of mass

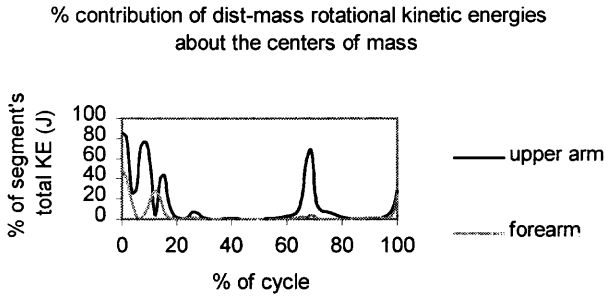

Figure 4.16 The percent of arm segments' total kinetic energies provided by rotation about the segments' centers of mass

It is apparent from the figures that both arm segments' kinetic energies are greatly affected by rotation about their centers of mass immediately preceding, during, and instantly following the push period. Furthermore, upper arm rotation, and to a lesser extent forearm rotation, is again significant at about 70 % of the stroke cycle, which is when maximum height is reached and downstroke is initiated. Therefore, segment rotation is significant near the push period and at maximum height, but is insignificant elsewhere in the cycle. That is, if a point-mass model is used, it will capture the behavior of the wheelchair racing motion most effectively during the upstroke and downstroke

periods of the recovery phase. Since the mathematical model presented in this thesis includes point-mass segments, this model will best simulate recovery upstroke and downstroke.

CHAPTER 5

OUTLINE OF TWO-DIMENSIONAL DATA ANALYSIS

5.1 Two-dimensional Data

There are two specific instances in this research when data is two-dimensional, namely the case of the model and when VICON data is projected into the sagittal plane of the athlete being modeled. Projecting VICON data into the sagittal plane causes the unconstrained, three-dimensional racing motion to now possess only the two degrees of freedom afforded by the plane. Some of this two-dimensional projected data is used as input to the model so that experimentally accomplished racing strokes can be simulated in this research.

The details of segment angle calculations and an outline of mechanical energy analysis for two-dimensional data are provided in this chapter. Once this analysis is complete, projected empirical racing strokes can be compared with those produced by the model.

5.2 Projection of VICON Data into the Sagittal Plane

In order to project filtered VICON data into the sagittal plane, two main steps must be completed. First, the sagittal plane must be defined and second, the three-dimensional marker position data must be projected into it. Specifically, this algorithm is as follows:

1) The left and right tubercle markers' VICON locations are averaged to give *TubMid*, the midpoint of the tubercles, which is assumed to lie in the sagittal plane. The sagittal plane goes through *TubMid*, C7, and L5. The vector from*TubMid* to C7 is crossed with the vector from *TubMid* to L5 to produce $\vec{n}$, a vector normal to the sagittal plane.

2) Any global-coordinate point, $\vec{x}$, is projected into the sagittal plane by completing the following three steps:

   a) Determine $\vec{v}$, the vector from *TubMid* (which is in the sagittal plane) to the specified point, $\vec{x}$.

   b) Project $\vec{v}$ onto $\vec{n}$ by using the standard projection equation,

   $$\vec{v}_n = \frac{\vec{n} \cdot \vec{v}}{|\vec{n}|^2} \vec{n}.$$

   c) Find the global coordinates of the point in the sagittal plane by Equation 5.1.

   $$\vec{x}_{sag} = TubMid + \vec{v} - \vec{v}_n \qquad (5.1)$$

Figure 5.1 illustrates the algorithm outlined above.

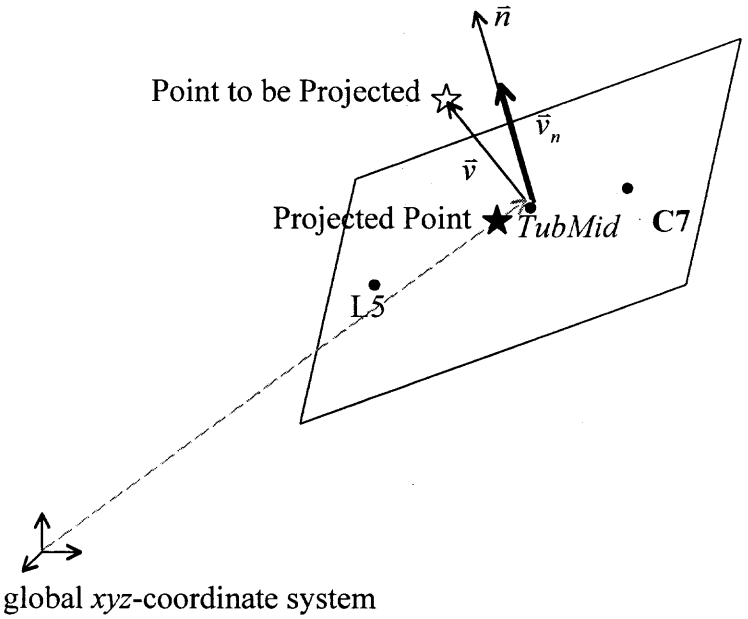

Note: All point locations are given in global coordinates.

Figure 5.1 Projecting a known point into the sagittal plane

5.3 Structural Parameters

Each segment's mass, center of mass location, and length are needed to complete an analysis of the two-dimensional data in the point-mass / disk wheel model. These parameters are all input of the mathematical model. Once again, the segment's length is measurable and its mass and the location of its center of mass are determinable by anthropometric tables (Dempster 1955). In addition, each wheel's mass, full radius, and pushrim radius, as well as the total chair mass, which can all be measured, must be known.

5.4 Angles

There are three different types of angles, which are used to describe two-dimensional movement. They are the segment horizon angle θ, the joint anatomical angle α_{jt}, and the pushrim contact angle α_{wh}. The determination of these angles is described in this section. The model output consists of θ's so that extracting horizon angles from projected, filtered VICON data will allow for the comparison of model predictions and empirical movement. Also, model horizon angles (θ's) should be manipulated to provide two-dimensional anatomical joint angles (α_{jt}'s), which are meaningful to the clinician.

5.4.1 Segment Horizon Angles

One important angle used to compare empirical data projected into the sagittal plane with model output is the angle a segment forms with the horizontal, the *horizon angle*. Horizon angles are denoted by θ's. Horizon angles are model output. To determine the horizon angle for a given segment from projected data, Equation 5.2 is employed. The sign function included in this formula causes the segment horizon angle to be designated positive if it measured counterclockwise from the horizontal or else negative. Also, the arctan2 function is used (as opposed to just arctan) because it has a full range from zero to 2π. Figure 5.2 illustrates this calculation with an example showing the horizon angle of the upper arm.

$$\theta_{seg} = sign\left(z_{dist} - z_{prox}\right)\arctan 2\left(\frac{\sqrt{\left(y_{prox} - y_{dist}\right)^2 + \left(z_{prox} - z_{dist}\right)^2}}{x_{prox} - x_{dist}}\right) \qquad (5.2)$$

z

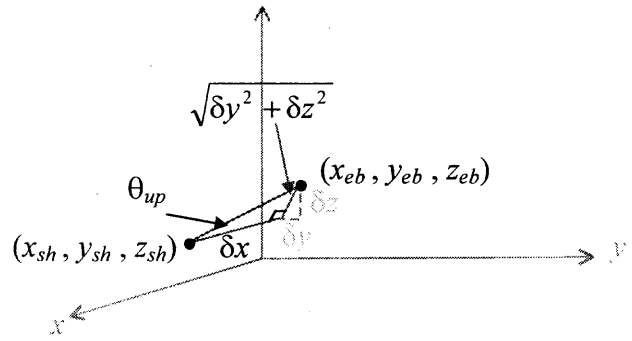

Figure 5.2 Calculation of the horizon angle of the upper arm

The dynamic horizon angles of Piston Cycle 1, as determined from filtered, projected VICON data, are given below in Figure 5.3. A counterclockwise (positive) upper arm angle indicates that this arm segment is above the horizon. This is comparable to shoulder joint extension. Note that the wheel completes almost two revolutions in one complete stroke cycle.

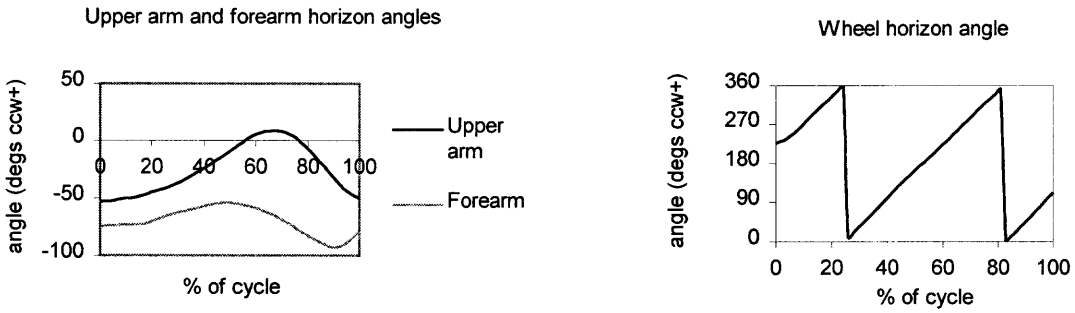

Figure 5.3 Piston Cycle 1 dynamic horizon angles of the upper arm, forearm, and wheel

5.4.2 Anatomical Joint Angles

Once the anatomical joint centers are projected into the sagittal plane, the anatomical joint angles can be found immediately. To find α_{jt}, the angle between two given segments (the two-dimensional analog of flexion/extension), two vectors, $\vec{v}_{prox}$ and $\vec{v}_{dist}$, are needed. When determining the shoulder *flexion* angle, $\vec{v}_{prox}$ is the trunk vector (from the shoulder joint center to L5) and $\vec{v}_{dist}$ is the upper arm vector (from the shoulder joint center to the elbow joint center). When finding the elbow *flexion* angle, $\vec{v}_{prox}$ is the upper arm vector (from the elbow joint center to the shoulder joint center) and $\vec{v}_{dist}$ is the forearm vector (from the elbow joint center to the wrist joint center). Once these vectors are calculated, Equation 5.3 is used to determine the desired joint angle.

$$\alpha_{jt} = \cos^{-1}\left(\frac{\vec{v}_{prox} \cdot \vec{v}_{dist}}{\left|\vec{v}_{prox}\right|\left|\vec{v}_{dist}\right|}\right) \tag{5.3}$$

Note that the joint angles and the horizon angles are related in that $\left(\alpha_{eb} - \left|\theta_{fore}\right|\right) + \left|\theta_{up}\right| = 180^{\circ}$, as illustrated in Figure 5.4. This inherit dependence can be used to determine anatomical joint angles from model output horizon angles, since $\alpha_{jt} = 180^{\circ} - \left|\theta_{prox}\right| + \left|\theta_{dist}\right|$.

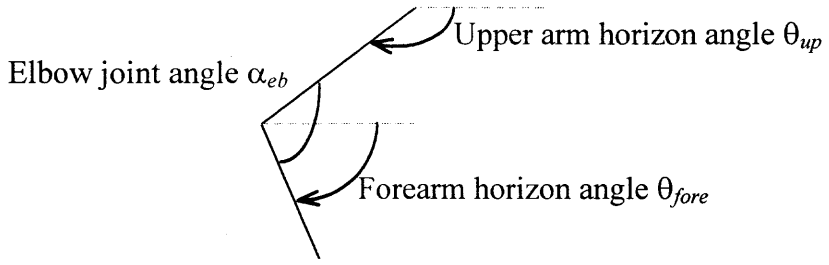

Figure 5.4 The inherent relationship between the joint angle and the angles of its proximal and distal segments

In Figure 5.5, the two-dimensional shoulder and joint angles of Piston Cycle 1 are graphed. For comparison, the three-dimensional shoulder and elbow flexion/extension angles are indicated in light gray.

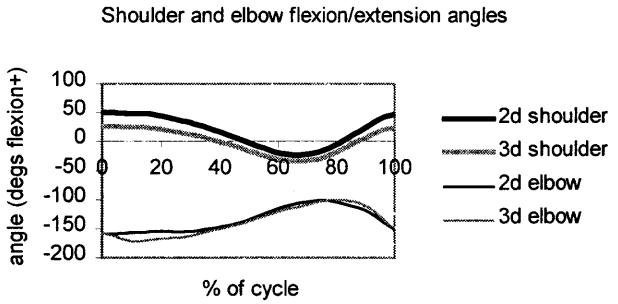

Figure 5.5 Piston Cycle 1 dynamic joint angles of the shoulder and elbow

5.4.3 Pushrim Contact Angle

The athlete's body comes into contact with the pushrim at the onset of push. They remain in contact until the end of push, namely *release*. While they are in contact, an angle is formed between the forearm segment and the line segment joining the wheel hub

(projected into the sagittal plane) and the point of contact on the pushrim. Figure 5.6 provides an illustration of this angle, the pushrim contact angle, α_{wh}.

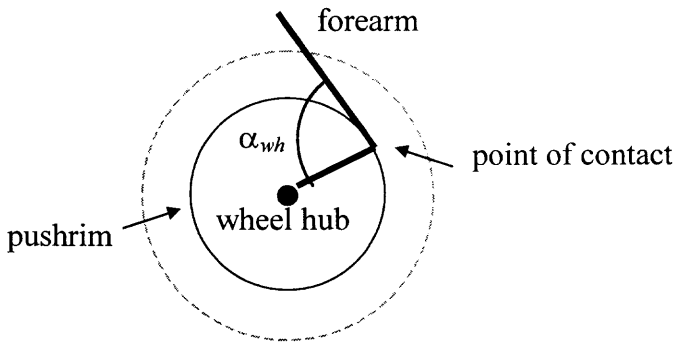

Figure 5.6 The pushrim contact angle, α_{wh}

This angle, the pushrim contact angle, varies during the push phase. It is approximated by assuming that the wrist joint center is the body part which makes contact with the pushrim. For model output, the pushrim contact angle is an immediate consequence of the horizon angles in that $\alpha_{wh} = 180^{o} - |\theta_{wh}| + |\theta_{fore}|$. For projected joint center data, Equation 5.4 gives the formula for the angle where $\vec{a}_{fore}$ is the vector from the wrist joint center to the elbow joint center and $\vec{a}_{wh}$ is the vector from the wrist joint center to the projected wheel hub. In the Piston Cycle 1 trial, the two-dimensional wheel contact angle is 82.2°.

$$\alpha_{wh} = \cos^{-1}\left(\frac{\vec{a}_{fore} \cdot \vec{a}_{wh}}{|\vec{a}_{fore}||\vec{a}_{wh}|}\right) \tag{5.4}$$

5.5 Energy Calculations on Two-Dimensional Data

Expressions for components of the system's total mechanical energy, including the potential energy and kinetic energy of the body segments and the wheel, are given in this section. These expressions can be used to determine mechanical energies for both model output and for projected, filtered VICON data.

5.5.1 Wheelchair Energy Calculations

Since experimental racing conditions, and not actual road racing, are being modeled, only the wheels of the chair move. Once again, the system's mass, which is not accounted for by the segments, will be used in wheelchair energy calculations. It is assumed that this mass, m_{rest}, is equally distributed at the two hubs.

In two dimensions, the wheel is a circular lamina with a given radius. Each wheel's center of mass is located at the center of its circle (its hub). To compute the chair's potential energy, hub height is needed. Projected, filtered VICON data includes hub height. On the other hand, model output consists of theoretical segment angles. Therefore, simple trigonometric relationships along with known segment lengths must be used to determine the height of the hub in this case. The wheel's potential energy is given by $V_{wh} = g\left(m_{wh} + \frac{1}{2}m_{rest}\right)(\text{hub height})$.

Assuming no-slip conditions, the athlete/chair system will move forward at the same rate as the wheels. However, in the CompuTrainer setup, the chair does not translate since it remains in a fixed position throughout the entire racing stroke. Therefore, the translational kinetic energy of the athlete/chair system is zero.

To determine the kinetic energy of the wheel caused by rotation, its angular velocity, ω_{wh}, is needed. The wheel's angular velocity at a specific time, $\omega_{wh}(t)$ is calculated by applying the finite difference scheme given by Equation 5.5 to dynamic wheel horizon angle data[1].

$$\omega_{wh}(t) = \frac{\omega_{wh}(t + \Delta t) - \omega_{wh}(t - \Delta t)}{2\Delta t} \tag{5.5}$$

A circular lamina has a moment of inertia about its center (its *polar moment of inertia*) equal to half the product of the radius squared and the mass. Therefore, a wheel's rotational kinetic energy at time t is determined by Equation 5.6, where m_{wh} is the mass of the wheel and v_{wh} is the wheel's velocity.

$$T_{wh}(t) = \frac{1}{2} I_{wh} \omega_{wh}^{2}(t) = \frac{1}{2}\left(\frac{m_{wh} r_{wh}^{2}}{2}\right) \omega_{wh}^{2}(t) = \frac{1}{4} m_{wh} v_{wh}^{2}(t) \tag{5.6}$$

Figures 5.7 and 5.8 indicate the results of an analysis of Piston Cycle 1 data. As in the three-dimensional analysis of this empirical data, the wheelchair potential energy is nearly constant and the initial kinetic energy of the wheel is minimal. For comparison, the three-dimensional wheel energies are indicated in light gray.

[1] The wheel horizon angles are determined for experimental data as described in Section 5.4.1 or else are given by model output.

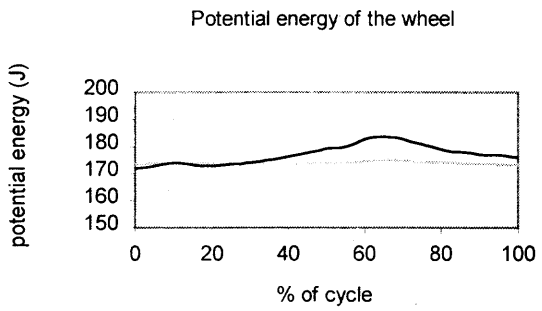

Figure 5.7 The wheel's potential energy in Piston Cycle 1

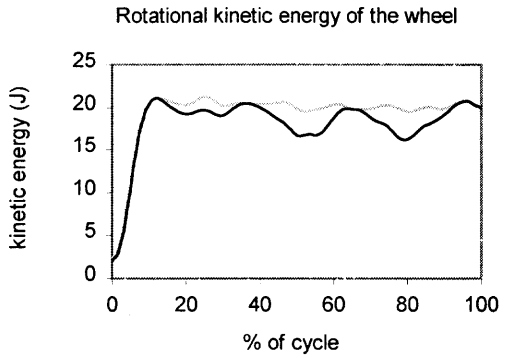

Figure 5.8 The wheel's kinetic energy in Piston Cycle 1

5.5.2 Body Segment Energy Calculations

As was mentioned previously, there are two possible idealizations of body segments considered in this thesis, point-mass or distributed-mass. Each body segment is assumed to be a simple point mass in the two-dimensional analysis for the reasons given at the end of Section 4.5.2. To compute the potential energy of a point-mass body segment, its mass and the height of its center of mass are needed. The horizon angles from projected, filtered VICON data or from the model, in conjunction with segment masses, lengths, locations of centers of mass, basic trigonometry, and a specified global origin enable the calculation of this height. The derivation of the formula for the potential energy of a

given segment is included in Section 6.4. Basically, $V_{seg} = mg(\text{c.o.m. height})$, where c.o.m. height denotes the height of the segment's center of mass.

In order to find a given segment's rotational kinetic energy, all segments' structural parameters, horizon angles, and horizon angle velocities are needed. Note that only one angle – the horizon angle – is needed to locally orient a segment in two-dimensional space. This is because there are three degrees of freedom in this case: a point (x,y) to locate the center of mass and one angle, θ , to orient it from the horizontal.

For projected data and for model output, the horizon angles are calculable or given, respectively. The angular velocities are then found by applying the finite difference scheme given by Equation 5.7 in which $\theta(j)$ is the segment angle at time j to these horizon angles.

$$\omega_{seg}(t) := \frac{d\theta(t)}{dt} = \frac{\theta(t+\Delta t)-\theta(t-\Delta t)}{2\Delta t} \tag{5.7}$$

Detailed derivation of the formulae for the body segments' kinetic energies is presented in Section 6.4. For completeness in this chapter, expressions for the potential energy and the rotational kinetic energy of the upper arm and forearm segments in the point-mass model are given in Table 5.1. In the table, the following abbreviations are used:

m_{seg} = segment mass (kg) $\qquad$ l_{seg} = segment length (m)

θ_{seg} = segment horizon angle $\qquad$ $\dot{\theta}_{seg}$ = segment horizon angle velocity

z_{seg} = location of segment c.o.m. from proximal end (m)

Table 5.1 Formulae for the potential and rotational kinetic energies of the upper arm and forearm point-mass segments

Point-Mass Model	Upper Arm Segment	Forearm Segment
Potential Energy	$m_{up} g z_{up} \sin\theta_{up}$	$m_{fore} g\left(L_{up} \sin\theta_{up} + z_{fore} \sin\theta_{fore}\right)$
Kinetic Energy	$\frac{1}{2} m_{up} z_{up}{}^2 \dot{\theta}_{up}{}^2$	$\frac{1}{2} m_{fore}\left[z_{fore}{}^2 \dot{\theta}_{fore}{}^2 + l_{up}{}^2 \dot{\theta}_{up}{}^2 + 2 l_{up} z_{fore} \cos\left(\theta_{up} - \theta_{fore}\right) \dot{\theta}_{up} \dot{\theta}_{fore}\right]$

Figures 5.9 through 5.12 present the energies of the arm segments and of the athlete/chair system in Piston Cycle 1 data. For comparison, corresponding three-dimensional energies are indicated in light gray.

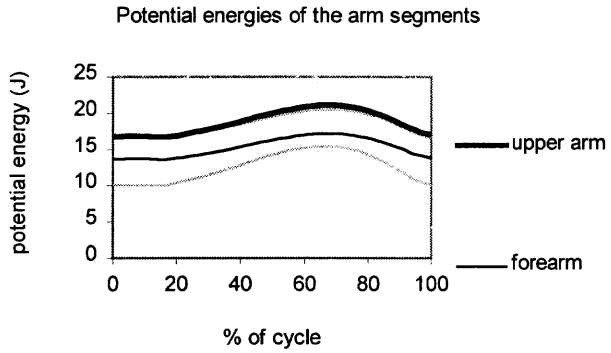

Figure 5.9 Potential energies of the arm segments in Piston Cycle 1

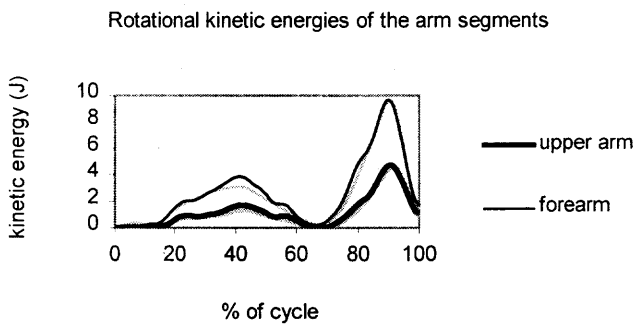

Figure 5.10 Rotational kinetic energies of the arm segments in Piston Cycle 1

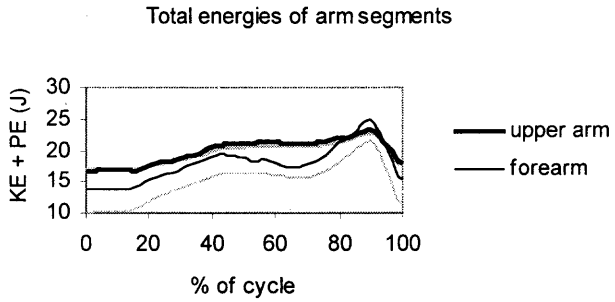

Figure 5.11 Total energies of the arm segments in Piston Cycle 1

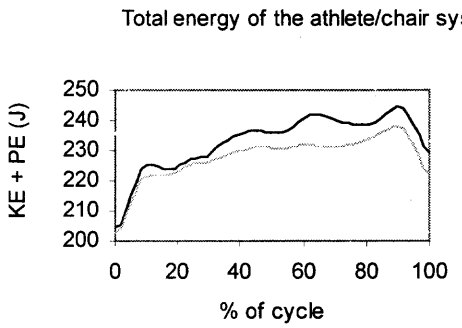

Figure 5.12 Total energy of the athlete/chair system in Piston Cycle 1

CHAPTER 6

THE MATHEMATICAL MODEL: THE BASIC COMPONENTS

6.1 The Approach

The model used in this thesis is an extension of the Motion Analysis Performance System (MAPS) model developed by Lacker and colleagues (1997), which was originally utilized to find an individual's optimal gait pattern. As an extension, the model will follow the same basic approach employed by MAPS. The MAPS approach has the advantage over more traditional (inverse) methods that are commonly used in modeling motion in that it does not require extensive kinematic data as model input. It also allows for the attainment of a complete set of solutions that can accomplish a desired physical task, which are all consistent with a given individual's structural parameters including the segment masses, lengths, and locations of the centers of mass.

In this model, the stroke is considered to be symmetric so that only one side of the athlete and racing chair system needs to be included. The human body is idealized to be an inelastic, two-dimensional, n-1-segment, coupled-pendulum system in which each pendulum represents a body segment. Because the model is two-dimensional, the effects of movement out of the sagittal plane will not be captured. In this way, this modeling attempt is a first approximation. Furthermore, the pendulums are represented as simple point masses, rather than distributed masses. The wheelchair is modeled as one segment, the wheel, which is represented as a uniform disk. The wheel additionally has half the mass of the athlete/chair system not accounted for by the n segments, located at each hub. The disk is attached to the end of the body segment system.

Wheelchair racing, like walking, is a cyclic motion. It may be reasonable to assume that the *best* stroke technique, which is to be repeated continually over the whole race, would be the one, which has the least mechanical energy cost per unit distance traveled. The *best* stroke would plausibly have two primary ingredients. First, the athlete's arm segments would be moved in an *efficient* way. Secondly, the racer would conserve energy by using muscles only at *optimal* times during the stroke cycle to impart necessary propulsive and/or braking forces. If these two conditions were to be met, the mechanical energy cost could conceivably be minimal, resulting in peak performance.

In modeling the racing stroke, this idea is taken into account. The main assumption of the model is that the wheelchair racing stroke can be captured by dissecting the entire cycle into an arbitrary number of consecutive phases, at the beginning of which impulsive forces supplied by the muscles are allowed to occur. That is, the only times that muscular energy can be supplied during the stroke cycle is at the boundaries of the prescribed phases. Although this is an extreme simplification of how human motion occurs, the close correlation of MAPS theoretical gait output with experimental gait data indicates that this method may be a good first approximation in modeling a cyclic motion (Choi 1997). A fundamental contribution toward enhancing this sport would be to determine where these phases should occur (that is, how to partition the entire stroke cycle into phases – when the muscles should be used – for maximal mechanical energy efficiency).

A phase consists of an initial configuration, a final configuration, and a time duration. An initial or final configuration consists of the locations and orientations of all modeled segments (both body and chair) at the onset or end of the phase, respectively.

Once the phases are established, Lagrange equations of motion for the human/wheelchair system will be applied. These equations will be constrained when the athlete is contacting the pushrim of the wheel (during what is clinically called *push*) or when a joint's extreme range of motion is attained. The equations will be unconstrained immediately following pushrim release and up until the next pushrim contact (during *recovery*) provided that no joint extreme range of motions are encountered.

The Lagrangian equations are second-order, nonlinear, ordinary differential equations. Together with the time duration and initial and final configurations provided by a given phase, the equations of motion create a well-posed, two-point boundary value problem (BVP). This BVP is solved via numerical methods for each phase, and the solutions are concatenated to simulate the complete continuous stroke motion. The mechanical energy cost per unit distance traveled is calculated for the output model solution.

Each racing stroke, whether it is experimentally performed or produced by the model, is characterized by several independent motion parameters, for example wheel velocity, cycle time, maximum shoulder elevation angle, and wheel contact angle. If there are P stroke parameters, then simultaneously varying all of them over a range consistent with the athlete's physical capabilities, produces a P-dimensional *motion space*. Every point in this space represents a racing stroke technique characterized by those P parameters. Thus, systematically varying the P quantities allows for the determination of all racing stroke cycles that an individual is capable of doing. Moreover, each of these techniques has a calculated mechanical energy cost per unit

distance. Searching this P-dimensional motion space or a specified subset of it allows for the determination of the most energy-efficient technique.

6.2 The Human Body Structure

As was stated in the previous section, the body is represented as an inelastic, coupled-pendulum system in two dimensions. As a first approximation, each pendulum is simply a point mass located at a model-input specified distance from its pivot point.

In the model, segment masses and lengths are required input. Each segment's mass is calculated as a percent of total body mass of the athlete to be modeled according to anthropometric table data (Dempster 1955). Furthermore, each segment's length is measurable on the individual. The location of the center of mass of each segment must also be specified and is supplied by tables.

The number of body segments (and, therefore, joints) included in the model is allowed to vary depending on the athlete whose stroke is being investigated. This is possible because the model uses a general relationship matrix, described below, to identify how the segments are related to one another. This is an important feature when simulating the motion of wheelchair racers, as these spinal-cord-injured individuals have diverse degrees of functionality.

For example, it is sufficient to model a person with a high-level spinal cord injury (who has no control over the abdominal muscles) by considering only two body segments – namely, an upper arm and a forearm. The trunk does not have to be included in this case because it cannot move during the stroke cycle. In fact, the trunk remains stationary throughout the movement, lying on the motionless legs for support. On the other hand, to

simulate the stroke of a racer with a lower-level injury (who is capable of producing trunk motion) three body segments are used – a trunk, an upper arm, and a forearm. The ability to move the trunk enables the athlete to produce a pump-like motion with this segment throughout the stroke.

Once the number of segments is assigned, they, represented as pendulums, are attached to one another in a specific order. One segment is designated to be the *root segment* of the system. The origin of the coordinate system is located at a specified end (either proximal or distal) of the root segment. From this root segment grows a general tree structure in which each segment has specific ancestors and descendants. In travelling from a given segment to the root, any segment traversed is an *ancestor*. Any segment that considers a given segment as its ancestor is known as a *descendant*. This vocabulary is illustrated in the three-segment, point-mass model of Figure 6.1.

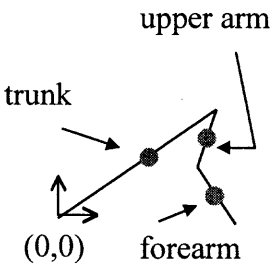

The trunk is the *root* segment. It has no *ancestors*. Its *descendants* are the upper arm and the forearm.

The *ancestor* of the upper arm is the trunk and its *descendant* is the forearm.

The forearm's *ancestors* are the upper arm and the trunk. It has no *descendants*.

Figure 6.1 An illustration of *ancestors* and *descendants*

This segment-relationship formulation is used to easily determine the equations of motion for a general branched-tree structured system (Choi 1997). The specifics of this approach are discussed in Section 6.4.

6.3 The Racing Wheelchair Structure

Since the model output is to be compared with empirical data collected on the CompuTrainer, the racing chair can be represented in simplified form[1]. Once again, athlete/chair movement symmetry is assumed and only one side is considered. This half chair is represented in the model simply as one uniform disk, which has an additional mass of $\frac{1}{2}m_{rest}$, half of the athlete/chair system mass not accounted for by the n segments, located at its hub. Chair structural input required by the model includes the wheel's mass, full radius, and pushrim radius, as well as the total mass of the athlete/chair system, which are all readily measurable.

An additional parameter needed as model input is the orientation of the athlete in the chair. Specifying the location of the origin of the system's root segment relative to the hub of the wheel will furnish this information. It is also determinable by identifying an initial or final configuration of the system.

6.4 The Equations of Motion

Since the purpose of this model is to determine possible paths of motion for the athlete/wheelchair system, it is necessary to develop equations of motion, which are then solved to give possible trajectories of the body segments and the wheel. There are several formulations of the fundamental laws of dynamics, which can be used to determine these equations. In this model, the Lagrangian approach is followed.

---

[1] If road-racing conditions were to be modeled, a more complicated version of the wheelchair would have to be utilized. This enhanced version would consider the chair as a combination of wheels and rigid bodies maintained at fixed orientations to each other.

In order to develop the equations of motion via the Lagrangian method, the first necessary step is to choose appropriate independent generalized coordinates. In an *n*-coupled pendulum system whose two-dimensional motion is being considered, there are *n* degrees of freedom when the motion is unconstrained and *n-k* degrees of freedom when there are *k* independent equations of constraint. The *n* generalized coordinates are chosen to be the angles the segments make with the horizontal (the *horizon angles*), where counterclockwise is considered positive. This choice is illustrated in the four-segment point mass / disk model of Figure 6.2.

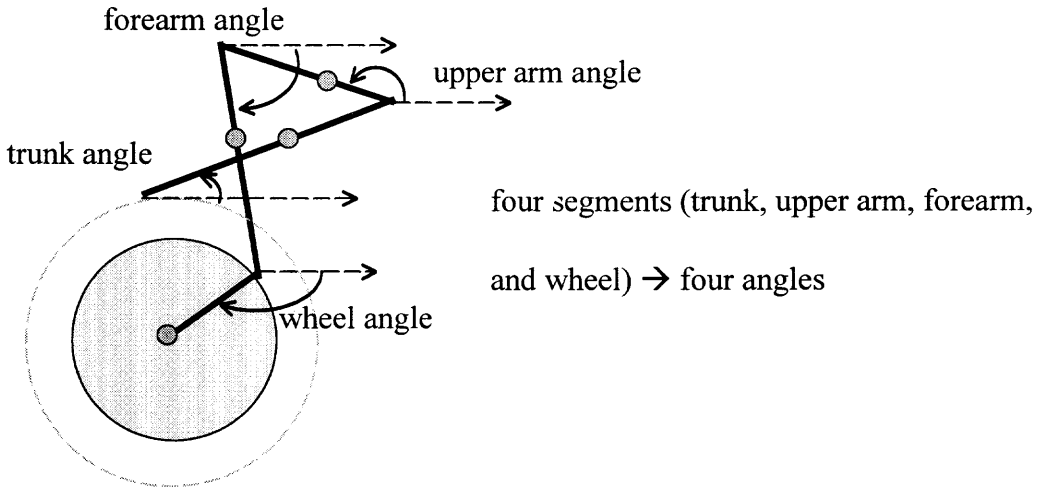

Figure 6.2 The dynamic horizon angles in a four-segment, point-mass/disk model

In modeling the wheelchair/racer system, the local origin is at a specified end of the root segment. From this origin, the location of all segments' centers of mass can be described via the dynamic horizon angles and model-input structural parameters. It is important to note that when the racer is not in contact with the wheel (that is, during

recovery – unconstrained motion), the motion of the racer and the chair (the wheel) are considered separately. However, when the racer is pushing the wheel (during *push* – constrained motion) the coupled motion of the racer and the chair is examined.

To derive the Lagrange equations of motion, expressions for the potential and kinetic energies of the system are needed. These expressions will be derived as generally as possible in this section. During push, it is assumed that the system consists of a point-mass pendulum system (the body segments and the point mass at the hub of the wheel), which has a distributed-mass wheel segment attached to its terminal end (at the hub). On the other hand, two separate systems are considered during recovery. The first is a point-mass pendulum system consisting of the body segment point masses and the point mass located at the wheel hub, and the second is a disk wheel segment.

Expressions for the energies of any given point-mass pendulum system will be derived first, which is sufficient for obtaining the recovery phase's equations of motion. This derivation will be followed by the determination of the energies of a disk wheel, which are necessary to include in finding the push phase's equations of motion.

Consider a pendulum system made up of s segments. Let each segment be represented by a discrete number of point masses so that there are a total of p point masses in the system. Choi (1997) used a $p \times s$ relation matrix $\mathbf{R}$ to express the relationship between the s segments. Given that the i^{th} point mass is on segment m, $\mathbf{R}$'s components are defined as follows:

$$r_{ij} = \begin{cases} l_j & \text{if the } m^{\text{th}} \text{ segment is a descendant of the } j^{\text{th}} \text{ segment} \\ z_i & \text{if } j = m \\ 0 & \text{otherwise} \end{cases}$$

where l_j is the length of the j^{th} segment (model input), z_i is the distance from the m^{th} segment's end closest to the root segment to the i^{th} point mass, i ranges from 1 to p, and j ranges from 1 to s. Note that **R** 's p rows contain information about the point masses in the system and its s columns concern the segments.

For example, consider the system represented in Figure 6.3 below. In the figure, R_p indicates the radius of the pushrim.

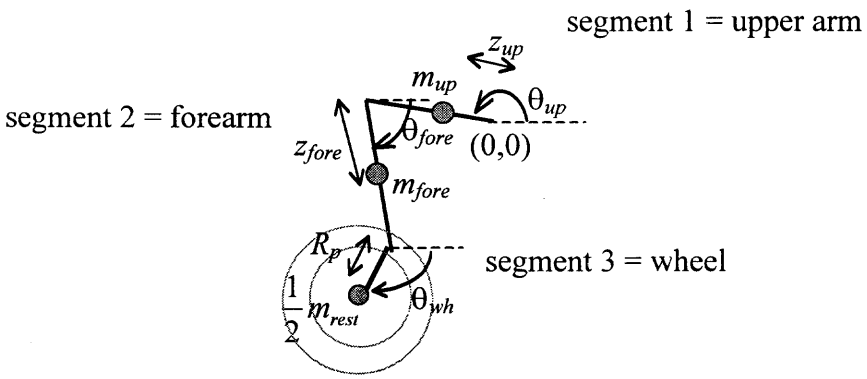

Figure 6.3 The three-segment, point-mass / disk wheel model

Temporarily ignoring the distributed-mass wheel in Figure 6.3, the relation matrix of the three-segment, point-mass system is as follows:

$$\mathbf{R} = \begin{bmatrix} z_{up} & 0 & 0 \\ L_{up} & z_{fore} & 0 \\ L_{up} & L_{fore} & R_p \end{bmatrix} \qquad (6.1)$$

The x- and y-coordinates of p point masses located on *any* branched-tree, s-segment system are now concisely expressed as follows:

$$\vec{x} = \left(x_1 \ldots x_p\right)^T = \mathbf{R}\left(\cos\theta_1 \ldots \cos\theta_s\right)^T \tag{6.2}$$

and

$$\vec{y} = \left(y_1 \ldots y_p\right)^T = \mathbf{R}\left(\sin\theta_1 \ldots \sin\theta_s\right)^T \tag{6.3}$$

where θ_i is the horizon angle of the i^{th} segment (time-dependent; model output).

The x- and y-components of the velocities of these point masses are obtained by differentiating their x- and y-coordinates with respect to time. Therefore, the velocity components are as follows:

$$\dot{\vec{x}} = \left(\dot{x}_1 \ldots \dot{x}_p\right)^T = -\mathbf{R}\ \sin\Theta\ \dot{\Theta} \tag{6.4}$$

and

$$\dot{\vec{y}} = \left(\dot{y}_1 \ldots \dot{y}_p\right)^T = \mathbf{R}\ \cos\Theta\ \dot{\Theta} \tag{6.5}$$

where $\sin\Theta$ and $\cos\Theta$ are defined to be diagonal matrices with nonzero elements $\sin\theta_1 \ldots \sin\theta_s$ and $\cos\theta_1 \ldots \cos\theta_s$ respectively and $\dot{\Theta} = \left(\dot{\theta}_1 \ldots \dot{\theta}_s\right)^T$.

Equations 6.2 through 6.5 enable the concise expression of the potential and kinetic energies of any branched-tree structure, point-mass segment pendulum system. The pendulum system's potential energy is found by summing the potential energy of all

point masses. Therefore, the potential energy of the point-mass pendulum system is given by Equation 6.6 in matrix form.

$$V_{pt\ mass} = \sum_{i=1}^{p} g m_i y_i = g\, \bar{y}^T\, \mathbf{M}\, \vec{1}^T = g\,(\sin\theta_1 \ldots \sin\theta_s)\mathbf{R}^T\, \mathbf{M}\, \vec{1}^T \qquad (6.6)$$

where $\vec{1}$ is a $1 \times p$ vector of ones and $p \times p$ mass matrix $\mathbf{M}$ has nonzero elements equal to the masses of the points on its diagonal. For example, the diagonal mass matrix of the point-mass system in Figure 6.3 is as follows:

$$\mathbf{M} = \begin{bmatrix} m_{up} & 0 & 0 \\ 0 & m_{fore} & 0 \\ 0 & 0 & \frac{1}{2} m_{rest} \end{bmatrix} \qquad (6.7)$$

Performing the multiplication in Equation 6.6 gives the potential energy of the point-masses of the body segments in summation form. This is as follows:

$$V_{pt\ mass} = g \sum_{i=1}^{p} \sum_{j=1}^{s} m_i r_{ij} \sin\theta_j \qquad (6.8)$$

The kinetic energy of the pendulum system is similarly found by summing up the kinetic energies of all point masses and is expressible in matrix form. It is derived as follows:

$$T_{pt\,mass} = \frac{1}{2}\sum_{i=1}^{p} m_i\left(\dot{x}_i^{\,2} + \dot{y}_i^{\,2}\right) = \frac{1}{2}\left(\dot{\bar{x}}^{T}\,\mathbf{M}\,\dot{\bar{x}} + \dot{\bar{y}}^{T}\,\mathbf{M}\,\dot{\bar{y}}\right)$$

$$= \frac{1}{2}\left[\dot{\Theta}^{T}\,(\sin\Theta)^{\mathrm{T}}\;\mathbf{R}^{T}\,\mathbf{M}\,\mathbf{R}\sin\Theta\;\dot{\Theta} + \dot{\Theta}^{T}\,(\cos\Theta)^{\mathrm{T}}\;\mathbf{R}^{T}\,\mathbf{M}\,\mathbf{R}\cos\Theta\;\dot{\Theta}\right]$$

$$= \frac{1}{2}\left[\dot{\Theta}^{T}\,(\sin\Theta)^{\mathrm{T}}\;\mathbf{C}\sin\Theta\;\dot{\Theta} + \dot{\Theta}^{T}\,(\cos\Theta)^{\mathrm{T}}\;\mathbf{C}\cos\Theta\;\dot{\Theta}\right]$$

$$= \frac{1}{2}\dot{\Theta}^{T}\left[\,(\sin\Theta)^{\mathrm{T}}\;\mathbf{C}\sin\Theta\;+\;(\cos\Theta)^{\mathrm{T}}\;\mathbf{C}\cos\Theta\right]\dot{\Theta}$$

where the symmetric $s \times s$ matrix $\mathbf{C} = \mathbf{R}^{T}\,\mathbf{M}\,\mathbf{R}$, making its elements $c_{ij} = \sum_{k=1}^{p} m_k r_{ki} r_{kj}$.

Furthermore, let $M = (\sin\Theta)^{T}\;\mathbf{C}\;\sin\Theta + (\cos\Theta)^{T}\;\mathbf{C}\cos\Theta$. Then by trigonometric identities, its elements are $\mu_{ij} = c_{ij}\cos(\theta_i - \theta_j)$. With this symmetric new matrix, the kinetic energy of the point-mass pendulum system is given by Equation 6.9 in matrix form.

$$T_{pt\,mass} = \frac{1}{2}\dot{\Theta}^{T} M\,\dot{\Theta} \tag{6.9}$$

Performing the matrix multiplication of Equation 6.9 gives the pendulum system's kinetic energy in summation form. This is as follows:

$$T_{pt\,mass} = \frac{1}{2}\sum_{k=1}^{p} m_k\left(\sum_{i=1}^{s}\sum_{j=1}^{s} r_{ki} r_{kj}\cos(\theta_i - \theta_j)\dot{\theta}_i\dot{\theta}_j\right) \tag{6.10}$$

Next, the energy contributions from the wheel segment's distributed mass must be found. For the following calculations, the disk wheel is attached at the terminal end of the point-mass pendulum system, which is the hub. The hub is not assumed to remain at a fixed location, which means that it is free to move in the plane. In Section 6.5, details will be given for imposing this constraint.

To obtain an expression for the potential energy present in the disk wheel, an integral must be evaluated. Let *dm* be a small element of mass on the wheel as indicated in gray in Figure 6.4. Note that any small section of the wheel *dm* can be located by the variables *r*, the radial distance from the hub, and θ, the variable angle from the horizontal with the hub.

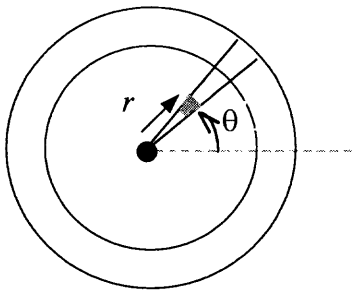

Figure 6.4 A small section of mass on the disk wheel indicated in gray

Since the disk wheel has uniform density, $\rho = \frac{m_{wh}}{\pi R_{wh}^{\ 2}}$. Also,

$dm = \rho dA = \rho r dr d\theta$. The potential energy of the disk is calculated as follows:

$$V_{disk\ wheel} = g\int dm\ (\text{height of } dm) = g\frac{m_{wh}}{\pi R_{wh}^{\ 2}}\int_0^{2\pi}\int_0^{R_{wh}}(\text{hub height} + r\sin\theta)\,r\,dr\,d\theta$$

$$= g\frac{m_{wh}}{\pi R_{wh}^{\ 2}}\int_0^{2\pi}\left(\frac{R_{wh}^{\ 2}}{2}\text{hub height} + \frac{R_{wh}^{\ 3}}{3}\sin\theta\right)d\theta$$

$$= g\frac{m_{wh}}{\pi R_{wh}^{\ 2}}2\pi\frac{R_{wh}^{\ 2}}{2}\text{hub height} = g\,m_{wh}\ \text{hub height}$$

Recall from Equation 6.6 or 6.8 that the point mass at the hub of the wheel has potential energy equal to $g\left(\frac{1}{2}m_{rest}\right)$ hub height. Therefore, the wheel's total potential energy is given by $g\left(m_{wh}+\frac{1}{2}m_{rest}\right)\sum_{j=1}^{s} r_{ij}\sin\theta_j$ where the i^{th} segment is the wheel and the r_{ij} are elements of the point-mass pendulum system's relation matrix **R**. Note that this adds only the quantity $gm_{wh}\sum_{j=1}^{s} r_{ij}\sin\theta_j$ (where *i* indicates the wheel segment) to the potential energy of the point-mass pendulum system given in Equation 6.8. This suggests modifying the wheel segment's point-mass element in the diagonal mass matrix **M** of Equation 6.7 so that it becomes $m_{wh}+\frac{1}{2}m_{rest}$ instead of just $\frac{1}{2}m_{rest}$.

Now the kinetic energy of the wheel's distributed mass must be calculated. Given that *k* indicates the wheel segment, the *x*- and *y*-coordinates of any point on the disk wheel are given by $\left(\sum_{j=1}^{s} r_{kj}\cos\theta_j + r\cos\theta, \sum_{j=1}^{s} r_{kj}\sin\theta_j + r\sin\theta\right)$, where again r_{kj} are from the point-mass pendulum system's relation matrix **R**. Differentiating the coordinates

with respect to time gives the x- and y-components of any point on the wheel's velocity as $\left(-\sum_{j=1}^{s} r_{kj} \sin\theta_j \dot{\theta}_j - r \sin\theta \dot{\theta}, \sum_{j=1}^{s} r_{kj} \cos\theta_j \dot{\theta}_j + r \cos\theta \dot{\theta} \right)$. This means that a wheel point's velocity squared is given by Equation 6.11.

$$\sum_{i=1}^{s} \sum_{j=1}^{s} r_{ki} r_{kj} \cos(\theta_i - \theta_j) \dot{\theta}_i \dot{\theta}_j + 2 \sum_{j=1}^{s} r r_{kj} \cos(\theta - \theta_j) \dot{\theta} \dot{\theta}_j + r^2 \dot{\theta}^2 \qquad (6.11)$$

Although Equation 6.11 gives a wheel point's *linear* velocity, it is important to note that all points on the wheel have the same *angular* velocity about the hub, namely $\dot{\theta} = \dot{\theta}_{wh}$. To calculate the kinetic energy of the disk wheel, all wheel points' kinetic energies must be summed. Since there are an infinite number of points on the disk wheel, an integral is used to determine the disk wheel's kinetic energy. This derivation proceeds as follows:

$$T_{disk\ wheel} = \frac{1}{2}\int dm\,(\text{velocity of } dm)^2$$

$$= \frac{1}{2}\frac{m_{wh}}{\pi R_{wh}^{\ 2}}\int_0^{2\pi}\int_0^{R_{wh}}\left[\sum_{i=1}^{s}\sum_{j=1}^{s} r_{ki}r_{kj}\cos(\theta_i-\theta_j)\dot{\theta}_i\dot{\theta}_j + \sum_{j=1}^{s} rr_{kj}\cos(\theta-\theta_j)\dot{\theta}\dot{\theta}_j + r^2\dot{\theta}^2\right] r\,dr\,d\theta$$

$$= \frac{1}{2}\frac{m_{wh}}{\pi R_{wh}^{\ 2}}\int_0^{2\pi}\left[\frac{R_{wh}^{\ 2}}{2}\sum_{i=1}^{s}\sum_{j=1}^{s} r_{ki}r_{kj}\cos(\theta_i-\theta_j)\dot{\theta}_i\dot{\theta}_j + \frac{R_{wh}^{\ 3}}{3}\sum_{j=1}^{s} rr_{kj}\cos(\theta-\theta_j)\dot{\theta}\dot{\theta}_j + \frac{R_{wh}^{\ 4}}{4}\dot{\theta}^2\right] d\theta$$

$$= \frac{1}{2}\frac{m_{wh}}{\pi R_{wh}^{\ 2}}\left[\frac{R_{wh}^{\ 2}}{2}(2\pi)\sum_{i=1}^{s}\sum_{j=1}^{s} r_{ki}r_{kj}\cos(\theta_i-\theta_j)\dot{\theta}_i\dot{\theta}_j + \frac{R_{wh}^{\ 4}}{4}(2\pi)\dot{\theta}_{wh}^{\ 2}\right]$$

$$= \frac{1}{2}m_{wh}\left(\sum_{i=1}^{s}\sum_{j=1}^{s} r_{ki}r_{kj}\cos(\theta_i-\theta_j)\dot{\theta}_i\dot{\theta}_j + \frac{R_{wh}^{\ 2}}{2}\dot{\theta}_{wh}^{\ 2}\right)$$

where k represents the wheel segment.

From the point-mass pendulum system's kinetic energy expression in Equation 6.10, it is seen that the point mass at the hub of the wheel has kinetic energy equal to $\frac{1}{2}\left(\frac{1}{2}m_{rest}\right)\sum_{i=1}^{s}\sum_{j=1}^{s} r_{ki}r_{kj}\cos(\theta_i-\theta_j)\dot{\theta}_i\dot{\theta}_j$. Therefore, the wheel's total kinetic energy is given by $\frac{1}{2}\left[\left(m_{wh}+\frac{1}{2}m_{rest}\right)\sum_{i=1}^{s}\sum_{j=1}^{s} r_{ki}r_{kj}\cos(\theta_i-\theta_j)\dot{\theta}_i\dot{\theta}_j + m_{wh}\frac{R_{wh}^{\ 2}}{2}\dot{\theta}_{wh}^{\ 2}\right]$ where the k^{th} segment is the wheel and the r_{kl} are from the point-mass pendulum system's relation matrix $\mathbf{R}$. This means that the distributed mass of the wheel adds only the quantity

$\frac{1}{2}\left[m_{wh} \sum_{i=1}^{s} \sum_{j=1}^{s} r_{ki} r_{kj} \cos(\theta_i - \theta_j) \dot{\theta}_i \dot{\theta}_j + m_{wh} \frac{R_{wh}^2}{2} \dot{\theta}_{wh}^2 \right]$ to the kinetic energy of the point-mass system given in Equation 6.10. This suggests altering the relation and diagonal mass matrices given in Equations 6.1 and 6.7, respectively, so that the point-mass / disk wheel segment is represented appropriately. The necessary modification to the relation matrix of Equation 6.1 consists of adding a row at the bottom of the matrix with a nonzero element $\frac{R_{wh}}{\sqrt{2}}$ on the diagonal. The mass matrix of Equation 6.7 must be altered by replacing the wheel's point-mass element $\frac{1}{2} m_{rest}$ with $m_{wh} + \frac{1}{2} m_{rest}$ and by adding a row at the bottom with diagonal element m_{wh}. That is, for the system pictured in Figure 6.3, **R** and **M** will now be as follows:

$$\mathbf{R} = \begin{bmatrix} z_{up} & 0 & 0 \\ L_{up} & z_{fore} & 0 \\ L_{up} & L_{fore} & R_p \\ 0 & 0 & \frac{R_{wh}}{\sqrt{2}} \end{bmatrix} \tag{6.12}$$

and

$$\mathbf{M} = \begin{bmatrix} m_{up} & 0 & 0 & 0 \\ 0 & m_{fore} & 0 & 0 \\ 0 & 0 & m_{wh} + \frac{1}{2} m_{rest} & 0 \\ 0 & 0 & 0 & m_{wh} \end{bmatrix} \tag{6.13}$$

With these new matrices, the potential energy of the point-mass / disk wheel system can be expressed as given by Equation 6.6 provided that the $1 \times p$ vector $\vec{1}$

becomes $\tilde{1}$, a vector of ones except for a zero as its p^{th} element. Moreover, the system's kinetic energy can be expressed exactly as given by Equation 6.9. In summary then, Equations 6.14 and 6.15 describe the energies of the whole point-mass / disk wheel system.

$$V_{sys} = g(\sin\theta_1 \ldots \sin\theta_s)\mathbf{R}^T\mathbf{M}\tilde{1}^T \tag{6.14}$$

$$T_{sys} = \frac{1}{2}\dot{\Theta}^T M \dot{\Theta} \tag{6.15}$$

Now that the kinetic and potential energies of the point-mass / disk wheel system have been derived, equations of motion will be obtained via the Lagrangian approach. In general, given a system described by s independent variables (for example, the horizon angles of the s segments), the Lagrangian equations of motion are given by Equation 6.16 (Wells 1967). The terms on the right hand side are generalized forces acting on the system in the θ_i direction. They will be examined in depth at a later point.

$$\frac{d}{dt}\left(\frac{\partial T_{sys}}{\partial \dot{\theta}_i}\right) - \frac{\partial T_{sys}}{\partial \theta_i} = Q_{\theta_i} + Q^c_{\theta_i} \quad \text{for } i = 1,\ldots,s \tag{6.16}$$

To obtain the terms on the left-hand side of Equation 6.16, derivatives of the system's kinetic energy are needed. These are as follows:

$$\frac{d}{dt}\left(\frac{\partial T_{sys}}{\partial \dot{\theta}_i}\right) = \frac{d}{dt}\left[\frac{\partial}{\partial \dot{\theta}_i}\left(\frac{1}{2}\dot{\Theta}^T M \dot{\Theta}\right)\right] = \frac{d}{dt}\left[\frac{1}{2}\sum_{j=1}^{s}\left(\mu_{ij}\dot{\theta}_j + \mu_{ji}\dot{\theta}_j\right)\right]$$

$$= \frac{d}{dt}\left(\sum_{j=1}^{s}\mu_{ij}\dot{\theta}_j\right) = \sum_{j=1}^{s}\left[-c_{ij}\sin(\theta_i - \theta_j)(\dot{\theta}_i - \dot{\theta}_j)\dot{\theta}_j + \mu_{ij}\ddot{\theta}_j\right] \tag{6.17}$$

$$\frac{\partial T_{sys}}{\partial \theta_i} = \frac{\partial}{\partial \theta_i}\left(\frac{1}{2}\dot{\Theta}^T M \dot{\Theta}\right) = \frac{1}{2}\sum_{j=1}^{s}\left[-c_{ij}\sin(\theta_i - \theta_j)\dot{\theta}_i\dot{\theta}_j + c_{ji}\sin(\theta_j - \theta_i)\dot{\theta}_j\dot{\theta}_i\right]$$

$$= -\sum_{j=1}^{s}c_{ij}\sin(\theta_i - \theta_j)\dot{\theta}_i\dot{\theta}_j \tag{6.18}$$

Substituting these derivatives into the Lagrangian equations of motion given by Equation 6.16 produces the equation

$$\sum_{j=1}^{s}\left[-c_{ij}\sin(\theta_i - \theta_j)(\dot{\theta}_i - \dot{\theta}_j)\dot{\theta}_j + \mu_{ij}\ddot{\theta}_j\right] - \left[-\sum_{j=1}^{s}c_{ij}\sin(\theta_i - \theta_j)\dot{\theta}_i\dot{\theta}_j\right] = Q_{\theta_i} + Q_{\theta_i}^c,$$

which simplifies to Equation 6.19 below. These are the Lagrangian equations of motion.

$$\sum_{j=1}^{s}\left[\mu_{ij}\ddot{\theta}_j + c_{ij}\sin(\theta_i - \theta_j)\dot{\theta}_j^2\right] = Q_{\theta_i} + Q_{\theta_i}^c \tag{6.19}$$

Now consider the terms on the right-hand side of Equation 6.19. The first term gives the net, non-conservative generalized force (due to gravity and, if included, joint viscosities) acting on the system in the θ_i direction. These generalized forces in the directions of the segment angles are expressible as linear combinations of F_{x_j} and F_{y_j},

forces acting on the p point masses in the x_j- and y_j- directions, respectively, for $j = 1,\ldots,p$. That is, they can be written as in Equation 6.20.

$$Q_{\theta_i}(t) = \sum_{j=1}^{p}\left(F_{x_j}(t)\frac{\partial x_j}{\partial \theta_i} + F_{y_j}(t)\frac{\partial y_j}{\partial \theta_i}\right) \tag{6.20}$$

Define an $s \times 1$ generalized force vector Q, an $s \times 2p$ coordinate change matrix A, and a $2p \times 1$ force vector F as follows:

$$Q = \begin{pmatrix} Q_{\theta_1} \\ \vdots \\ Q_{\theta_s} \end{pmatrix}, \quad A = \begin{bmatrix} \frac{\partial x_1}{\partial \theta_1} & \cdots & \frac{\partial x_p}{\partial \theta_1} & \frac{\partial y_1}{\partial \theta_1} & \cdots & \frac{\partial y_p}{\partial \theta_1} \\ & \vdots & & & \vdots & \\ \frac{\partial x_1}{\partial \theta_s} & \cdots & \frac{\partial x_p}{\partial \theta_s} & \frac{\partial y_1}{\partial \theta_s} & \cdots & \frac{\partial y_p}{\partial \theta_s} \end{bmatrix}, \text{ and } \quad F = \begin{pmatrix} F_{x_1} \\ \vdots \\ F_{x_p} \\ F_{y_1} \\ \vdots \\ F_{y_p} \end{pmatrix}$$

This notation allows Equation 6.20 to be expressed simply as $Q = AF$. Thus, the non-conservative generalized forces can be found by multiplying the coordinate transformation matrix by a force vector comprised of forces in the point masses' x- and y-directions. In this thesis, the only non-conservative generalized forces included are those provided by gravity. Furthermore, a generalized gravitational force in the θ_i direction can be expressed as in Equation 6.21 below.

$$Q_{grav\,\theta_i} = \sum_{j=1}^{p}\left(F_{x_j}\frac{\partial x_j}{\partial \theta_i} + F_{y_j}\frac{\partial y_j}{\partial \theta_i}\right) = \sum_{j=1}^{p}\left(0 - gm_j r_{ji}\cos\theta_i\right) = -g\sum_{j=1}^{p} m_j r_{ji}\cos\theta_i \tag{6.21}$$

Thus, the vector Q_{grav} is given as follows:

$$Q_{grav} = -g\left(\sum_{j=1}^{p} m_j r_{j1} \cos\theta_1 \quad \cdots \quad \sum_{j=1}^{p} m_j r_{js} \cos\theta_s \right)^T$$

$$= -g\,(\cos\Theta)^T \left(\sum_{j=1}^{p} m_j r_{j1} \quad \cdots \quad \sum_{j=1}^{p} m_j r_{js} \right)^T \tag{6.22}$$

$$= -g\,\cos\Theta\,\mathbf{R}^T \left(m_1 \quad \cdots \quad m_p \right)^T = -g\,\cos\Theta\,\mathbf{R}^T\,\mathbf{M}\,\tilde{1}^T$$

Defining Γ, an $s \times 1$ vector, as $g\,\mathbf{R}^T\mathbf{M}\,\tilde{1}^T$ allows the generalized gravitational forces to be expressed concisely. This abbreviation is used in Equation 6.23 below.

$$Q_{grav} = -(\cos\Theta)\,\Gamma \tag{6.23}$$

At this point, it is possible to write the Lagrangian equations of motion for an unconstrained system. These are given by Equation 6.24 below.

$$M\ddot{\Theta} + S\dot{\Theta}^2 = -(\cos\Theta)\,\Gamma \tag{6.24}$$

For a constrained system, the second term on the right-hand side of Equation 6.19 must be included. This term is the net generalized force in the θ_i direction *due to the constraints imposed on the system.* (More details on constraints are given in Section 6.5.) Given k constraints, $G_j(\theta_1,\ldots,\theta_s) = 0$ where $j = 1,\ldots,k$, these constraint forces are

expressible as $Q^c_{\theta_i}(t) = \sum_{j=1}^{k} \lambda_j \frac{\partial G_j}{\partial \theta_i}$, where the λ_j are time-dependent Lagrange multipliers and i runs over all segments from 1 to s.

Define an $s \times 1$ generalized constraint force vector Q^c and a $2p \times 1$ constraint force vector F^c analogous to Q and F above. Also define a $k \times 1$ constraint vector G and a $k \times 1$ Lagrange multiplier matrix Λ as $G = \begin{pmatrix} G_1 & \cdots & G_k \end{pmatrix}^T$ and $\Lambda = \begin{pmatrix} \lambda_1 & \cdots & \lambda_k \end{pmatrix}^T$, where λ_j is the Lagrange multiplier corresponding to constraint G_j. These definitions make the following matrix equations possible, where the ij^{th} element of the matrix $\frac{\partial G}{\partial \Theta}$ is $\frac{\partial G_j}{\partial \theta_i}$:

$$Q^c = AF^c \tag{6.25}$$

$$Q^c = \frac{\partial G}{\partial \Theta}\Lambda \tag{6.26}$$

Because A is a coordinate change matrix, it is nonsingular, and therefore, invertible giving Matrix Equation 6.27 for the forces of constraint.

$$F^c = A^{-1}Q^c = A^{-1}\frac{\partial G}{\partial \Theta}\Lambda \tag{6.27}$$

It is important to note that the units of these generalized force terms are Newton-meters, which means that generalized forces in the angular directions are torques. These generalized force expressions will now be incorporated into the Lagrangian equations of motion given by Equation 6.19. For simplicity, the matrices and vectors given in Table 6.1 will be used.

Table 6.1 Definition of matrices and vectors appearing in the equations of motion

Matrix / Vector	Name	Elements	Size
Θ	the *horizon angle* vector	θ_i	$s \times 1$
$\dot{\Theta}$	the *angular velocity* vector	$\dot{\theta}_i$	$s \times 1$
$\dot{\Theta}^2$	The *angular velocity-squared* vector	$\dot{\theta}_i^{\,2}$	$s \times 1$
$\ddot{\Theta}$	the *angular acceleration* vector	$\ddot{\theta}_i$	$s \times 1$
M	the *generalized mass cosine* matrix	$c_{ij} \cos(\theta_i - \theta_j)$	$s \times s$
S	the *generalized mass sine* matrix	$c_{ij} \sin(\theta_i - \theta_j)$	$s \times s$
-cosΘ Γ	the *gravity* vector	$-g\sum_{j=1}^{p} m_j r_{ji} \cos\theta_i$	$s \times 1$

When there are k constraints imposed on the system, there are $s + k$ equations of motion for the system. These equations are given in matrix form below in Equation 6.28.

$$M\ddot{\Theta} + S\dot{\Theta}^2 = -(\cos\Theta)\,\Gamma + \frac{\partial G}{\partial \Theta}\Lambda \qquad (6.28)$$
$$G = \vec{0}$$

The movement of the system during a specific phase is completely determined by a two-point boundary value problem. The BVP consists of the equations of motion given above along with specified boundary configurations $\Theta_0 = \Theta(t_0)$ and $\Theta_f = \Theta(t_f)$, which must satisfy any imposed constraints (that is, $G(\Theta_0) = G(\Theta_f) = \vec{0}$), and a time duration for the phase. The $s + k$ unknown dynamic variables in the equations of motion, which need to be solved for at each time step, are the elements of matrices Θ and Λ, namely the horizon angles and the Lagrange multipliers.

These matrix equations are converted into a system of second-order differential equations by weakening the constraint equation $G = \vec{0}$. If $G(\Theta(t)) = \vec{0}$, then differentiating twice with respect to time gives $\frac{d^2}{dt^2} G(\Theta(t)) = \vec{0}$. This second derivative must be calculated. It follows from the chain rule that $\frac{d}{dt} G(\Theta(t)) = \left(\frac{\partial G}{\partial \Theta}\right)^T \dot{\Theta}$, where $\dot{\Theta}$ is the $s \times 1$ angular velocity vector defined in Table 6.1. Taking another time derivative gives $\frac{d^2}{dt^2} G(\Theta(t)) = \mathbf{H} + \left(\frac{\partial G}{\partial \Theta}\right)^T \ddot{\Theta} = 0$. In this expression, $\mathbf{H}$ is a block matrix, where its i^{th} block is an $s \times s$ matrix given by $\mathbf{H}_i = \dot{\Theta}^T \frac{\partial^2 G_i}{\partial \Theta^2} \dot{\Theta}$ for $i = 1,\ldots,k$ and the jk^{th} component of $\frac{\partial^2 G_i}{\partial \Theta^2}$ is $\frac{\partial^2 G_i}{\partial \theta_j \partial \theta_k}$ for $j,k = 1,\ldots,s$.

Therefore, the equations of motion are given by the following system of second-order differential equations, Equation 6.29:

$$\begin{aligned} M\ddot{\Theta} - \frac{\partial G}{\partial \Theta}\Lambda &= -\left[S\dot{\Theta}^2 + (\cos\Theta)\Gamma\right] && s \text{ equations} \\ \left(\frac{\partial G}{\partial \Theta}\right)^T \ddot{\Theta} &= -\mathbf{H} && k \text{ equations} \end{aligned} \tag{6.29}$$

The above system of equations can be written more concisely. This gives the Lagrange equations of motion for a constrained system as follows:

$$\begin{bmatrix} M & \dfrac{\partial G}{\partial \Theta} \\ \left(\dfrac{\partial G}{\partial \Theta}\right)^T & 0 \end{bmatrix} \begin{bmatrix} \ddot{\Theta} \\ -\Lambda \end{bmatrix} = \begin{bmatrix} -\left[S\dot{\Theta}^2 + (\cos\Theta)\Gamma\right] \\ -\mathbf{H} \end{bmatrix} \tag{6.30}$$

Equation 6.30 is of the general form *mass* × *acceleration* = *force*. This *generalized mass* matrix is $(s+k)\times(s+k)$. If it is possible to invert this square matrix, then explicit solutions for the angular accelerations ($\ddot{\theta}_i$'s for i = 1 to s) and the Lagrange multipliers (λ_j's for j = 1 to k) at a specific time in the motion are given by Equation 6.31.

$$\begin{bmatrix} \ddot{\Theta} \\ -\Lambda \end{bmatrix} = \begin{bmatrix} M & \dfrac{\partial G}{\partial \Theta} \\ \left(\dfrac{\partial G}{\partial \Theta}\right)^T & 0 \end{bmatrix}^{-1} \begin{bmatrix} -\left[S\dot{\Theta}^2 + (\cos\Theta)\Gamma\right] \\ -\mathbf{H} \end{bmatrix} \tag{6.31}$$

There are a total of $s+k$ equations given above, the first s of which define a system of second-order, ordinary differential equations. The remaining k equations are algebraic equations for the λ's. This allows for the simultaneous computation of the k Lagrange multipliers and the angular acceleration vector $\ddot{\Theta}$ at each time step, using the values of Θ and $\dot{\Theta}$ to calculate the right-hand side of Equation 6.31. Once the Lagrange multipliers are determined, the forces of constraint may be calculated via Equation 6.27.

6.5 Constraints

The types of constraints, which are included in this model of wheelchair racing, are listed and briefly described below in Table 6.2.

Table 6.2 Constraints, which occur during wheelchair racing

Constraint	Description
Joint angle range of motion	The angle that two adjoining body segments make is limited anatomically by the joint's range of motion. The model must take these limitations into account.
Fixed hub	The wheel hub is at a fixed orientation and distance from the origin of the root segment in the model. These parameters are required model input.

In general, constraints restrict the allowable motion of a system. The constraints listed in the table confine the athlete/chair system considered in this research in specific ways. In order for constraints to be imposed and then maintained, forces must act on the

system. These are the *forces of constraint*. One advantage of the Lagrangian approach is that these forces are automatically accounted for in the equations of motion and they do not need to be specified as model input. That is, including constraint forces explicitly in the equations of motion is not necessary when the Lagrangian method is followed but is necessary when a Newtonian approach is taken (Wells 1967). In fact, it is possible to calculate the constraint forces via the transformation equations, the equations of constraint, and the Lagrange multipliers, as per Equation 6.27.

In the following sections, each constraint listed in the table is examined in detail. To include active constraints (elements of the constraint vector G) in the system's equations of motion requires the knowledge of the first partial derivatives of G, $\frac{\partial G}{\partial \Theta}$, as well as G's Hessian, $\frac{\partial^2 G}{\partial \Theta^2}$. Therefore, these derivatives will be calculated for each type of constraint.

6.5.1 Joint Angle Range of Motion

Anatomically there are restrictions in the possible range of motion of each joint. This means that it is impossible for a joint whose range of motion is $[\alpha_{min}, \alpha_{max}]$ to open smaller than α_{min} or larger than α_{max}. Figure 6.5 illustrates this constraint for a joint with range [25°,180°].

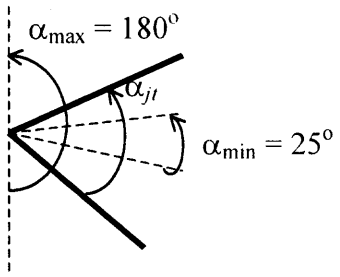

Figure 6.5 The range of motion of a joint

As was explained in Section 5.4.2, the magnitude of a model-determined joint angle is $\alpha_{jt} = 180^\circ - |\theta_{prox}| + |\theta_{dist}|$, which is acceptable provided that this value lies in the joint's range of motion. The constraint will be imposed immediately once the model outputs a configuration, which produces a joint angle that is at either extreme of the allowable range of motion. Therefore, the constraint function is either

$G(\theta_1,\ldots,\theta_n) = 180^o - |\theta_j| + |\theta_k| - \alpha_{min} = 0$ (when the angle reaches α_{min}) or

$G(\theta_1,\ldots,\theta_n) = 180^o - |\theta_j| + |\theta_k| - \alpha_{max} = 0$ (when the angle reaches α_{max}), where the joint angle being considered is between segments j (proximal) and k (distal).

In either case, the first partials are $\dfrac{\partial G}{\partial \theta_i} = \begin{cases} -1 & \text{if } i = j \\ 1 & \text{if } i = k \\ 0 & \text{if } i \neq j,k \end{cases}$, giving

$\dfrac{\partial G}{\partial \Theta} = (0 \quad -1 \quad 0 \quad \cdots \quad 0 \quad 1 \quad 0 \quad \cdots \quad 0)$, a $1 \times n$ matrix with the --1 in the j^{th} column and the +1 in the k^{th} column and $\dfrac{\partial^2 G}{\partial \Theta^2} =$ an $n \times n$ zero matrix given that there are n segments in the system.

By Equation 6.26, the components of the generalized forces of constraint are

$$Q^c_{\theta_i} = \begin{cases} -\lambda & \text{if } i = j \\ \lambda & \text{if } i = k \\ 0 & \text{if } i \neq j,k \end{cases}$$

. Since generalized forces in the angular directions were determined to be torques, this means that the constraint must be released when the induced torque changes direction.

6.5.2 Fixed Hub

The racing stroke cycle is made up of time spent in push and time spent in recovery. During recovery, the athlete's body segments and the wheel of the racing chair move independently of one another and the wheel segment need not be included in the dynamic coupled pendulum model. However, during push, their motion is coupled and the athlete must maintain contact with the pushrim of the racing chair's wheel. This necessitates the wheel's inclusion as a segment in the system during push.

As a first approximation, assume that the wrist is the body part, which stays in contact with the pushrim during push. Attaching the wheel segment to the wrist end of the forearm segment will force this condition. The system will then be modeled appropriately provided that the hub of the wheel is fixed in its correct (model input) orientation to the system's root segment and is not free to move in the plane.

To fix the hub in such a manner, first take into account that the racing wheelchair used by an athlete is custom designed so that there is a snug fit between the athlete's body and the seat. Therefore, it is assumed that the local origin of the system[1] remains at

[1] The local origin is located at the base of the trunk in a four-segment system and at the shoulder in a three-segment system.

a fixed distance from and unvarying orientation (horizon angle) to the wheel hub. These two quantities (distance D and angle θ_{hub}) are required as input to the model and are illustrated in the four-segment, point-mass / disk system of Figure 6.6 below.

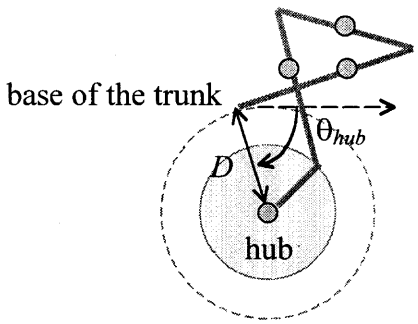

Figure 6.6 The fixed orientation of the athlete in the racing chair

Since the local origin is located at the root segment, the local coordinates of the wheel hub are $\left(D\cos\theta_{hub}, D\sin\theta_{hub}\right)$. If there are n segments in the system, these local coordinates can also be found by tracing through all n segments from the root (origin) to the end of the wheel segment. If the point-mass system's relation matrix **R** defined in Equation 6.1 of Section 6.4 is modified to become $\tilde{\mathbf{R}}$ so that its diagonal terms are now L's instead of z's, then the coordinates of the end of the wheel segment are

$\left(x_{hub}, y_{hub}\right) = \left(x_{k,end}, y_{k,end}\right) = \left(\sum_{j=1}^{n} \tilde{r}_{kj} \cos\theta_j, \sum_{j=1}^{n} \tilde{r}_{kj} \sin\theta_j\right)$, where k is given the appropriate value to indicate the wheel segment. Thus, fixing the hub results in the following system of equations of constraint:

$$\begin{cases} G_1 = D\cos\theta_{hub} - \sum_{j=1}^{n} \tilde{r}_{kj}\cos\theta_j \\ G_2 = D\sin\theta_{hub} - \sum_{j=1}^{n} \tilde{r}_{kj}\sin\theta_j \end{cases}$$

The first partials are $\frac{\partial G_1}{\partial \theta_i} = \tilde{r}_{ki}\sin\theta_i$ and $\frac{\partial G_2}{\partial \theta_i} = -\tilde{r}_{ki}\cos\theta_i$. The second partials are $\frac{\partial^2 G_1}{\partial\theta_i\partial\theta_j} = \begin{cases} \tilde{r}_{ki}\cos\theta_i & \text{for } i = j \\ 0 & \text{for } i \neq j \end{cases}$ and $\frac{\partial^2 G_2}{\partial\theta_i\partial\theta_j} = \begin{cases} \tilde{r}_{ki}\sin\theta_i & \text{for } i = j \\ 0 & \text{for } i \neq j \end{cases}$. Therefore, the

the $2 \times n$ vector $\frac{\partial G}{\partial \Theta} = \begin{bmatrix} \tilde{r}_{k1}\sin\theta_1 & \cdots & \tilde{r}_{kn}\sin\theta_n \\ -\tilde{r}_{k1}\cos\theta_1 & \cdots & -\tilde{r}_{kn}\cos\theta_n \end{bmatrix}$ and

the $2n \times n$ Hessian $\frac{\partial^2 G}{\partial \Theta^2} = \begin{bmatrix} \tilde{r}_{k1}\cos\theta_1 & & 0 \\ & \ddots & \\ 0 & & \tilde{r}_{kn}\cos\theta_n \\ \tilde{r}_{k1}\sin\theta_1 & & 0 \\ & \ddots & \\ 0 & & \tilde{r}_{kn}\sin\theta_n \end{bmatrix}$.

6.6 Non-Conservative Generalized Forces

In general, the sum of non-conservative generalized forces acting on the system make up the vector Q of Section 6.4. In MAPS, joint viscous forces are the only permitted dissipative forces (Lacker 1997, Choi 1997). However, because model output presented in this thesis agreed reasonably well with experimental data without including joint viscous forces, these parameters were set identically to zero in this work.

CHAPTER 7

THE MATHEMATICAL MODEL: OBTAINING A SOLUTION

7.1 The Two-Point Boundary Value Problem

As was previously mentioned, the entire racing stroke cycle is divided up into an arbitrary number (N) of distinct phases, $p_1, \ldots, p_N$. Each phase, p_i, is mathematically a two-point boundary value problem consisting of the following items:

- two boundary configurations Θ_0^i (initial) and Θ_f^i (final)
- a time duration, $\Delta^i t = t_f^i - t_0^i$
- the equations of motion, which include all constraints acting on the system during the phase

Because the phases will later be concatenated to form the entire stroke cycle solution, the boundary configurations of two neighboring phases must match up so that the final configuration of phase i is the same as the initial configuration of phase i+1. That is, $\Theta_f^{i-1} = \Theta_0^i$ for all i from 2 to n. This ensures the continuity of the kinematic solution throughout the stroke cycle, which is obviously desirable. Although the kinematic solution will be continuous, each phase (two-point BVP) is solved independently from the other phases. Even adjacent phases, p_{i+1} and p_{i-1}, have no effect on the solution of a given phase, p_i.

Furthermore, each phase is regarded as *ballistic*. This means that only the forces present in each phase's equations of motion (including gravitational forces, joint viscous

forces[1], and constraint forces) act on the system throughout the phase. There are no muscular forces or other external forces acting on the system for the duration of the phase, as these types of forces are not present in the equations of motion.

7.2 Method of Solution

To determine the trajectory of the segments during a phase, its two-point BVP is solved numerically by the shooting method (Press *et al.*). Assume the model includes s segments and denote the known initial configuration Θ_0 and final configuration Θ_f. The shooting method applies an iterative method to an initial value problem (IVP). In this section, a superscript will denote the current iteration step.

The IVP consists of the equations of motion along with a known duration t_f, the given initial configuration, Θ_0, and a guess as to the initial angular velocities of the segments, $\dot{\Theta}_0^0$ (required input for this method of solution). Note that the zero superscript indicates the 0^{th} guess of the initial velocity vector.

The IVP is solved, producing a trajectory $\Theta^0(t)$. Next $\Theta^0(t_f)$, the *end configuration*, is determined and $\bar{E}^0 = \left(e_1^0 \ \ldots \ e_s^0\right)$, the error between this end configuration and the desired final configuration, Θ_f, is calculated. If the error vector is zero, that is if all error vector components are less than a stipulated acceptance criteria ε, the iteration stops and $\Theta^0(t)$ is accepted as a solution to the BVP. Otherwise, the velocity vector guess is adjusted by adding $\left(\Delta\dot{\theta}_1 \ \ 0\cdots0\right)$, $\left(\ 0 \ \ \Delta\dot{\theta}_2 \ 0\cdots0\right)$, … , and $\left(\ 0\cdots0 \ \ \Delta\dot{\theta}_s\ \right)$ to

[1] Joint viscous forces are excluded in this thesis.

$\dot{\Theta}_0^0$, creating s new IVPs. Each of these is solved and corresponding end configurations are determined.

New error vectors $\vec{\mathrm{E}}_1^1 = \left(e_{11}^1 \cdots e_{1s}^1\right)$, …, $\vec{\mathrm{E}}_s^1 = \left(e_{s1}^1 \cdots e_{ss}^1\right)$ are calculated respectively. These new error vectors indicate the influence each component of the initial velocity vector has on determining the end configuration, in effect producing a measure of sensitivity. The error Jacobian matrix $\mathbf{J}^1$ has components $J_{mn}^1 = \dfrac{\partial e_{mn}^1}{\partial \dot{\theta}_n} \approx \dfrac{e_{mn}^1 - e_m^0}{\Delta \dot{\theta}_n}$. This error Jacobian matrix suggests the required amount of change in the initial velocity vector guess $\Delta^1\dot{\Theta}$, which would make the error vector zero. Once the error vector is zero, the end configuration matches the final configuration indicating a solution to the BVP. A new initial velocity vector guess is given by $\dot{\Theta}_0^1 = \dot{\Theta}_0^0 + \Delta^1\dot{\Theta}$, which in turn creates a new IVP. Iteration now occurs and continues until the error vector is zero, at which point a solution to the BVP is found.

7.3 Interpretation of the Solution

The solutions of all N phases are concatenated to form the entire stroke cycle. Although the *configurations* are required to match at the boundaries of the phases, the angular *velocities* have no such restriction. Moreover, because the phases are solved independently, these velocities are likely to be discontinuous at the phase boundaries. Denote the discontinuity in segment angular velocities between phases i-1 and i as $\Delta^{i-1,i}\vec{v} = \vec{v}_i - \vec{v}_{i-1}$ for $i = 2$ to n. Then at each phase boundary there is an instantaneous change in angular velocity $\Delta^{i-1,i}\vec{v}$, which is interpretable as an immediate change in the system's generalized momentum. Impulsive generalized forces cause these instantaneous

changes in generalized momentum. Thus, these impulsive generalized forces may be calculated from the discontinuities in the segments' angular velocities at the phase boundaries, which are model output.

Moreover, these impulsive generalized forces have two sources of origin. One source is instantaneous muscle input from the athlete. The second source is physical impulsive generalized forces acting on the system at that instant. In the wheelchair racing stroke there are two occurrences which can produce physical impulsive generalized forces. One physical impulsive generalized force is the impact force caused by the full extension or flexion of a joint. The other is the impact force caused by the athlete's inelastic collision with the pushrim at the moment of push. Because these instantaneous physical generalized forces arise from impacts, they will be referred to as *impact forces*.

It is certainly possible that the total impulsive generalized forces calculated at *some* phase boundaries have components of instantaneous muscle input *and* instantaneous impact forces. It is desirable to separate these forces so that the athlete's muscular input is known. In order to resolve this net muscle input, these non-muscular impact forces must be subtracted out of the calculated total impulsive generalized force at the phase boundary. Therefore, these instantaneous impact forces need to be determined. This is accomplished by the *projection method*, which is explained in Sections 7.4 and 8.4. It is important to note that required muscle input at a phase boundary may be positive, a source of energy, or negative, a sink of energy. If muscle input is positive, the muscles must supply energy to the system by acting propulsively. On the other hand, if muscle input is negative, the muscles must remove energy from the system by braking.

As was already stated, the number of phases chosen is arbitrary. Because muscle input is only possible at the phase boundaries, increasing the number of phases allows for more frequent muscular action, and in the limit, approaches continuous muscle activity. In fact, using N phases in the model to simulate a VICON-recorded racing stroke technique, which consists of F frames of kinematic data, results in a Lagrangian form of the inverse method in the limit as N approaches F.

However, it is plausible that an energetically efficient stroke does not require frequent (or continuous) muscle input. This means that a small number of phases may be adequate for the purpose of this research, which seeks a mechanically energy efficient stroke technique. In fact, in the *ideal* case perhaps the net muscle input required is zero. That is, the net effect of the gravitational forces, joint viscous forces, constraint forces, and impact forces acting on the system cause the segments to complete a racing stroke without any muscle input at all. This would clearly define a mechanically efficient stroke technique for the athlete. If such an ideal solution exists, it would certainly be extremely sensitive to such parameters as push timing and the point of force application. Even if an ideal solution does not exist, the model is still useful provided that the wheelchair racing stroke can be idealized into prominent times when the muscles are active (that is, phase boundaries).

7.4 The Projection Method

The projection method is used to predict the magnitude of the impulsive, non-muscular impact forces. The two circumstances for which the projection method must be employed in modeling wheelchair racing are those described in Section 6.5, namely at

joint angle extremes and at pushrim contact. First consider pushrim contact. When the (n-1)-coupled body segment pendulum system hits the pushrim of the wheel, the segments' trajectories, and thus velocities, are instantly redirected so that the constraint (the circular path of the pushrim) is followed. Essentially what occurs is that the velocities of the segments are projected into the tangent space of the constraint. Similarly, when a joint angle is at its extreme range of motion, the joint's segments must instantaneously alter their trajectories to avoid hyperextension or hyperflexion. Details of the projection theorem and the calculations involved are given in Section 8.4.

CHAPTER 8

A GEOMETRIC DERIVATION OF THE EQUATIONS OF MOTION

8.1 Introduction and Definitions

In this section, a non-rigorous, general derivation of the model's equations of motion will be presented. The calculus of variations is employed through a geometric approach. Equations for both the unconstrained and constrained cases, as well as the projection method, will be obtained.

Although many of the notations used in this section will be the same as those in Chapter 6, some new definitions are necessary. A *path*, $\Theta(t) = \left(\theta_1(t) \quad \cdots \quad \theta_n(t)\right)^T$, is the varying configuration of a conservative, mechanical system as t changes. That is, $\Theta(t)$ is a possible motion of a conservative mechanical system. Paths that are continuous and non-singular in the time interval $[t_0, t_f]$, which also have continuous first and second derivatives for this duration, will be considered. The *action of a given path*, $A[\Theta(t)]$, is defined to be the path-dependent functional $A[\Theta(t)] = \int_{t_0}^{t_f} \mathsf{L}\left(\Theta(t), \dot{\Theta}(t), t\right) dt$, where $\Theta_0 = \Theta(t_0)$ and $\Theta_f = \Theta(t_f)$ are given boundary configurations and L is the *Lagrangian* of the path. Specifically, L is defined as the system's kinetic energy minus its potential energy along $\Theta(t)$, the given possible path. The *critical path* of the system, denoted $\Theta^*(t)$, is the curve for which the action has a stationary value. (A stationary value occurs when the variation of the action is zero.) According to Hamilton's Principle of

Least Action, any observed path of the conservative mechanical system that satisfies the given boundary configurations must be a critical path of the action A.

8.2 The Unconstrained Conservative System

First, consider when the system is unconstrained. Perturb $\Theta(t)$, any given path of the system, to produce neighboring paths, which are still required to have the same boundary configurations. This is done by choosing a small scalar, ε, and any *test function* $\eta(t) = (\eta_1(t) \quad \cdots \quad \eta_n(t))^T$, which is in the set S. S consists of all $n \times 1$, time-dependent test functions that are continuous and nonsingular between t_0 and t_f with continuous first and second derivatives in the same interval and which vanish at both t_0 and t_f. The neighboring paths are then $\Theta(t,\varepsilon) = \Theta(t) + \varepsilon\eta(t)$. Note that in the limit, as $\varepsilon \to 0$, the neighboring paths approach the given path and that $\Theta(t,0) = \Theta(t)$. The variation of the action of the given path $\Theta(t)$ is calculated below where $\Phi(\varepsilon) = A[\Theta(t,\varepsilon)]$ to give Equation 8.1:

$$\delta A[\Theta(t)] = \left.\frac{d\Phi}{d\varepsilon}\right|_{\varepsilon=0} = \left.\left(\frac{d}{d\varepsilon}\int_{t_0}^{t_f} \mathcal{L}\left(\Theta(t,\varepsilon),\dot{\Theta}(t,\varepsilon),t\right)dt\right)\right|_{\varepsilon=0}$$

$$= \left.\left(\int_{t_0}^{t_f}\left(\frac{\partial \mathcal{L}\left(\Theta(t,\varepsilon),\dot{\Theta}(t,\varepsilon),t\right)}{\partial\Theta}\cdot\frac{\partial\Theta(t,\varepsilon)}{\partial\varepsilon} + \frac{\partial \mathcal{L}\left(\Theta(t,\varepsilon),\dot{\Theta}(t,\varepsilon),t\right)}{\partial\dot{\Theta}}\cdot\frac{\partial\dot{\Theta}(t,\varepsilon)}{\partial\varepsilon}\right)dt\right)\right|_{\varepsilon=0}$$

$$= \left.\left(\int_{t_0}^{t_f}\frac{\partial \mathcal{L}\left(\Theta(t,\varepsilon),\dot{\Theta}(t,\varepsilon),t\right)}{\partial\Theta}\cdot\frac{\partial\Theta(t,\varepsilon)}{\partial\varepsilon}dt\right)\right|_{\varepsilon=0} + \left.\left(\int_{t_0}^{t_f}\frac{\partial \mathcal{L}\left(\Theta(t,\varepsilon),\dot{\Theta}(t,\varepsilon),t\right)}{\partial\dot{\Theta}}\cdot\frac{\partial\dot{\Theta}(t,\varepsilon)}{\partial\varepsilon}dt\right)\right|_{\varepsilon=0} \tag{8.1}$$

where the i^{th} elements of the vectors $\frac{\partial \mathcal{L}}{\partial\Theta}$, $\frac{\partial \mathcal{L}}{\partial\dot{\Theta}}$, $\frac{\partial\Theta}{\partial\varepsilon}$, and $\frac{\partial\dot{\Theta}}{\partial\varepsilon}$ are

$\frac{\partial \mathcal{L}}{\partial\theta_i}$, $\frac{\partial \mathcal{L}}{\partial\dot{\theta}_i}$, $\frac{\partial\theta_i}{\partial\varepsilon}$, and $\frac{\partial\dot{\theta}_i}{\partial\varepsilon}$, respectively.

The second integral in Equation 8.1 is simplified via integration by parts as follows:

$$\int_{t_0}^{t_f} \frac{\partial \mathcal{L}\left(\Theta(t,\varepsilon),\dot{\Theta}(t,\varepsilon),t\right)}{\partial \dot{\Theta}} \cdot \frac{\partial \dot{\Theta}(t,\varepsilon)}{\partial \varepsilon}\, dt$$

$$= \int_{t_0}^{t_f} \frac{\partial \mathcal{L}\left((t,\varepsilon),\dot{\Theta}(t,\varepsilon),t\right)}{\partial \dot{\Theta}} \cdot \frac{\partial}{\partial t}\left(\frac{\partial \Theta(t,\varepsilon)}{\partial \varepsilon}\right) dt$$

$$= \frac{\partial \mathcal{L}\left(\Theta(t,\varepsilon),\dot{\Theta}(t,\varepsilon),t\right)}{\partial \dot{\Theta}} \cdot \frac{\partial \Theta(t,\varepsilon)}{\partial \varepsilon}\Big|_{t_0}^{t_f} - \int_{t_0}^{t_f} \frac{d}{dt}\left(\frac{\partial \mathcal{L}\left(\Theta(t,\varepsilon),\dot{\Theta}(t,\varepsilon),t\right)}{\partial \dot{\Theta}}\right) \cdot \frac{\partial \Theta(t,\varepsilon)}{\partial \varepsilon}\, dt$$

Since $\frac{\partial \Theta(t,\varepsilon)}{\partial \varepsilon} = \eta(t)$ and $\eta(t)$ vanishes at t_0 and t_f, the first term of the result above is zero. Substituting the remaining term into Equation 8.1 and letting $\varepsilon = 0$ gives the variation of the action of the given path $\Theta(t)$ to be the linear functional $\delta A[\Theta(t)] = \int_{t_0}^{t_f} \left[\frac{\partial \mathcal{L}\left(\Theta(t),\dot{\Theta}(t),t\right)}{\partial \Theta} - \frac{d}{dt}\left(\frac{\partial \mathcal{L}\left(\Theta(t),\dot{\Theta}(t),t\right)}{\partial \dot{\Theta}}\right)\right] \cdot \eta(t)\, dt$, where $\eta(t)$ is any element of S. To state this concisely, define the Eulerian grad operator, $\tilde{\nabla} = \frac{\partial}{\partial \Theta} - \frac{d}{dt}\frac{\partial}{\partial \dot{\Theta}}$, and the inner product $\langle \vec{a}, \vec{b} \rangle = \int_{t_0}^{t_f} \vec{a} \cdot \vec{b}\, dt$. Thus, $\delta A[\Theta(t)] = \left\langle \tilde{\nabla} \mathcal{L}\left(\Theta(t),\dot{\Theta}(t),t\right), \eta(t) \right\rangle$. Furthermore, a critical path, $\Theta^*(t) = \Theta(t)$, exists when $\langle \tilde{\nabla} \mathcal{L}, \eta \rangle = 0$ for all $\eta \in S$ since a critical path with respect to A occurs when $\delta A = 0$. Geometrically, this is implies that for the critical path $\tilde{\nabla} \mathcal{L}$ is orthogonal to all $\eta \in S$ for the given mechanical system.

The fundamental lemma of the calculus of variations states that if $\langle M(t),\eta(t)\rangle = 0$ for all arbitrary functions $\eta(t)$ continuous through the second derivative, then $M(t)$ must vanish in the interval (t_0, t_f) (Goldstein 1980). Applying the fundamental lemma to the inner product found above which holds for all test functions $\eta \in S$ allows for the conclusion that the $n \times 1$ vector $\tilde{\nabla}L$ must be identically zero for $\Theta(t) = \Theta^*(t)$.

This gives *the Lagrangian equations of the observed motion for unconstrained conservative systems*, Equation 8.2, below.

$$\tilde{\nabla}L = \vec{0}$$

or (8.2)

component-wise $\frac{d}{dt}\left(\frac{\partial L}{\partial \dot{\theta}_i}\right) - \frac{\partial L}{\partial \theta_i} = 0$ for $i = 1$ to n

8.3 The Constrained Conservative System

Next, consider a system with k independent constraints where the $k \times 1$-constraint vector, $G(\Theta(t))$, is given by $G(\Theta(t)) = \left(G_1[\Theta(t)] \quad \cdots \quad G_k[\Theta(t)]\right)^T = \vec{0}$. Denote the time at which the constraints are imposed as t_c so that the constraints act on the system for $t_c \le t \le t_f$. Assume that $G = \vec{0}$ for $t_c \le t \le t_f$ defines a smooth (n-k)-dimensional surface (manifold) of constraint C, which has a well-defined tangent space at each point on it. This means that the columns of ∇G are independent; that is, ∇G is a full k-rank matrix. The following analysis will only consider the post-constraint system (that is, when $t \in [t_c, t_f]$) since the pre-constraint (unconstrained) system was analyzed earlier.

In this case, the critical path must lie on the surface of constraint, C. A path $\Theta(t)$ on the surface of constraint C given by $G(\Theta(t)) = \bar{0}$ is critical, $\Theta(t) = \Theta^*(t)$, for the action A restricted to G, denoted A/G, if $\delta\left(A/G[\Theta(t)]\right) = 0$ with respect to *all* neighboring paths $\Theta(t,\varepsilon)$ on C.

Creating a parametrized set of all paths $\Theta(t,\varepsilon)$ on C near a given path $\Theta(t)$ on C now requires that the test functions $\eta(t)$ be chosen from a subset of S such that all paths $\Theta(t,\varepsilon)$ remain on the constraint surface C defined by $G(\Theta(t)) = \bar{0}$. This restricted set of test functions, $\eta(t)$, will be denoted by S/G and will be more precisely described below.

Let $\Theta(t,\varepsilon) = \Theta(t) + \varepsilon\eta(t,\varepsilon)$ such that $G(\Theta(t,\varepsilon)) = \bar{0}$. Note that η must also now depend on the parameter ε and that when $\varepsilon = 0$, $\Theta(t,0) = \Theta(t)$. Assume that $\frac{\partial\eta}{\partial\varepsilon}$ exists in some open interval about $\varepsilon = 0$.

Define a $k \times 1$ functional vector $\boldsymbol{G}[\Theta(t,\varepsilon)] = \left(G_1[\Theta(t,\varepsilon)] \quad \cdots \quad G_k[\Theta(t,\varepsilon)]\right)^T$, which consists of functionals $\boldsymbol{G}_i$ defined as $\boldsymbol{G}_i[\Theta(t,\varepsilon)] = \int_{t_c}^{t_f} G_i[\Theta(t,\varepsilon)]dt$. Since all neighboring paths are on the surface, they must satisfy all constraints, giving $G_i[\Theta(t,\varepsilon)] = 0$ for $i = 1$ to k. This in turn gives $\boldsymbol{G}_i[\Theta(t,\varepsilon)] = 0$ for $i = 1$ to k, so that $\boldsymbol{G} = \bar{0}$. Furthermore, $\delta\boldsymbol{G}_i = 0$ for $i = 1,\ldots,k$ or $\delta\boldsymbol{G} = 0$ for all $\Theta(t)$ on C since all paths in the neighborhood of $\Theta(t)$ are also restricted to be on C; that is, $G(\Theta(t,\varepsilon)) = \bar{0}$.

The variation of $\boldsymbol{G}$'s components, $\boldsymbol{G}_i[\Theta(t)]$, at $\Theta(t)$ are specifically calculated as follows:

$$0 = \delta G_i = \left(\frac{d}{d\varepsilon} \int_{t_c}^{t_f} G_i(\Theta(t,\varepsilon))dt \right)\Bigg|_{\varepsilon=0} = \left(\int_{t_c}^{t_f} \frac{dG_i(\Theta(t,\varepsilon))}{d\Theta} \cdot \frac{d\Theta(t,\varepsilon)}{d\varepsilon} dt \right)\Bigg|_{\varepsilon=0}$$

$$= \left(\int_{t_c}^{t_f} \frac{dG_i(\Theta(t,\varepsilon))}{d\Theta} \cdot \left[\eta(t,\varepsilon) + \varepsilon \frac{\partial \eta(t,\varepsilon)}{\partial \varepsilon} \right] dt \right)\Bigg|_{\varepsilon=0} = \int_{t_c}^{t_f} \frac{dG_i(\Theta(t))}{d\Theta} \cdot \eta(t,0) dt$$

Therefore, the subset S/G of test functions $\eta_0(t)$ associated with the surface path $\Theta(t)$ must satisfy $\langle \nabla G_i(\Theta(t)), \eta_0(t) \rangle = 0$ where $\nabla G_i(\Theta(t)) = \frac{dG_i(\Theta(t))}{d\Theta}$, $\eta_0(t) = \eta(t,0)$, and the inner product definition is modified to integrate from t_c to t_f. Moreover, since this inner product equation must hold for all constraints (i.e., for $i = 1,\ldots,k$), the test functions consistent with all constraints, $\eta_0(t)$, must satisfy the homogeneous system given in Equation 8.3 where the ij^{th} element of the matrix $(\nabla G)^{\mathrm{T}}$ is $\frac{dG_i(\Theta(t))}{d\theta_j}$.

$$\left(\nabla G(\Theta(t))\right)^T \eta_0(t) = \vec{0} \tag{8.3}$$

Therefore, η_0, the nullspace of $(\nabla G)^T$, is the tangent space of the constraint surface C at the point $\Theta(t)$ at a given time t. In other words, the rowspace of $(\nabla G)^T$ is the orthogonal complement of the tangent space of the surface of constraint C.

In order for $\Theta^*(t) = \Theta(t,0)$ to be critical with respect to the action, it must be stationary with respect to all neighboring paths on C. Denote the action of the path

restricted to remain on the constraint surface by $\mathcal{A}_G[\Theta(t)]$. Then

$\mathcal{A}_G[\Theta(t)] = \int_{t_c}^{t_f} L(\Theta(t),\dot{\Theta}(t),t)dt$, where $\Theta(t)$ must be a path on the surface C (i.e., $G(\Theta(t)) = \vec{0}$). The variance of the action of a constraint-surface path is calculated below where $\Phi_G(\varepsilon) = \mathcal{A}_G[\Theta(t,\varepsilon)]$.

$$\delta\left(\mathcal{A}_G[\Theta(t)]\right) = \left.\frac{d\Phi_G(\varepsilon)}{d\varepsilon}\right|_{\varepsilon=0} = \left.\left(\frac{d}{d\varepsilon}\int_{t_c}^{t_f} \mathcal{L}\left(\Theta(t)+\varepsilon\eta(t,\varepsilon),\dot{\Theta}(t)+\varepsilon\frac{\partial\eta(t,\varepsilon)}{\partial t},t\right)dt\right)\right|_{\varepsilon=0}$$

via Equation 8.1 (8.4)

$$= \left.\left(\int_{t_c}^{t_f}\left\{\frac{\partial\mathcal{L}\left(\Theta(t,\varepsilon),\dot{\Theta}(t,\varepsilon),t\right)}{\partial\Theta}\cdot\left(\eta(t,\varepsilon)+\varepsilon\frac{\partial\eta(t,\varepsilon)}{\partial\varepsilon}\right)\right.\right.\right.$$
$$\left.\left.\left.+\frac{\partial\mathcal{L}\left(\Theta(t,\varepsilon),\dot{\Theta}(t,\varepsilon),t\right)}{\partial\dot{\Theta}}\cdot\left[\frac{\partial\eta(t,\varepsilon)}{\partial t}+\varepsilon\frac{d}{dt}\left(\frac{\partial\eta(t,\varepsilon)}{\partial\varepsilon}\right)\right]\right\}\right)\right|_{\varepsilon=0}$$

Integrate the second term in Equation 8.4 by parts, let $\varepsilon = 0$, and recall that test functions vanish at the endpoints. This allows the variation of the action of a constraint-surface path to be expressed as follows, where the inner product is modified to integrate from t_c to t_f:

$$\delta\left(\mathcal{A}_G[\Theta(t)]\right) = \left\langle\tilde{\nabla}\mathcal{L}\left(\Theta(t),\dot{\Theta}(t),t\right),\eta_0(t)\right\rangle \tag{8.5}$$

Therefore, a constraint-surface path is critical and $\Theta^*(t) = \Theta(t)$ when Equation 8.6 holds for all $\eta_0 \in S/G$.

$$\left\langle \tilde{\nabla} L \, , \eta_0 \right\rangle = 0 \tag{8.6}$$

Since Equation 8.3 defines η_0 to be *any* vector in the tangent space of C at $\Theta^*(t)$, it follows from Equation 8.6 that $\tilde{\nabla} L \left(\Theta^*(t), \dot{\Theta}^*(t), t\right)$ must be orthogonal to the tangent space of C at $\Theta^*(t)$. This means that for a critical constraint-surface path $\Theta^*(t)$, $\tilde{\nabla} L$ must lie in the subspace orthogonal to the surface of constraint, namely the column space of ∇G. Therefore, $\tilde{\nabla} L = \sum_{i=1}^{k} (\nabla G_i)\lambda_i = (\nabla G)\Lambda$, where the $k \times 1$-vector $\Lambda(t) = \left(\lambda_1(t) \quad \cdots \quad \lambda_k(t)\right)^T$ is time-dependent (since ∇G varies with time).

This gives *the Lagrangian equations of observed motion for constrained conservative systems*, Equation 8.7, below.

$$\tilde{\nabla} L = (\nabla G)\Lambda$$

or (8.7)

component-wise $\dfrac{d}{dt}\left(\dfrac{\partial L}{\partial \dot{\theta}_i}\right) - \dfrac{\partial L}{\partial \theta_i} = \sum_{j=1}^{k} (\nabla G_j)\lambda_j$ for $i = 1$ to n

8.4 The Constraint Interface and the Projection Theorem

Equations 8.2 and 8.7 allow for the determination of the equations of observed motion for an unconstrained conservative system or a constrained conservative system. Now consider the moment, t_c, when a constraint is imposed on an unconstrained (*pre-constraint*) system causing it to become constrained (*post-constraint*).

Let the neighborhood of the critical path be defined piecewise as

$\Theta^*(t,\varepsilon) = \Theta^*(t) + \varepsilon\eta$, where $\eta = \begin{cases} \eta^-(t) & \text{for } t \in [t_0, t_c] \\ \eta^+(t,\varepsilon) & \text{for } t \in [t_c, t_f] \end{cases}$. That is, the neighboring paths of the unconstrained and constrained critical paths can be represented as $\Theta^{*-}(t,\varepsilon) = \Theta^*(t) + \varepsilon\eta^-(t)$ and $\Theta^{*+}(t,\varepsilon) = \Theta^*(t) + \varepsilon\eta^+(t,\varepsilon)$, respectively. Note that the boundary conditions $\eta^-(t_0) = \eta^+(t_f,\varepsilon) = \bar{0}$ must still hold and the constraint $G(\Theta^{*+}(t,\varepsilon)) = \bar{0}$ for $t_c \le t \le t_f$ must now additionally be satisfied so that the neighboring paths will remain on the surface of constraint for the appropriate time interval.

The action of the critical path $\Theta^*(t)$ is obtained by summing the actions of the unconstrained critical path and of the constrained critical path. That is, $A[\Theta^*(t)] = A[\Theta^{*-}(t,\varepsilon)] + A[\Theta^{*+}(t,\varepsilon)]$, where each action is computed over the appropriate time interval.

Setting the variation of the action of this critical path equal to zero via Equation 8.1 gives Equation 8.8 where $\eta_0^+(t) = \eta^+(t,0)$ as before:

$$\int_{t_0}^{t_c} \tilde{\nabla} L\left(\Theta^*(t),\dot{\Theta}^*(t),t\right)\cdot\eta^-(t)dt + \frac{\partial L\left(\Theta^*(t),\dot{\Theta}^*(t),t\right)}{\partial\dot{\Theta}}\cdot\eta^-(t)\Big|_{t_0}^{t_c}$$
$$+\int_{t_c}^{t_f} \tilde{\nabla} L\left(\Theta^*(t),\dot{\Theta}^*(t),t\right)\cdot\eta_0^+(t)dt + \frac{\partial L\left(\Theta^*(t),\dot{\Theta}^*(t),t\right)}{\partial\dot{\Theta}}\cdot\eta_0^+(t)\Big|_{t_c}^{t_f} = 0 \qquad (8.8)$$

The boundary conditions allow for simplification, giving Equation 8.9, which describes the variation of the action of the critical path:

$$\int_{t_0}^{t_c} \tilde{\nabla} L\left(\Theta^*(t),\dot{\Theta}^*(t),t\right)\cdot\eta^-(t)dt + \int_{t_c}^{t_f} \tilde{\nabla} L\left(\Theta^*(t),\dot{\Theta}^*(t),t\right)\cdot\eta_0^+(t)dt$$
$$+\frac{\partial L\left(\Theta^*(t),\dot{\Theta}^*(t),t\right)}{\partial\dot{\Theta}}\cdot\eta^-(t)\Big|_{t_c} + \frac{\partial L\left(\Theta^*(t),\dot{\Theta}^*(t),t\right)}{\partial\dot{\Theta}}\cdot\eta_0^+(t)\Big|_{t_c} = 0 \qquad (8.9)$$

Consider the following cases:

Case 1: The path contacts the surface of constraint C at time t_c and has the same configuration as the critical path at that instant.

1a) Perturb the pre-constraint path, but contact C at Θ_{con} at time t_c where $\Theta_{con}(t_c) = \Theta^*(t_c)$, the contact configuration of the critical path, and then follow the critical path (post-constraint) on C. Mathematically, this means

$$\Theta(t) = \begin{cases} \Theta^{*-}(t,\varepsilon) & \text{for } t_0 \le t < t_c \\ \Theta^*(t) & \text{for } t_c \le t \le t_f \end{cases} \text{ with } \eta^-(t_0) = \vec{0},\ \eta^-(t_c) = \vec{0}, \text{ and}$$

$\eta^+(t,\varepsilon) = \vec{0}$ for $t_c \le t \le t_f$. This case is illustrated below.

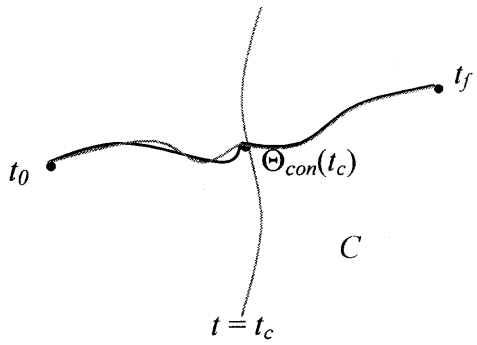

NOTE: The path followed is black and the critical path is gray.

Equation 8.9 reduces to $\int_{t_0}^{t_c} \tilde{\nabla} L\left(\Theta^*(t), \dot{\Theta}^*(t), t\right) \cdot \eta^-(t) dt = 0$ (pre-constraint) for all $\eta^- \in S$. This means that a necessary condition for a path to be critical for $t_0 \le t \le t_c$ is $\tilde{\nabla} L = \vec{0}$. Therefore, the system's motion in this time interval must satisfy $\tilde{\nabla} L = \vec{0}$.

1b) Follow the critical path from $t = t_0$ until $t = t_c$ so that Θ_{con} is the contact configuration on C as before, but then perturb the path on the surface C. Mathematically, this means $\Theta(t) = \begin{cases} \Theta^*(t) & \text{for } t_0 \le t \le t_c \\ \Theta^{*+}(t, \varepsilon) & \text{for } t_c < t \le t_f \end{cases}$ with $\eta^+(t_c, \varepsilon) = \vec{0}$, $\eta^+(t_f, \varepsilon) = \vec{0}$, and $\eta^-(t) = \vec{0}$ for $t_0 \le t \le t_c$. This case is illustrated below.

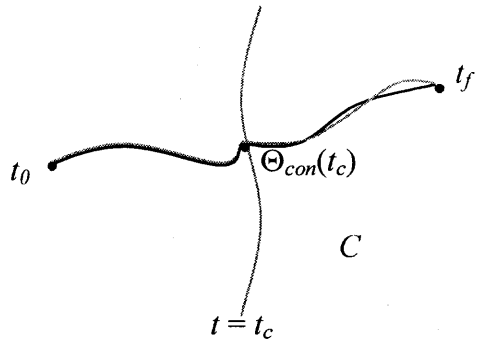

NOTE: The path followed is black and the critical path is gray.

Equation 8.9 reduces to $\int_{t_c}^{t_f} \tilde{\nabla} L\left(\Theta^*(t), \dot{\Theta}^*(t), t\right) \cdot \eta_0^+(t) dt = 0$ (post-constraint) for all $\eta_0^+ \in S/G$. Since the system is constrained, this means that a necessary condition for a path to be critical for $t_c \le t \le t_f$ is $\tilde{\nabla} L = (\nabla G)\Lambda$. Therefore, the system's motion in this time interval must satisfy $\tilde{\nabla} L = (\nabla G)\Lambda$.

1c) Combine cases 1a and 1b to account for any paths which still contact C at Θ_{con} at time t_c, but are perturbed in both of the time intervals $[t_0, t_c)$ (pre-constraint) and $(t_c, t_f]$ (post-constraint). That is,

$$\Theta(t) = \begin{cases} \Theta^{*-}(t,\varepsilon) & \text{for } t_0 \le t < t_c \\ \Theta_{con} & \text{for } t = t_c \\ \Theta^{*+}(t,\varepsilon) & \text{for } t_c < t \le t_f \end{cases} \quad \text{with } \eta^-(t_0) = \eta^-(t_c) = \vec{0} \text{ and}$$

$\eta^+(t_c,\varepsilon) = \eta^+(t_f,\varepsilon) = \vec{0}$. This case is illustrated below.

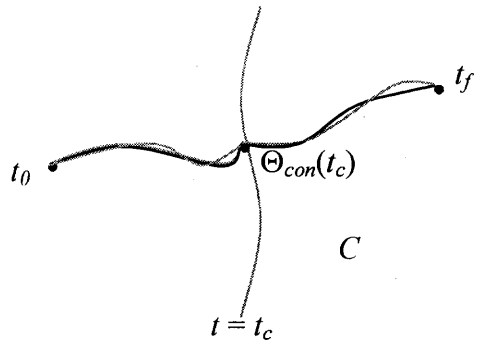

NOTE: The path followed is black and the critical path is gray.

In this combined case, the system's motion must satisfy $\tilde{\nabla}L = 0$ for $t_0 \le t < t_c$ (pre-constraint) and $\tilde{\nabla}L = (\nabla G)\Lambda$ for $t_c < t \le t_f$ (post-constraint). Note that because case 1c combined cases 1a and 1b, no new necessary conditions were established.

This concludes Case 1.

Case 2: The path contacts the surface of constraint C at time t_c and does not have the same configuration as the critical path at that instant.

Perturb the path in both the pre-constraint and the post-constraint regions (for $t \in [t_0, t_c) \cup (t_c, t_f]$), but allow the path to contact C at time t_c in a configuration different than $\Theta_{con} = \Theta^*(t_c)$ (the contact configuration of the critical path). That is, choose $\Theta(t) = \begin{cases} \Theta^{*-}(t,\varepsilon) & \text{for } t_0 \le t \le t_c \\ \Theta^{*+}(t,\varepsilon) & \text{for } t_c \le t \le t_f \end{cases}$ with $\eta^-(t_0) = \vec{0}$ and

$\eta^+(t_f,\varepsilon)=\bar{0}$ to satisfy the boundary conditions of the system and $\eta^-(t_c)=\eta^+(t_c,\varepsilon)\neq\bar{0}$ to satisfy continuity at the constraint interface and so that the contact point is not Θ_{con}.

Recall that $\Theta^{*-}(t,\varepsilon)$ is the part of the path not on the surface of constraint and that $\Theta^{*+}(t,\varepsilon)$ is the part of the path on the surface of constraint. Also note that since the path (and not the velocity) must be continuous at the constraint interface, $\eta^-(t_c)=\eta^+(t_c,\varepsilon)$. This case is illustrated below.

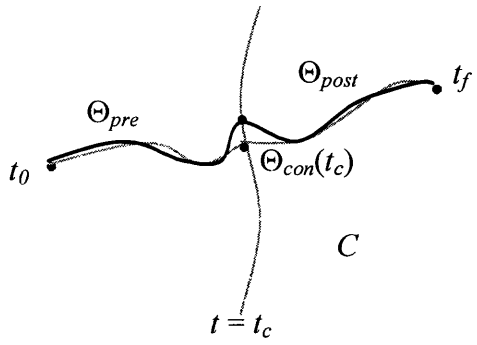

NOTE: The path followed is black and the critical path is gray.

In this case, Equation 8.9 becomes

$\int_{t_0}^{t_c}\tilde{\nabla}L\cdot\eta^-dt+\int_{t_c}^{t_f}\tilde{\nabla}L\cdot\eta_0^+dt+\frac{\partial L}{\partial\dot{\Theta}}\cdot\eta^-\Big|_{t_c}-\frac{\partial L}{\partial\dot{\Theta}}\cdot\eta_0^+\Big|_{t_c}=0$. By cases 1a and 1b, the first and second integrals are identically zeroes, respectively. Furthermore, since $\eta^-(t)=\eta^+(t,\varepsilon)$ at t_c, this simplifies to give Equation 8.10 below.

$$\left\{\frac{\partial L\left(\Theta^{*-}(t),\dot{\Theta}^{*-}(t),t\right)}{\partial\dot{\Theta}}-\frac{\partial L\left(\Theta^{*+}(t),\dot{\Theta}^{*+}(t),t\right)}{\partial\dot{\Theta}}\right\}\Bigg|_{t_c}\cdot\eta_0^+(t_c)=0 \qquad (8.10)$$

Consider the quantity enclosed in braces in Equation 8.10. Recall that the Lagrangian is defined in matrix form as

$\mathsf{L}\left(\Theta(t),\dot{\Theta}(t),t\right) =$ kinetic energy - potential energy $= \frac{1}{2}\dot{\Theta}^T M\dot{\Theta} - V_{sys}(\Theta)$, where M is the Θ-dependent generalized mass cosine matrix defined in Section 6.4.

Therefore, $\frac{\partial \mathsf{L}}{\partial \dot{\Theta}} = M\dot{\Theta}$, which can be substituted into Equation 8.10 to give Equation 8.11 below.

$$\left(\left(M\dot{\Theta}^{*-} - M\dot{\Theta}^{*+}\right)\Big|_{t_c}\right)^T \eta_0^+(t_c) = 0 \qquad (8.11)$$

Factoring out the symmetric generalized mass cosine matrix in Equation 8.11 gives Equation 8.12.

$$\left(\dot{\Theta}^{*-}(t_c) - \dot{\Theta}^{*+}(t_c)\right)^T M|_{t_c}\, \eta_0^+(t_c) = 0 \qquad (8.12)$$

Given M, a positive-definite symmetric matrix, a new inner product with respect to M is defined as $\langle \vec{a},\vec{b}\rangle_M = \vec{a}^T M \vec{b}$. With this M-inner product, Equation 8.12 is now expressible as follows where all quantities in the equation are evaluated at *contact*, the instant when the system becomes constrained (i.e., at time t_c):

$$\left\langle \dot{\Theta}^{*-} - \dot{\Theta}^{*+}, \eta_0^+ \right\rangle_M = 0 \qquad \text{at } t_c \tag{8.13}$$

From Equation 8.13 it follows that $\dot{\Theta}^{*-} - \dot{\Theta}^{*+}$ is M-orthogonal to all η_0^+ in S/G at contact. Since it was defined previously that η_0^+ is *any* element in the tangent space to the surface of constraint C at any given point, it further follows that $\dot{\Theta}^{*-} - \dot{\Theta}^{*+}$ must be M-orthogonal to all η_0^+, that is to the tangent space at the specified point. In addition, $\dot{\Theta}^{*+}$ must be in T, the tangent space to C at contact, for $t_c \le t \le t_f$ so that the post-constraint path will remain on the surface of constraint during this time interval. Figure 8.1 below illustrates the geometric relationship between the pre- and post-constraint generalized velocities at contact, where pictorial orthogonality indicates M-orthogonality.

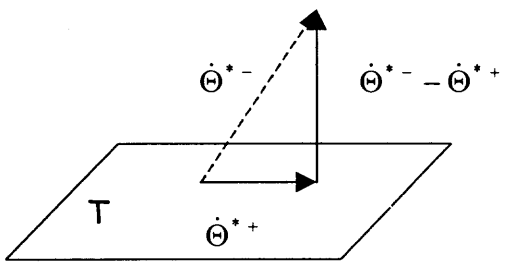

Figure 8.1 An illustration of the relationship between pre- and post-constraint generalized velocities at contact

As can be seen in Figure 8.1, note that just before contact, the pre-constraint generalized velocity vector $\dot{\Theta}^{*-}(t_c)$ is not generally in the tangent

space of the surface of constraint C (of which the system is not yet aware). However, instantaneously after contact, the post-constraint generalized velocity vector $\dot{\Theta}^{*+}(t_c)$ must be in the tangent space of C to ensure that the path $\Theta^{*+}(t,\varepsilon)$ will remain on C for $t \in [t_c, t_f]$, as required by the post-constraint system. This instantaneous jump accounts for the discontinuity of velocities and requires the presence of impulsive forces at the time of contact. Physically, this contact often corresponds to an inelastic collision and the impulsive forces are the collision impact forces. Furthermore, it can be seen from Figure 8.1 that $\dot{\Theta}^{*+}$ is geometrically the M-projection of $\dot{\Theta}^{*-}$ into T at contact.

To actually calculate $\dot{\Theta}^{*+}(t_c)$, the M-projected generalized velocity vector at contact, it is necessary to have an explicit representation of T. Such a representation is possible since T is the homogeneous solution of $\nabla G\left(\Theta^*(t_c)\right)^T \eta_0^+(t_c) = \vec{0}$. Since the k constraints of G are independent, T is the (n-k)-dimensional nullspace of $\nabla G\left(\Theta^*(t_c)\right)^T$.

Let A be an $n \times (n-k)$ matrix whose columns form a basis for T. If Y is the set of all vectors in $\Re^{n-k}$, then AY spans T. Furthermore, since $\dot{\Theta}^{*+}(t_c)$ is in T, it can be represented as $\dot{\Theta}^{*+}(t_c) = A\vec{y}$, where $\vec{y}$ is a unique element of $\Re^{n-k}$. Similarly, the set of test functions, which inherently define the tangent space, can be represented as $\eta_0^+(t_c) = A\vec{q}$, where $\vec{q}$ is any element of $\Re^{n-k}$. Substituting these expressions into Equation 8.12 gives the following relationship, which must hold for all $\vec{q}$ in $\Re^{n-k}$, at the moment of contact:

$$\left(\dot{\Theta}^{*-} - A\bar{y}\right)^T M A\bar{q} = 0 \qquad \text{at } t_c \tag{8.14}$$

By transposing Equation 8.14, Equation 8.15 follows. Recall that Equation 8.15 must hold for all $\bar{q}$ in $\Re^{n-k}$.

$$\bar{q}^T A^T M\left(\dot{\Theta}^{*-} - A\bar{y}\right) = 0 \qquad \text{at } t_c \tag{8.15}$$

Since Equation 8.15 must be satisfied *for all* $\bar{q}$ in $\Re^{n-k}$, Equation 8.16 follows.

$$A^T M\left(\dot{\Theta}^{*-} - A\bar{y}\right) = 0 \qquad \text{at } t_c \tag{8.16}$$

Equation 8.16 is altered to give the following relationship between the pre- and post-constraint generalized velocities at the time of contact, namely $\dot{\Theta}^{*-}$ and $\dot{\Theta}^{*+} = A\bar{y}$:

$$A^T M\dot{\Theta}^{*-} = A^T MA\bar{y} \qquad \text{at } t_c \tag{8.17}$$

Equation 8.17 is called the *Projection Theorem* because it is the *M*-projection of the pre-constraint system's generalized velocity into the tangent space of the surface of constraint at the moment of contact, which gives the generalized velocity of the system immediately after the constraint is imposed. It

represents a generalization of the principle conservation of momentum for constrained systems. Furthermore, if there are no constraints acting on the system, A is the identity matrix and the Projection Theorem is exactly reduced to conservation of momentum, $M\dot{\Theta}^{*-} = M\dot{\Theta}^{*-}$ at t_c.

From the Projection Theorem, Equation 8.17, it also follows that $\vec{y} = \left(A^T MA\right)^{-1} A^T M\dot{\Theta}^{*-}$. The inverse matrix in this equation will exist since A has independent columns and M is positive definite so that the product $A^T MA$ is a full-rank, $(n-k)\times(n-k)$ square matrix. Upon further substitution, the generalized velocity vector immediately after contact is given by Equation 8.18.

$$\dot{\Theta}^{*+} = A\left(A^T MA\right)^{-1} A^T M\,\dot{\Theta}^{*-} \qquad \text{at } t_c \qquad (8.18)$$

8.5 Numerical Implementation of the Projection Theorem

To calculate the post-impact segment angular velocities when a constraint is enacted in the stroke cycle, the projection theorem is applied. Recall that the post-constraint generalized velocity vector at contact is given in terms of the pre-constraint generalized velocity vector at contact by Equation 8.18, which contains an inverse matrix. Computing inverses of ill-conditioned matrices may produce large numerical errors. Therefore, if $A^T MA$ is ill-conditioned, Equation 8.18 may yield a poor computational solution.

The steps below outline the method of numerically obtaining the generalized velocity vector immediately after impact, $\dot{\Theta}^{*+}(t_c)$, without explicitly inverting $A^T MA$

and being careful to reduce numerical errors that would arise if the columns of A were to be nearly dependent. All quantities in the steps are evaluated at contact, i.e., at t_c.

1) Let M, which is symmetric and positive definite, be decomposed as $M = W^T W$. It follows from Equation 8.17 that

$$A^T W^T W A\bar{y} = A^T W^T W\dot{\Theta}^{*-} \tag{8.19}$$

2) Solve the homogeneous system $(\nabla G)^T \eta_0 = \vec{0}$ and form the matrix A whose columns provide a basis for the nullspace of $(\nabla G)^T$, that is, for the tangent space of the constraint T. Note that these column basis vectors may be near one another so that $A^T MA$ may be nearly singular and ill-conditioned. This issue will be resolved in Step 4 below.

3) Define $\tilde{A} = WA$ so that Equation 8.19 gives the following:

$$\tilde{A}^T \tilde{A}\bar{y} = \tilde{A}^T W\dot{\Theta}^{*-} \tag{8.20}$$

Note that Equation 8.20 may be considered as either the normalized equations for the least-squares problem $\tilde{A}\bar{y} = \tilde{b}$, where $\tilde{b} = W\dot{\Theta}^{*-}$, or for the weighted least-squares problem $WA\bar{y} = W\dot{\Theta}^{*-}$ (Strang 1988).

4) Factor $\tilde{A} = QR$, where Q is orthonormal and R is upper triangular and invertible. This is analogous to the Gram-Schmidt process and produces an orthonormal basis for T, causing the basis vectors to be far apart. This is important because using orthogonality in computations reduces numerical roundoff error.

5) Making these substitutions in Equation 8.12 gives the following since Q is orthonormal and R is invertible:

$$\tilde{A}^T\tilde{A}\bar{y} = \tilde{A}^T\tilde{b} \Rightarrow R^TQ^TQR\bar{y} = R^TQ^T\tilde{b} \Rightarrow R^TR\bar{y} = R^TQ^T\tilde{b} \Rightarrow R\bar{y} = Q^T\tilde{b}$$

6) Solve $R\bar{y} = Q^T\tilde{b}$ for $\bar{y}$, which is straightforward since R is upper triangular.

7) Compute the projected generalized velocity at the time of impact, $\dot{\Theta}^{*+} = A\bar{y}$.

Figure 8.2 illustrates the steps described above.

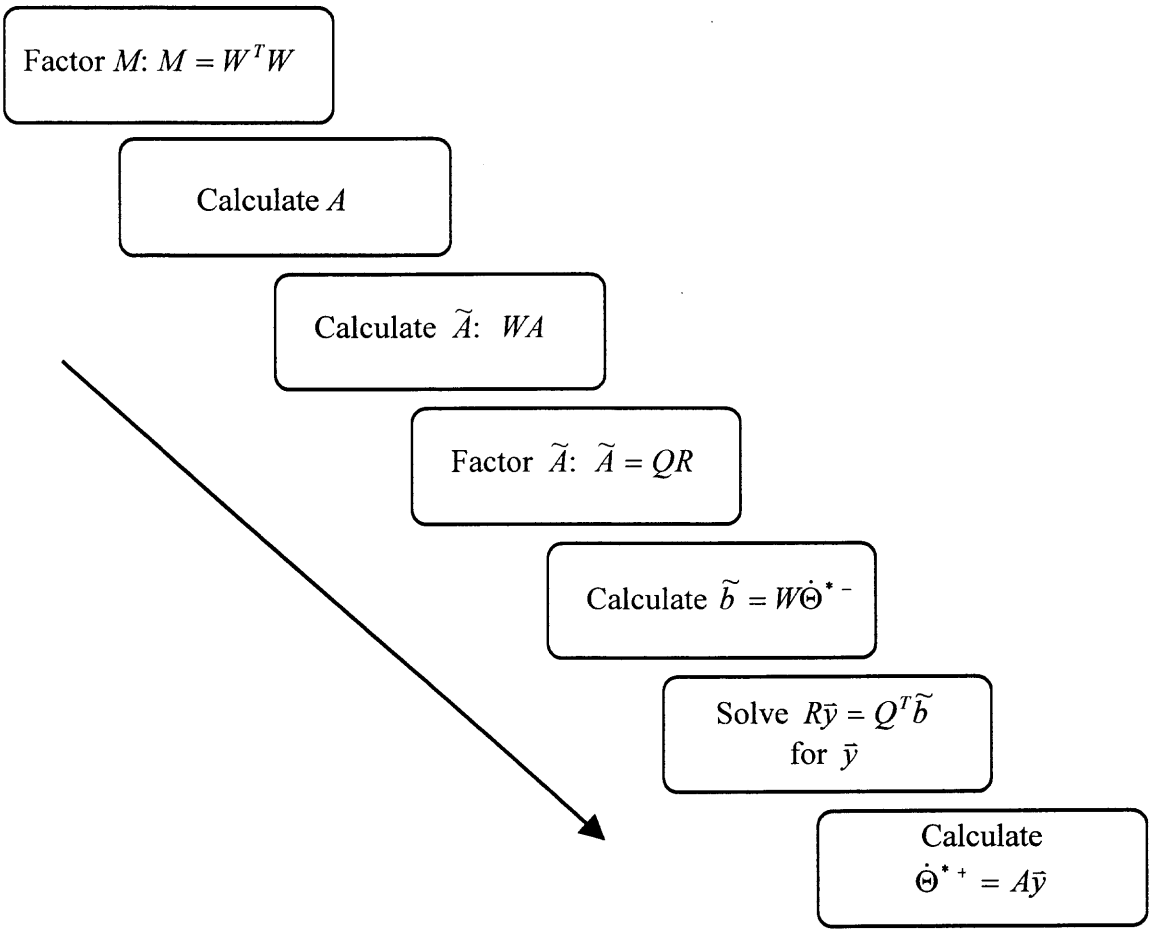

Figure 8.2 Steps taken to numerically project a the system's angular velocity vector

CHAPTER 9

MODEL RESULTS: WHEELCHAIR RACING STROKE SOLUTIONS

9.1 The Model Applied to Wheelchair Racing: Assumptions and Input

One main assumption of this model is that it is possible to divide a complete wheelchair-racing stroke into a small number, N, of consecutive ballistic phases. Mathematically, this means that N BVPs need to be solved for the segments' dynamic horizon angles and that adjacent solutions must be continuous. It is desirable to find a solution with as few phases as possible. This ensures a minimal dimension of the motion space, which will be searched for an optimal stroke technique.

In this thesis, three-phase solutions are presented. The phases are referred to as *Release 1*, *Release 2*, and *Push*. These phases have the following characteristics, where *configuration* refers to the segments' positions (horizon angles) and assumptions are indicated:

Release 1:

1) Release 1 begins immediately after the pushrim is released and continues until a specified time during the upstroke.
2) ASSUMPTION: the elbow joint is constrained to a particular range of motion and cannot exceed an indicated maximal angle during Release 1; this results in a "stiff arm segment," where the elbow angle remains fixed, in Release 1 once this constraint is enacted.

3) Release1-model segments include an upper arm, a forearm, and an unattached wheel; the motions of the arm segments and of the wheel are uncoupled during Release 1.
4) The Release 1 initial configuration is the same as the final configuration of Push; the final configuration of Release 1 is identical to the initial configuration of Release 2.

Release 2:

1) Release 2 begins after Release 1 and continues until the athlete contacts the pushrim; that is, Release 2 includes part of the upstroke as well as the full downstroke.
2) ASSUMPTION: The range of motion of the elbow joint is not constrained during Release 2. In practice, there appears to be no loss of generality in making this assumption, since elbow joint angles exceeding the maximum range of motion used in Release 1 are not observed in Release 2.
3) Release2-model segments include an upper arm, a forearm, and an unattached wheel; the motions of the arm segments and of the wheel are uncoupled during Release 2.
4) The Release 2 initial configuration is the same as the final configuration of Release 1; the Release 2 final configuration is the same as the initial configuration of Push (except for the position of the wheel segment).

Push:

1) Push begins after Release 2 and concludes the three-phase cycle.
2) To instantaneously project Release 2 final velocities, simulating the effect of pushrim impact, the duration of push can be set to 0.0 seconds. Consequently, the immediate effect of pushrim impact on the wheel and arm segment angular velocities is calculated at the beginning of this instantaneous Push by *M*-projecting the final Release 2 angular velocities into the tangent space of the Push-model in the wheel contact configuration. This process enables the effect of the impact at the moment pushrim contact to be separated from what occurs during Push.
3) Push-model segments include an upper arm, a forearm, and an attached wheel, the hub of which is fixed in position; the motions of the arm segments and of the wheel are coupled during Push.
4) The Push initial configuration is the same as the final configuration of Release 2 (except for the wheel segment); the Push final configuration is identical to the initial configuration of Release 1.

The two assumptions included in the above list are justified in a first approximation sense by Piston Cycle 1 empirical data. Specifically, the assumption that the elbow angle does not exceed a specified maximum during Release 1 is reasonable in that the experimental elbow angle remains near but does not exceed 160 degrees for an early portion of the stroke cycle. This constraint is not required during Release 2, as the

elbow angle remains well below any such maximum in the empirical data. This joint angle is graphed in Figure 9.1 below.

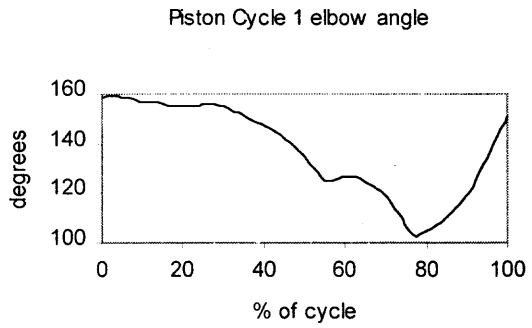

Figure 9.1 Piston Cycle 1 elbow angle

The cyclic nature of the three-phase solution is illustrated in Figure 9.2. IC_j and FC_j are abbreviations for initial configuration and final configuration of phase j, respectively. The duration of phase j is denoted t_j. Arrows in the diagram indicate equivalence.

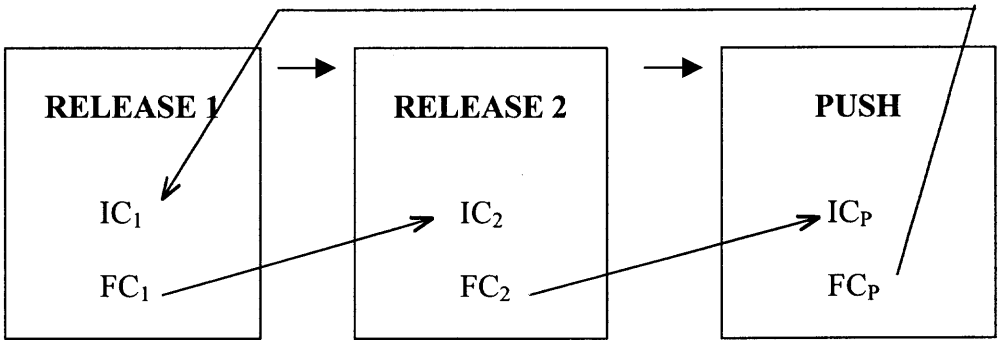

Figure 9.2 A three-phase wheelchair racing stroke solution

In such a three-phase, three-segment model solution, there are a total of ten independent parameters. These are as follows:

- initial configuration of Release 1 (upper arm, forearm, wheel) → 3
- elbow constraint angle → 1
- final configuration of Release 1 (upper arm, wheel) → 2
- time of Release 1 → 1
- final configuration of Release 2 (upper arm)[1] → 1
- time of Release 2 → 1
- time of Push → 1

Specifying these ten independent motion parameters will mathematically yield a complete model wheelchair racing stroke motion, provided that the BVPs are solvable. However, it is possible to choose another set of ten, more clinically relevant independent parameters, which would also define a model stroke. The following independent set is used in this dissertation:

1) wheel velocity (racing speed)

2-3) orientation of the athlete in the racing chair (hub-shoulder distance *and* hub-shoulder angle)

4) total cycle time ($t_1 + t_2 + t_{push}$)

5) recovery cycle time ($t_1 + t_2$)

[1] This configuration requires the specification of only *one* angle provided that the same athlete/chair orientation is assumed as in the initial configuration of Release 1.

6) wheel contact angle (wheel horizon angle at pushrim contact)

7) wheel release angle (wheel horizon angle at pushrim release)

8) elbow constraint angle during Release 1

9) upper arm horizon angle at the end of Release 1

10) Release 1 time (t_1)

To obtain a model solution, reasonable values must be chosen for each of these ten clinical parameters, which then serve as model input. Piston Cycle 1 data provides such appropriate numbers. The values are as follows:

1) The average racing speed of Piston Cycle 1 was 15.8 miles per hour, or 1226.7 degrees per second. Taking wheel linear deceleration into account by applying Equation 3.1 gives the initial wheel velocity at the beginning of Release 1: 1244.1 degrees per second.

2-3) The Piston Cycle 1 pushrim release configuration of the arm segments and the wheel, in conjunction with trigonometry, provides the orientation of the athlete in the racing chair. Figure 9.3 illustrates the pushrim release configuration from which it is determined that the hub-shoulder distance, D, is 0.490 meters and the hub-shoulder angle, θ_{hub} is –41.971 degrees.

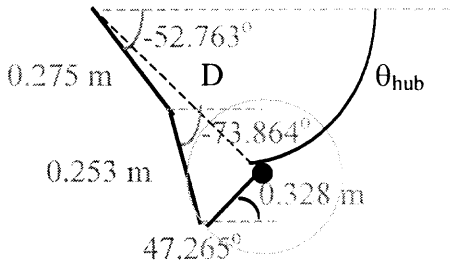

Figure 9.3 The pushrim release configuration of Piston Cycle 1

4) Piston Cycle 1 consists of 59 frames of VICON data making the total cycle time approximately 0.483 seconds.

5) The graph in Figure 9.4 shows Piston Cycle 1 horizon angle data arranged in the following order: Push – Release 1 – Release 2. At 0.033 seconds, cusp-like features are apparent in the horizon angles inferring the boundary of Push and Release 1. Thus, Push lasts 0.033 seconds, which means that the recovery cycle time is 0.450 seconds.

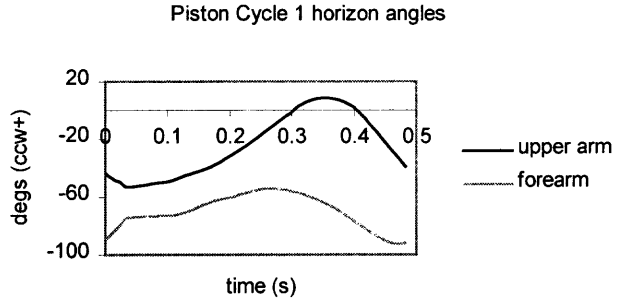

Figure 9.4 Piston Cycle 1 horizon angle data arranged in the order Push-Release1-Release2

6-7) The wheel contact angle is 37.711 degrees as determined from Piston Cycle 1 data. The wheel release angle is 47.265 degrees, as seen in Figure 9.3.

8-10) Figure 9.4 provides values for the maximal elbow joint angle, the upper arm horizon angle at the end of Release 1, and the time of Release 1. Recall that Release 1 is constrained by a maximal elbow angle. This means that when the constraint is enacted, the upper arm and the forearm horizon angles are parallel. In the figure, these horizon angles are approximately parallel from 0.033 seconds (end of Push) to about 0.208 seconds giving Release 1 time to be 0.175 seconds. During this time, the maximum elbow angle is less than 160 degrees as can be seen in Figure 9.1. At 0.208 seconds, the upper arm horizon angle is roughly –31 degrees.

9.2 A Three-Phase Model Solution

Providing the mathematical model with the ten-parameter set of input described in the previous section results in a model solution. Since this model input was obtained from Piston Cycle 1 data, model output will be compared to this experimental data once the model results are presented. In Figures 9.5 and 9.6 below, the model solution's dynamic horizon angles are graphed in the phase order of Push – Release 1 – Release 2 and the phase boundaries are indicated by vertical dashed lines. In each of the figures, empirical angles are indicated in gray for comparison.

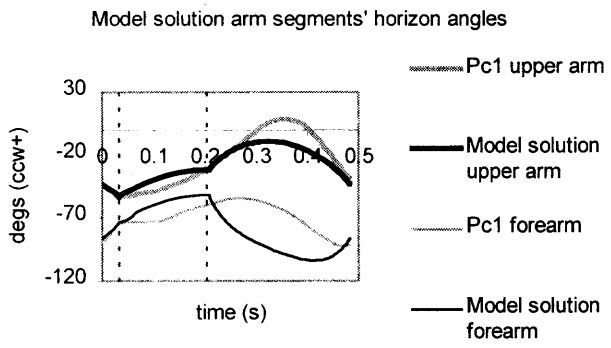

Figure 9.5 Model solution arm segments' horizon angles

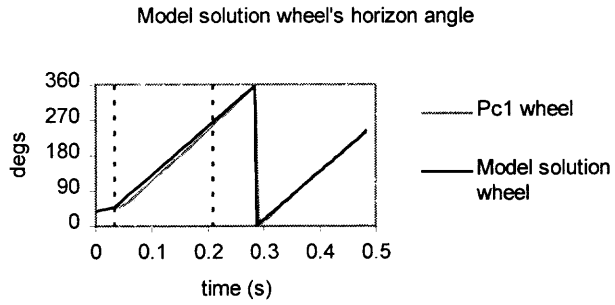

Figure 9.6 Model solution wheel's horizon angle

The model solution arm segments' horizon angles are continuous throughout the cycle. However, at several instances in the cycle angular velocity discontinuities exist. At these times, impulsive generalized forces due to either muscular effort or impact situations are present. Figures 9.7 and 9.8 show the arm segments' angular velocities and the wheel's angular velocity throughout the cycle, respectively. Again, Piston Cycle 1 data is indicated in gray and phase boundaries are shown as dashed lines.

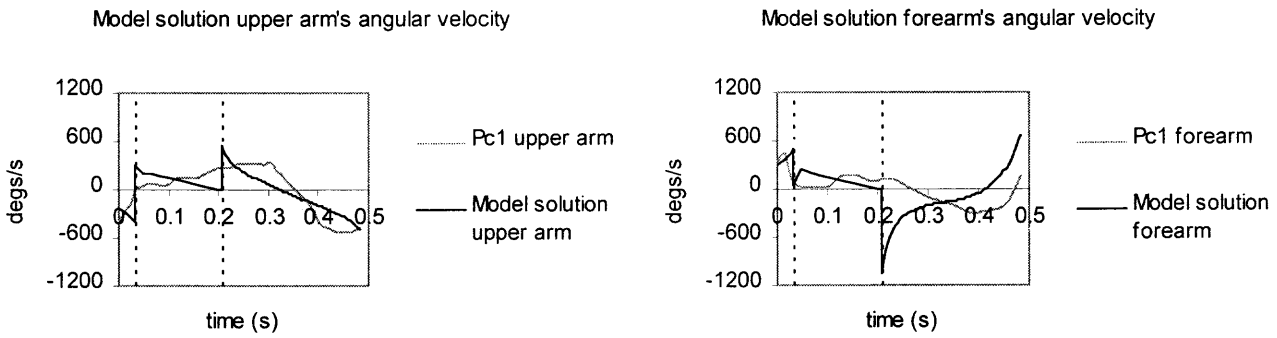

Figure 9.7 Model solution arm segments' angular velocities

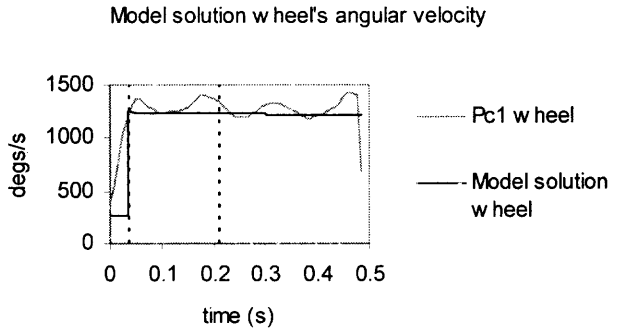

Figure 9.8 Model solution wheel's angular velocity

Instantaneous changes in velocities cause sudden gains or losses in the kinetic energy of the system. Figure 9.9 provides the total kinetic energy in the system throughout the cycle. Piston Cycle 1 data is indicated in gray and dashed lines represent phase boundaries.

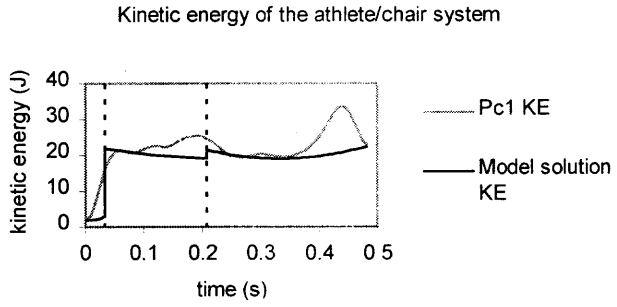

Figure 9.9 Model solution kinetic energy of the athlete/chair system

To understand the theoretical *and* empirical movements and energies, each phase's horizon angles and kinetic energies, as well as changes in kinetic energies at the phase boundaries, must be interpreted. First consider the 0.033-second Push phase, the first sections of Figures 9.5, 9.7, and 9.9. While the athlete is in contact with the wheel, the arm segments must move on the arc prescribed by the pushrim, which does not allow for much variation in terms of the trajectories of the segments. Also, since the initial and final configuration of Push were taken from Piston Cycle 1 data and the duration is only 0.033 seconds, the Push-phase BVP is easily solved to be close to the experimental angles. This explains the exceptional model-empirical match of segment horizon angles indicated in Figure 9.5. A study of the model and the empirical arm segments' horizon angles shows that following the rim of the spinning wheel during Push forces the following:

- The horizon angle of the upper arm becomes more negative as this segment flexes.
- The horizon angle of the forearm becomes less negative as this segment extends.

- The elbow angle increases as a result of a flexing upper arm and an extending forearm.

Consideration of the Piston Cycle 1 arm segments' angular velocities during the push period reveals that those of the upper arm and forearm are inversely related. That is, the upper arm's clockwise velocity increases while the forearm's counterclockwise velocity decreases after achieving a maximum. In the model solution, the arm segments' angular velocities are also inversely related. However in this case, the upper arm (clockwise) is slowing while the forearm (counterclockwise) is quickening, which is the opposite of empirical data.

The wheel rotates more slowly during Push than during the recovery phase. This is most likely because the collision of the athlete's hand (which is probably moving slower than the wheel) with the pushrim causes the wheel to slow down. Piston Cycle 1 data indicates that the wheel's velocity increases steadily through the duration of the push period. This is presumably due to the athlete imparting a quick but gradual push to the rim, allowing for the transfer of some arm segment energy to the wheel. At the end of the push period, empirical data shows the wheel velocity is maximal.

On the other hand, because model phases are ballistic the arm segments cannot gradually impart force to the wheel. Furthermore, wheel viscosity is present in the model. Therefore, the wheel velocity in the model solution is decreasing slightly throughout Push.

Throughout the stroke cycle, the wheel's kinetic energy is large relative to that of the arm segments. In Piston Cycle 1 data, the push period includes a rapid climb in the

athlete/chair system's kinetic energy, which can be explained by the large increase in wheel velocity during this time. In contrast, because the model solution's wheel velocity is almost constant, no such rise in system kinetic energy exists during Push.

Although empirical energies exhibit no discontinuities, model solution energies are characterized by kinetic energy jumps at the phase boundaries. The first such discontinuity in the system's kinetic energy is present at 0.033 seconds, or about 7 % of the stroke cycle, which is the Push-Release1 phase boundary. This immediate jump of 18.824 Joules of kinetic energy must be supplied by propulsive muscular input. This can be interpreted as a required instantaneous push when the athlete releases the rim. In a sense, the gradual increase in kinetic energy over the full duration of push in Piston Cycle 1 is reduced in the model solution to this burst of energy at pushrim release.

Next, the 0.175-second Release 1 phase is examined. The model solution arm segments' horizon angles agree with empirical at the beginning of the phase, as Piston Cycle 1 data was input for the Release 1 BVP. Recall that the model assumes that the elbow cannot exceed a maximum angle of 160 degrees during this phase. This elbow constraint forces the arm segments to move independently until this greatest permitted angle is achieved at which time the arm becomes stiff. While the elbow remains at maximal extension, the graphs of the horizon angles of the upper arm and forearm are parallel to one another, which is seen in Figure 9.5. Although the concavities of the model and empirical curves do not agree, both data indicate that the upper arm and the forearm extend during Release 1 (upstroke).

During this phase, Piston Cycle 1 analysis shows that the upper arm's counterclockwise velocity rises from zero degrees per second, representing the change in

direction of this arm segment after pushrim release. The counterclockwise velocity of the forearm slows to almost zero and then increases slightly. This indicates a pause in the angular motion of the forearm after release.

Angular velocities of the model solution arm segments disagree with those of the experimental data. While both arm segments' velocities are counterclockwise in the model solution, both decrease for most of Release 1. Furthermore, when the model elbow constraint is imposed, a collision of segments occurs resulting in a loss in angular velocity for both arm segments. Careful examination of Figure 9.7 shows this impact happens at approximately 0.066 seconds into the cycle. That is, slight arm segments' velocity discontinuities occur after 0.033 seconds of Release 1, when the elbow constraint is enacted and impact occurs. Reaching maximal elbow joint range of motion results in the arm segments' velocities being projected into the tangent space of the constraint, causing both segments to lose velocity.

Since the wheel and the arm are moving independently during this phase, the motion of the arms does not influence the wheel in any way. Figure 9.8 indicates that the Piston Cycle 1 wheel angular velocity is varying considerably here, although this is most likely an artifact of projecting the cambered wheel into the sagittal plane of the athlete. In this case, the local maxima and minima during recovery should be smoothed out of the graph. The motion of the disk wheel in the two-dimensional model will not encounter this problem, as there is no camber to the wheel. The model solution wheel's angular velocity slows linearly during Release 1, as per the model-included effect of wheel viscosity.

Release 1-phase system kinetic energies primarily increase in empirical data but decrease in the case of the model. Since no joint viscous forces are included in the model, arm segment energy is conserved within a given phase. Therefore, during Release 1 (upstroke) while arm segment potential energies are increasing, their kinetic energies must decrease. This result, along with the presence of wheel viscosity in the model, ensures a decrease in system kinetic energy during Release 1. Furthermore, as mentioned above, imposition of the elbow constraint causes an instantaneous loss in the arm's kinetic energy. In this model solution, this impact energy loss is approximately 0.374 Joules. It is important to interpret this energy loss in the system as due to a physical impact and not from muscular activity.

Another discontinuity in the model solution system's kinetic energy occurs at the Release1-Release2 phase boundary, or at 0.208 seconds of the stroke cycle. This sudden 2.297-Joule jump in system kinetic energy must be provided by a propulsive muscular effort. Most likely, this energy requirement is necessary to allow for the completion of the upstroke portion of the cycle. It is interesting to note that this burst roughly coincides with a system kinetic energy local maximum in the empirical data, perhaps offering an explanation for this Piston Cycle 1's observed energy increase.

Lastly, the 0.275-second Release 2 phase is analyzed. Release 2 includes the end of upstroke followed by downstroke. Piston Cycle 1 data reveals the following segment horizon angle behaviors:

- The graph of the upper arm's horizon angle is concave down. The upper arm first extends until reaching a maximal excursion of about 8 degrees above the

horizontal at 0.358 seconds (0.15 seconds into Release 2), the high point of the cycle. At this time, it flexes to begin the downstroke and finally contact the pushrim at the end of this period.

- The graph of the forearm's horizon angle is primarily concave down until about 0.4 seconds of the stroke cycle where a point of inflection occurs and the graph continues concave up. The elbow is flexed maximally to approximately –54 degrees at 0.267 seconds in the cycle, which is 0.059 seconds into Release 2.

Qualitatively, some of this empirical horizon angle behavior is captured by the model solution. The graph of the model upper arm angle is concave down, as it is in the experimental case. However, the solution's upper arm maximal extension angle of roughly –9 degrees at 0.325 seconds in the cycle (0.117 seconds into Release 2) occurs a bit sooner and does not allow the upper arm to achieve the height present in Piston Cycle 1 data. Furthermore, the graph of the solution's forearm angle is only concave up and does not contain a point of inflection. There allows for considerably less forearm flexion in the model solution to a maximum of only about –52, which occurs immediately at the beginning of Release 2. This does not closely coincide with the –54-degree flexion, which takes place at about 21 % of this phase in Piston Cycle 1.

During Release 2, empirical data shows the upper arm's counterclockwise velocity remaining relatively constant for a while and then slowing as this segment's maximal extension is reached. At this point, the velocity is zero, allowing for a change in direction as the segment initiates downstroke. Throughout downstroke, the upper arm's

clockwise velocity increases then levels off as the pushrim is neared. The forearm's counterclockwise velocity, which is much smaller than that of the upper arm, decreases during the first portion of the phase and reaches zero sooner than the upper arm segment. This indicates a change in direction, as the forearm comes forward toward the pushrim during downstroke. Once the forearm is positioned above the rim, it stretches down toward the rim and reverses its direction again as the forearm thrusts in extension to allow the hand to hit the rim.

The model solution arm segments' angular velocities are qualitatively the same as Piston Cycle 1 data. The upper arm's counterclockwise velocity decreases through zero (sooner than experimentally achieved) to increase in the clockwise direction. This is consistent with the explanation given above. The forearm's clockwise velocity similarly decreases through zero, at which point increasing counterclockwise velocity exists. One difference between the model solution and experimental data is that the model forearm velocity only reaches zero once indicating a sole change in angular direction. Also, the time at which this direction change occurs in the model solution is between the two direction-change empirical instances.

As for the model solution wheel's angular velocity, it once again slows linearly during Release 2. This is consistent with the wheel constant angular deceleration term present in the model. A decrease in the wheel velocity in Piston Cycle 1 data could indicate that contact with the wheel was already made. It is possible that the athlete's body rubbed against the wheel prior to pushrim contact causing it to slow. Otherwise, it could be that the stroke cycle endpoint has not accurately been identified and may actually occur a few VICON frames before it was originally identified.

Empirically, the system kinetic energy decreased, increased to a maximum, then decreased again. The first decrease in Piston Cycle 1 system kinetic energy is due to the slowing of the arm segments as they complete the upstroke portion of the cycle. At this time, descent begins and the arms speed up as they move toward the wheel, which accounts for the system kinetic energy increase. The final loss of kinetic energy is plausibly caused, at least in part, by a wheelchair athlete's skill level. That is, in order for the racer to land his hands on the pushrim accurately, the segments must slow down somewhat to allow for correct positioning. This system kinetic energy loss might also be attributed to the decrease in wheel velocity at the end of the Release2-phase time.

The graph of the system kinetic energy of the model solution in Figure 9.9 is slightly concave up. Considering that the wheel slightly loses kinetic energy throughout Release 2, this is explained, once again, by the fact that arm total energy is conserved because there is no joint viscosity included in this ballistic-phase model. Therefore, as the arms rise toward maximum height and potential energy consequently increases, kinetic energy must decrease. On the other hand, during the downstroke part of Release 2, potential energies decrease forcing kinetic energies to increase in this portion of the phase.

Assuming a cyclic racing stroke, the end of Release 2 must coincide with the beginning of Push. In other words, the original system kinetic energy must be restored via the Release2-Push phase boundary. At this pushrim contact boundary configuration, changes in system energy occur in the model as the result of both physical impact and impulsive muscle forces.

First consider the impact energy loss. Projecting the segments' angular velocities at the end of the Release 2 phase into the fixed-hub constraint tangent space is achieved by using the computational method summarized in Figure 8.2. This is implemented in the initial part of the Push phase solution. Since the attached wheel model is used in Push, the appropriate fixed-hub constraint is enforced and Release 2 ending angular velocities will be instantaneously projected to values consistent with pushrim contact without wheel displacement but allowing for instantaneous changes in wheel rotation speed and arm segments angular velocities. In the model solution, the Release 2 velocities are projected as given in Table 9.1.

Table 9.1 Projection of the segments' velocities at pushrim contact

Segment	Pre-projection angular velocity (Release 2 final velocity) in degs/s	Post-projection angular velocity in degs/s
Upper arm	-509.160	-788.842
Forearm	686.557	1016.789
Wheel	1211.613	940.960

This change in velocities results from a physical impact, namely collision of the athlete with the pushrim. It is not caused by muscle activity. In this model solution, approximately 1.897 Joules of energy was lost as a result of pushrim contact.

The final discontinuity in system kinetic energy is an effect of the assumed cyclic nature of the motion and contributes to muscle energy cost. That is, in order to perform yet another full stroke cycle, the segments' projected velocities must return to the values they have at the beginning of Push, which are –228.405, 294.406, 272.450 degrees per second for the upper arm, forearm, and wheel respectively. To do so, all segments' velocities must decrease, implying that the muscles must provide a braking force at the post-projection Release2-Push phase boundary. In this model solution, the instantaneous decrease in system kinetic energy here is approximately 18.725 Joules and must be supplied by the muscles.

From these results, it is possible to determine the mechanical energy cost per unit distance of the model solution. To complete the racing stroke cycle given by the model solution, muscles must provide the following:

- a propulsive action to create 18.824 Joules of mechanical energy at the Push-Release1 phase boundary (at the instant of pushrim release)
- a propulsive action to create 2.297 Joules of mechanical energy at the Release1-Release2 phase boundary
- a braking action to remove 18.725 Joules of mechanical energy at the post-projection Release2-Push phase boundary

Consider the braking action listed above. Since muscles must provide impulsive forces at this time, it is assumed here that this braking action of muscles, which removed mechanical energy from the pendulum-wheel system, requires metabolic energy and,

therefore, must be tallied as an energy cost. From the principle of the conservation of energy, work is being performed by the pendulum-wheel system on the muscles. Although some of this work might be stored as potential energy in elastic structures such as muscle ligaments and tendons, this stored-energy contribution is assumed to be negligible compared to that which is dissipated as thermal energy. In other words, it is assumed that the braking muscle action requires metabolic energy to produce impulsive forces, which remove system mechanical energy as heat, in a similar way that metabolic energy is required to produce impulsive muscle forces, which add mechanical energy to the pendulum-wheel system. Furthermore, it is assumed that the metabolic muscle energy costs are proportional to the sum of the absolute values of the mechanical (non-impact) energy changes in the wheelchair stroke. Thus, the sum of these absolute-value mechanical (non-impact) energy changes per unit distance will be a measure of the metabolic energy required to move the athlete/chair system a unit distance while performing that racing stroke technique.

In the model solution described in this section, the muscles are required to create a total of 39.846 Joules of mechanical energy for this racing stroke technique to be performed. Since a distance of 3.218 meters is covered in this 0.483-second cycle, the mechanical energy cost per unit distance of this stroke method is 12.382 Joules per meter. Alternatively, the mean muscle mechanical power per unit distance is 25.636 Watts per meter. Furthermore, in performing the model-suggested racing technique a total of 2.271 Joules of energy are lost due to physical impacts (elbow lock and pushrim contact). If this is normalized to distance traveled, approximately 0.706 Joules per meter are lost through impacts.

9.3 A Twenty-Phase "Inverse" Model Solution

As was mentioned in Chapter 7, the model can be used in an inverse fashion by breaking the racing stroke down into *many* ballistic phases, allowing the muscles to act frequently (at many phase boundaries) throughout the cycle. Such an inverse analysis of Piston Cycle 1 data was conducted. The "inverse" solution consisted of an eighteen-phase recovery period (seventeen 0.025-second phases and one 0.008-second phase) and a two-phase push period (two 0.025-second phases). Figure 9.10 shows this twenty-phase "inverse" model solution arm segments' horizon angle in the Push1-Push2-Release1-Release2-...-Release18 order. The empirical data is indicated in gray for comparison. Because so many phases exist, dashed lines have not been used in Figure 9.10 to indicate them, but they exist approximately every 0.025 seconds.

The extremely close empirical-theoretical match is a direct result of the large number of very short duration phases. That is, solving a 0.025-second BVP, with initial and final configurations given by Piston Cycle 1 data, does not allow for much deviation from the experimentally performed trajectory.

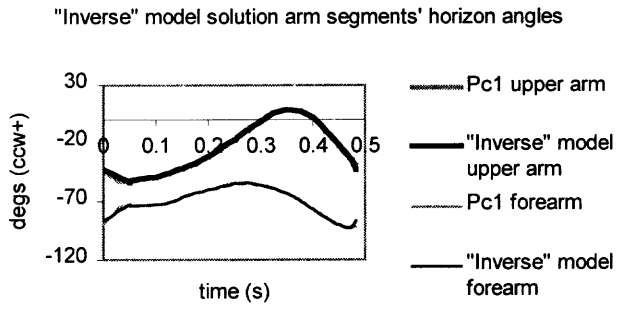

Figure 9.10 "Inverse" model solution arm segments' horizon angles

Figure 9.11 indicates the "inverse" model solution system's kinetic energy results. Recall that phase-boundary discontinuities are attributed to impulsive muscular input and/or the presence of impulsive impacts. Also remember that the motion is considered cyclic, requiring consideration of the relationship between the final and initial energies indicated.

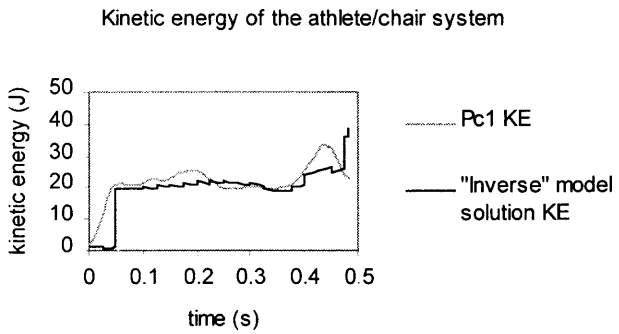

Figure 9.11 "Inverse" model solution kinetic energy of the athlete/chair system

Overall, the "inverse" model solution system's kinetic energy graph displays similar qualitative behavior to that of Piston Cycle 1. Since model phases are ballistic, small changes in energy at phase boundaries suggest the ballistic nature of the athlete's actual technique at these times in the stroke cycle. In other words, the natural flow of physical momentum and energy between the arm segments and the gravitational field is incorporated into the athlete's racing method during these time periods. Figure 9.11 reveals that a large portion of the racer's recovery phase, from approximately 0.05 seconds to 0.4 seconds, exhibits this ballistic behavior.

On the other hand, large energy increases or decreases at phase boundaries indicate muscular action. Empirical EMG data can be used to corroborate this interpretation of model output. The "inverse" model solution system's kinetic energy graph in Figure 9.11 implies that the athlete significantly used muscle during the recovery period's downstroke, at pushrim contact, and at pushrim release. This explanation can be used to interpret the Piston Cycle 1 system's kinetic energy graph.

To calculate the muscular energy cost of the athlete's racing technique, the absolute values of the changes in mechanical energy present at appropriate phase boundaries must be added. This number represents the total mechanical energy change caused by either muscular propulsion or braking. The total mechanical muscular energy cost of the stroke technique produced by this "inverse" model solution is 81.193 Joules, or 25.231 Joules per meter. Accepting this "inverse" solution as representative of the actual stroke technique implies that the wheelchair racer's current stroke technique costs 25.231 Joules per meter. Note that this value is slightly more than twice the 12.282-Joule per meter muscular energy cost of the technique given by the three-phase model solution. This suggests that the athlete could improve his racing method if he were trained to use his muscles less often (at only three specified times in the stroke cycle) and to incorporate the spontaneous energy transfers between segments and the gravitational field that can occur from an appropriate ballistic motion. That is, if he could perform the technique that more closely approximates the three-phase model solution.

As for the impact energy loss, pre-projection system kinetic energy at the end of Release 18 must be subtracted from post-projection system kinetic energy. No energy is lost due to the elbow reaching its maximum angle because in this "inverse" model such a

constraint was not included. Therefore, the impact energy loss is solely due the collision at pushrim contact. In this solution, 2.290 Joules of energy were lost at impact, making the impact energy loss 0.712 Joules per meter. Comparing this with the 0.706-Joule per meter cost of the three-phase model solution indicates no significant difference.

9.4 The Search for an Optimal Technique

It has already been suggested that the athlete modeled in this thesis could improve his mechanical energy efficiency by changing his wheelchair-racing technique. In fact, the three-phase model solution stroke was found to cost half the muscular energy expenditure than the actual motion performed. An important question to answer is whether the model could produce other solutions, which are even more efficient than the particular three-phase solution already described in Section 9.2. A search for such an optimal three-phase wheelchair racing stroke technique will be described in this section.

Varying the ten independent stroke parameters simultaneously in the three-phase stroke cycle creates a ten-dimensional motion space. In this thesis, a three-dimensional subset of this full motion space is considered in search of a model-suggested optimal stroke technique. That is, seven parameters are specified constants, while the other three are systematically varied to produce a subset of potential strokes in the three-dimensional subspace of possible new solutions. The seven fixed parameters are as follows:

- the initial wheel velocity = 1244.1 degrees per second
- the orientation of the athlete in the racing chair = 0.490 meters and –41.971 degrees

- the total cycle time = 0.483 seconds
- the recovery phase time = 0.450 seconds
- the wheel contact angle = 37.711 degrees
- the wheel release angle = 47.265 degrees

The three alterable parameters are then the elbow constraint angle during Release 1, the upper arm horizon angle at the end of Release 1, and Release 1 time. Varying these three parameters corresponds to altering the configuration and timing of the muscular effort during the recovery phase idealized in the three-phase model to the interphase time and configuration at the Release1-Release2 boundary. Piston Cycle 1 data indicates that the elbow angle does not exceed 160 degrees while the stiff arm segment exists. A reasonable maximal elbow angle range to search is from 160 degrees to 180 degrees. The empirical data also implies that the upper arm horizon angle at the end of Release 1 could realistically be between –51 and –20 degrees. In addition, Release 1 could conceivably be as short as 0.04 or as long as 0.22 seconds. (Refer to Figures 9.1 and 9.4.)

These allowable ranges of the three variables specify a volume, which must be searched. Figure 9.12 gives a pictorial representation of an example of searching this three-dimensional subset of the motion space. Each grid point in the figure represents a model solution, which would have an associated muscle mechanical energy cost and impact energy loss.

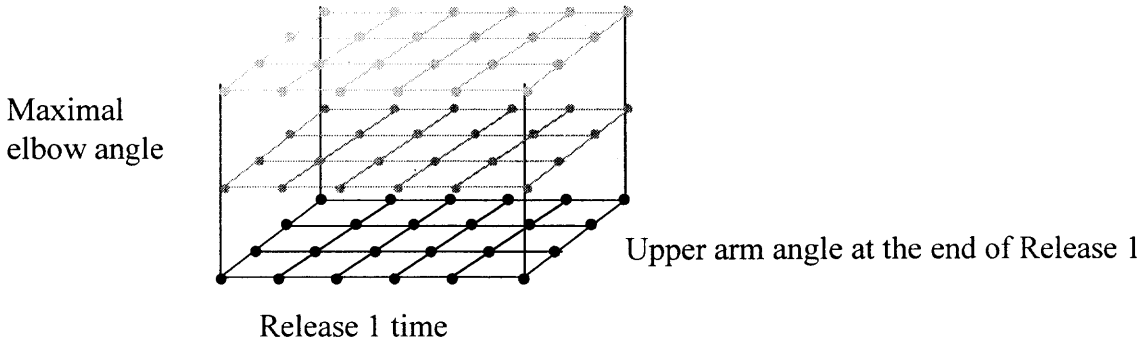

Figure 9.12 A three-dimensional subspace of the athlete's motion space

The motion subspace search produces a large number of three-phase model solutions, each with a calculated mechanical energy cost and impact energy loss. These numbers are shown in Table 9.2 for a sample of search-generated solutions where the elbow angle could not exceed 160 degrees. In this table, impact energy loss is indicated parenthetically. Since wheel velocity and total cycle time are not varied, every cost/loss value corresponds to travelling 3.218 meters. All energy values are given in Joules. The highlighted box represents the solution in this table, which most closely matches Piston Cycle 1 parameters.

Table 9.2 Muscle energy cost / impact energy loss of many model solutions

Upper arm angle at Release 1 end ↓							
-20°	79.629 (2.647)	51.467 (1.945)	46.435 (1.915)	44.965 (1.801)	43.275 (1.699)	42.257 (1.647)	41.505 (1.578)
-24°	68.834 (2.455)	47.242 (1.904)	45.149 (1.896)	43.711 (1.824)	42.276 (1.850)	41.149 (1.855)	40.266 (1.847)
-27°	59.776 (2.227)	45.966 (1.991)	44.345 (1.966)	42.776 (1.907)	41.275 (2.029)	40.054 (2.091)	39.052 (2.148)
-31°	51.763 (2.188)	45.129 (2.170)	43.403 (2.090)	41.782 (2.132)	40.301 (2.231)	38.991 (2.356)	37.881 (2.478)
-35°	46.262 (2.303)	44.434 (2.152)	42.634 (2.157)	40.942 (2.265)	39.386 (2.434)	37.993 (2.624)	36.783 (2.816)
-39°	45.614 (2.359)	43.707 (2.201)	41.839 (2.283)	40.083 (2.455)	38.460 (2.685)	36.986 (2.941)	35.690 (3.205)
-43°	44.978 (2.294)	42.997 (2.269)	41.059 (2.428)	39.237 (2.671)	37.565 (2.958)	36.030 (3.278)	34.655 (3.616)
-47°	44.360 (2.262)	42.288 (2.367)	40.292 (2.599)	38.423 (2.903)	36.703 (3.252)	35.122 (3.637)	33.676 (4.051)
-51°	43.759 (2.258)	41.613 (2.474)	39.565 (2.780)	37.645 (3.152)	35.877 (3.567)	34.241 (4.024)	32.740 (4.514)
→ Release 1 time (s)	0.04	0.07	0.10	0.13	0.16	0.19	0.22

Several general trends concerning muscular energy costs are noticed by examining Table 9.2. These trends are depicted in Figure 9.13.

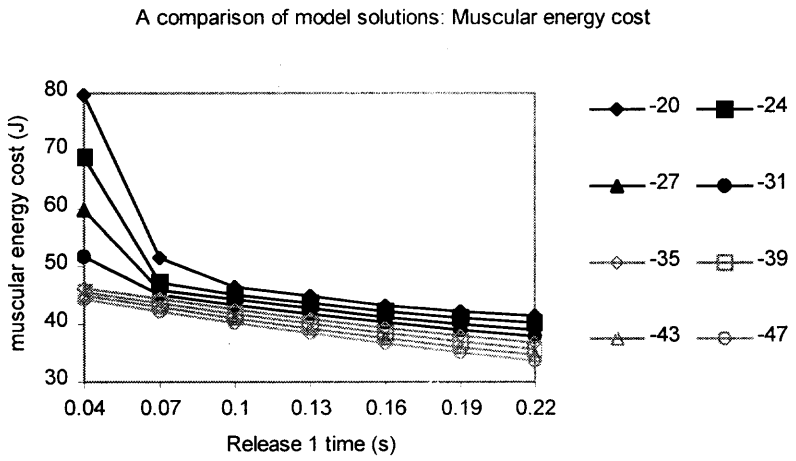

Figure 9.13 Trends in muscular energy costs of several model solutions

As can be seen in Figure 9.13, increasing Release 1 time decreases muscle energy cost independent of the upper arm angle at the end of Release 1. Furthermore, this decrease occurs very quickly when the end upper arm angle is high. This is intuitive because requiring the upper arm to rise relatively high in a short amount of time would take a large burst of propulsive energy. Allowing more time to raise would make this motion easier to produce and require a smaller energy spurt. As the upper arm need not necessarily achieve such height, permitting more time for the segment to rise does not impact the muscle energy cost as much. Figure 9.13 also shows that, regardless of Release 1 time, increasing the upper arm angle at the end of Release 1 correlates to an increase in muscle energy cost. Analogous to the preceding discussion, this effect is most pronounced for the shorter Release 1 times.

Inspection of Table 9.2 also reveals some trends concerning impact energy losses. Unlike the graph depicting muscular energy costs in Figure 9.13, however, the impact energy loss graph is not monotonic. Impact energy loss graphs for Release 1 times fixed

between 0.04 and 0.10 seconds exhibit local maxima and minima as can be seen in Figure 9.14. For the rest of the considered Release 1 times, however, the energy loss due to impact decreases as upper arm angle increases. Similar behavior occurs if the upper arm angle is fixed between –43° and –24° where local minima points exist as Release 1 time is varied. A sample of these curves is shown in Figure 9.15.

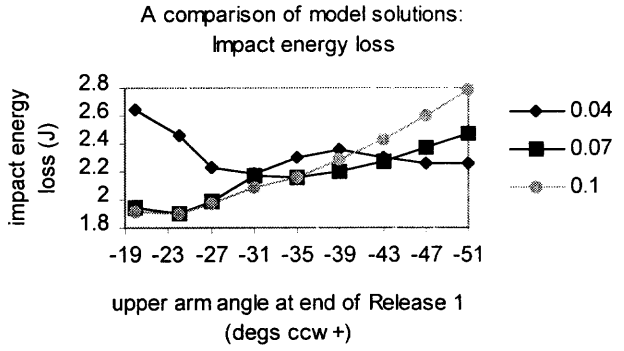

Figure 9.14 Trends in impact energy losses of several model solutions (Release 1 times fixed)

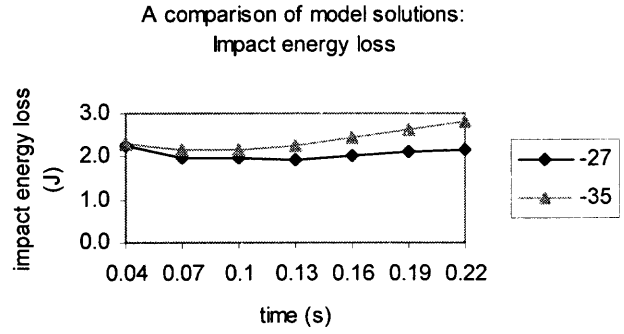

Figure 9.15 Trends in muscular energy costs of several model solutions (Upper arm angle at the end of Release 1 fixed)

It is not surprising that animations of solutions nearby one another on the chart have a similar look. However, observing those further from one another reveals a wide variety of possible wheelchair racing stroke techniques, all of which agree on the eight set stroke parameters. To highlight the variations among solutions, four of the sixty-three table solutions along with the three-phase solution of Section 9.2 will be discussed. Solutions will be named as follows: Release1 time – Release1 upper arm final angle – Maximum elbow angle. The five solutions to be discussed are given in Table 9.3.

Table 9.3 Model solutions and their energy costs/losses

Model solution	Muscular Energy Cost (J)	Impact Energy Loss (J)	Location in Table 9.2
0.04, –51,160	43.759	2.258	Lower left-hand corner
0.04, –20,160	79.629	2.647	Upper left-hand corner
0.17, –31,160	39.846	2.272	Three-phase model solution of Section 9.2
0.22, –20,160	41.505	1.578	Upper right-hand corner
0.22, –51,160	32.740	4.514	Lower right-hand corner

The five model solutions each look quite different when animated. 0.04, –51,160 looks exactly like a mechanical piston, as it is characterized by an up-and-down motion throughout which the wrist remains very close to the pushrim. In this stroke technique, the wrist trajectory runs parallel to the pushrim during the upstroke, then proceeds

vertically upward until downstroke is initiated at which point it travels vertically downward until it follows the rim's arc once again. This stroke technique will be called the *piston stroke*.

In contrast, the wrist trajectory of 0.04, –20,160 is very circular. The wrist travels up and back after release and then lifts during the upstroke to a point above the circle made by the pushrim. During downstroke, the wrist appears to travel parallel to the rim for the entire duration until contact is made. The arm segments undergo a lot of excursion in this technique. This stroke technique will be known as the *roundest stroke*.

The stroke of 0.17, –31,160 is not quite as round looking as the roundest stroke (0.04, –20,160). The wrist seems to stay well inside the pushrim circle for the entire cycle, reducing the total excursion of the arm segments. That is, the wrist trajectory is not parallel to the pushrim arc in this technique. Furthermore, this technique was developed by matching the ten stroke parameters of Piston Cycle 1. This stroke technique will be referred to as the *Piston Cycle 1 – like stroke*.

0.22, –20,160's stroke lacks the roundness at the end of Release 1 that characterizes the Piston Cycle 1 – like stroke (0.17, –31,160) and the empirical technique. The trajectory of the wrist is more elliptical and does not run parallel to the rim at all. Nonetheless, it looks like a reasonable pushing stroke. This stroke technique will be called the *elliptical stroke*.

The stroke given by 0.22, –51,160 does not look like a true racing stroke in that it is characterized by minimal arm segment excursion. It looks like a slight swinging of the arms, in a pendular fashion. After release, the wrist proceeds up and back from the rim (but not high at all). Next the wrist moves toward the rim running parallel to its arc to a

point higher than the prescribed contact. At this time, it moves back down, still with the rim's arc, until the arm segments are in the prescribed contact configuration. Thus, the wrist is near the pushrim throughout the stroke cycle. This solution involves a small movement relative to the other model solutions. This stroke technique will be known as the *pendulum swing stroke*.

The maximum upper arm horizon angle (shoulder extension) achieved by the five solutions also varies widely. Maximal shoulder extension, from largest to smallest, is as follows: 25.211° (roundest), 7.382° (piston), –8.321° (elliptical), –9.258° (Piston Cycle 1 – like), –29.351° (pendulum swing). When compared to the 8.379 degrees achieved in Piston Cycle 1, the piston stroke is closest. The large excursion of the segments in the roundest stroke caused its too great extension, whereas the minimal excursion of the pendulum swing stroke did not allow for enough extension.

Although the elbow angle was constrained in all the solutions to not exceed 160 degrees, its minimum during the entire cycle differed greatly in these five solutions. Moreover, minimal elbow angle is an observable characteristic of the solutions' animations. Piston Cycle 1 minimum elbow angle is 101.127 degrees, which is much more obtuse than 62.696° (piston), 70.370 ° (roundest), and 90.965 ° (Piston Cycle 1 – like). Both the elliptical stroke and the pendulum swing stroke, with 101.103° and 102.418° respectively, came closest to the empirical minimal angle. From this analysis it is suggested that stroke solutions with large excursions include minimal elbow angles that are too acute.

In terms of the mechanical muscular energy costs of the solutions, although they vary greatly from a minimum of 32.740 Joules to a maximum of 79.629 Joules, all except

one solution has the following required muscle activity pattern: propel (Push-Release1 boundary), propel less (Release1-Release2 boundary), brake (projected Release2-Push boundary). The sole exception requires a propel-brake-brake pattern. These results imply by continuity that a two-phase wheelchair racing cycle should exist where no muscle energy change occurs at the Release1-Release2 boundary. In other words, the entire recovery period is a single ballistic phase.

At the Push-Release1 boundary, the following muscular energy requirements exist: 41.206 J (roundest), 20.484 J (elliptical), 18.824 J (Piston Cycle 1 – like), 17.319 J (pendulum swing), and 16.678 J (piston). Muscle energy input of –14.958 J (roundest), 6.531 J (piston), 2.297 J (Piston Cycle 1 – like), 1.446 J (pendulum swing), and 1.056 J (elliptical) are necessary at the Release1-Release2 boundary. And, to complete the cycle at the projected Release2-Push boundary, –23.465 J (roundest), –20.549 J (piston), –19.965 J (elliptical), –18.725 J (Piston Cycle 1 – like), and –13.974 J (pendulum swing) must be supplied by muscular braking action.

These three boundary muscular energy requirements can be explained by studying the solutions and is seen in their animations. The first boundary energy cost seems dependent on the end of Release 1 upper arm segment angle requirement. The strokes demanding upper arm angles of -20° have the largest first boundary energy costs, whereas those needing to reach only -51° have the smallest. The second boundary energy cost appears to be related to Release 1 time allowance. That is, the shorter Release1-time solutions also have the greatest muscular energy costs at this boundary. The third boundary energy cost is associated with the cyclic assumption of the stroke. It

seems related to the amount of excursion achieved by the stroke technique, with techniques covering larger distances having higher braking muscular needs at this point.

In summary, the muscular energy requirements from highest to lowest are given in the following list:

the roundest stroke (0.04, –20,160)	→ 79.629 Joules
the piston stroke (0.04, –51,160)	→ 43.759 Joules
the elliptical stroke (0.22, –20,160)	→ 41.505 Joules
the Piston Cycle 1 – like stroke (0.17, –31,160)	→ 39.846 Joules
the pendulum swing stroke (0.22, –51,160)	→ 32.740 Joules

Impact energy losses are also important. It is not surprising that the roundest stroke has the largest elbow impact energy loss of 1.291 Joules. This collision energy loss is seen in the animation, where the forearm is thrust into extension as the arm segments speed through Release 1 and a high final angle for the upper arm is reached. All other solutions have elbow impact losses less than half of this solution's.

Impact energy losses sustained when the athlete contacts the pushrim are more substantial in all cases. The amount of this loss is dependent on how close the segments' angular velocities are to the tangent space of the fixed-hub constraint. If the trajectory is such that the pushrim is being approached tangentially, then projected momentums will be closer to pre-projected values and less energy loss will occur. The pendulum swing stroke had the greatest pushrim-contact impact energy loss at 4.312 Joules. This loss can be observed in the animation as the forearm segment approaches the pushrim almost

perpendicularly. It seems reasonable that this would cause a large decrease in segments' velocities at collision. In contrast, the stroke with the least pushrim-contact energy loss of 1.056 Joules is the elliptical stroke.

In summary, the impact energy losses from highest to lowest are given in the following list:

the pendulum swing stroke (0.22, –51,160)	→ 4.514 Joules
the roundest stroke (0.04, –20,160)	→ 2.647 Joules
the Piston Cycle 1 – like stroke (0.17, –31,160)	→ 2.272 Joules
the piston stroke (0.04, –51,160)	→ 2.258 Joules
the elliptical stroke (0.22, –20,160)	→ 1.578 Joules

Searching the three-dimensional subspace of the athlete's motion space generates many model solutions. A grid of solutions similar to that shown in Table 9.2 is created for each maximal elbow angle considered in the exploration The patterns described above for the case of an elbow constrained to not exceed 160 degrees existed for other specified elbow angle maxima. Furthermore, the muscle energy cost and the impact energy loss at corresponding grid points were higher and lower respectively as the maximal elbow angle increased.

The analysis of five solutions (160-degree elbows) revealed that numerous racing stroke techniques are possible and each has unique characteristics, which describe them. Furthermore Table 9.3 suggests that of these five the most muscular energy efficient stroke is the pendulum swing stroke, whereas that which minimized impact energy loss is

the elliptical stroke. The same is true for similar looking strokes, which were produced by models that included different maximum elbow angles.

It is interesting that the most muscular-efficient pendulum swing stroke found in the search looked least like the athlete's racing method modeled in this study. Perhaps this is because not much must be done to maintain the specified fast racing speed under experimental racing conditions (with minimal wheel friction). In this case, employing a pendulum swing stroke would maintain the wheel velocity with the least amount of muscular effort.

On the other hand, there are many instances during actual wheelchair racing when wheel deceleration is greater than the experimental conditions modeled in this thesis, namely on the CompuTrainer with minimal free wheel energy dissipation. For example, wheel speed decreases quickly when racing on a rough road surface and especially when traveling uphill. Under these circumstances, the pendulum swing stroke would most likely not be capable of maintaining the prescribed wheel speed without a considerable increase in muscular effort. That is to say, another stroke technique may be more energy efficient in these cases.

It is also important to consider the role that impact energy loss plays in choosing a stroke technique. It is plausible that there is a threshold to the amount of impact energy, or impact forces, that an athlete can withstand without causing pain and/or doing damage to his or her joints. If this limit were quantifiable, perhaps some of the search-generated stroke solutions would be disregarded as physiologically unavailable. Removing these injurious techniques may reveal a true *best* solution that the athlete is capable of

achieving. This would validate the use of this model in guiding wheelchair racers toward optimal performances.

CHAPTER 10

CONCLUSION

10.1 A Summary of the Model and Results

The mathematical model presented in this thesis includes many assumptions, which reduce the complexity of movement. These simplifications include restricting the motion to the sagittal plane, representing the body segments as point masses, and condensing continuous muscle activity into a discrete number of instances throughout the movement. It has been shown in this thesis, however, that even such an elementary model is capable of offering insight into the kinematics of motion, specifically wheelchair racing, and capturing much of its essence.

Animation and anlaysis of model output strokes revealed close agreement with an experimental technique. Furthermore, since most model-produced racing methods presented in this work contained only three phases, it seems possible to simulate the trajectory of the arm segments during a wheelchair racing stroke by concatenating relatively few ballistic-phase model solutions. This means that muscles need not be active continuously throughout the stroke cycle, which in turn intimates that the model may be useful in suggesting possible ways to increase the athlete's mechanical energy efficiency.

Using the model in an inverse fashion enabled the calculation of an approximated muscular energy cost per unit distance of the racer's current technique. Modeling

techniques found in the literature have not been able to separate the amount of system kinetic energy provided by muscular effort from that due to transfer of energy between segments and the gravitational field. For that reason, determining the muscular mechanical energy efficiency of a given movement has not been very accurate in the past. This is one of the primary contributions to the field of movement analysis that this new modeling technique offers.

Moreover, the muscular energy cost of the performed experimental stroke was found to be twice as high as other racing methods found by the model. This suggests that a stroke can be accomplished rather efficiently by exploiting the natural exchange of energy between the segments and the gravitational field, which reduces the athlete's required muscular effort. An analysis of several model-determined possible racing techniques, which were consistent with several specified wheelchair racing stroke parameters, was conducted. The results of this investigation provided insight into stroke kinematics and energetics.

The achievements detailed above describe the original contributions of work included in this thesis to the fields of motion analysis and applied mathematics. In summary, this research provides the following new information: the limitations caused by the two-dimensional nature of the model are established; the model is used in an inverse fashion to calculate the muscular mechanical energy cost of a performed wheelchair racing stroke; model output is used to guide the biomechnical analysis of an actual stroke technique; both coupled *and* uncoupled motion of components of the athlete/chair system are modeled; a geometric derivation of the equations of motion of the system and the

projection theorem (when constraints are imposed) is given; and improvements upon the shooting method boundary-value-problem solving technique are made.

10.2 Suggestions for Future Work

Although the model was successful in reproducing the qualitative behavior of a three-dimensional motion in this thesis, it definitely has limitations. Applying this two-dimensional model to movements which involve large excursions outside the sagittal plane would not be prudent. It is therefore suggested that the model be expanded to include some part of this out-of-the-plane motion, but not necessarily to incorporate the full range of three-dimensional space. For example, in wheelchair racing it is important to allow the upper arm to move in the frontal plane, enabling this segment to abduct or adduct. If this were accomplished in the model, butterfly strokes could also be studied. Adding this one degree of freedom to the *n*-segment model would be a first step toward a full, three-dimensional model.

Furthermore, it was pointed out in Section 4.5.2 that a large part of the system's kinetic energy comes from considering the rotation of distributed-mass segments. Therefore, it is proposed that the model be modified to represent the arm segments as distributed masses, rather than employ the current point-mass idealization. This would hopefully provide more accuracy in determining kinetic energy, which would improve the calculation of the muscular energy cost and impact energy loss of a given stroke technique.

As for the capabilities of the model to identify the *optimal* racing stroke, there are several opportunities for improvement. It was proposed in Section 9.4 that there might be

a maximal impact energy loss that the athlete could absorb without becoming injured. Calculating the pushrim impact force from model output would provide necessary input to an inverse model, so that joint reaction forces and moments could be determined. If the model described in this thesis could output impact forces, then motion labs not equipped with such impact-measuring instruments as the SMART Wheel could use the model to resolve these quantities instead.

Also, it might be insightful to change the experimental racing conditions by increasing wheel friction or by reducing racing speed to see whether a search of an individual's motion subspace under these circumstances would reveal an optimal motion. In this thesis, only three of ten stroke parameters were varied in ranges suggested by empirical data. As a first improvement, the ranges of these parameters could be widened to include values beyond those suggested experimentally. Expanding the subspace search might produce a better technique, which is completely different from what racers currently do. This is reminiscent of the *Fosbury flop* technique, in which high jumpers propel their bodies over the bar backward. When this technique first appeared it was unlike anything seen up to that point in time and completely revolutionized the sport of high jumping. Perhaps such a wheelchair racing technique could be discovered by a larger search. Lastly, it is also suggested that other stroke parameters be altered to find their effects on the racing method. It would be interesting to explore a larger motion subspace or even the full ten-dimensional movement space itself.

APPENDIX A

THE DERIVATION OF THE MOMENTS OF INERTIA THROUGH THE CENTER OF MASS AND THE LOCATION OF THE CENTER OF MASS FOR THE FRUSTRUM

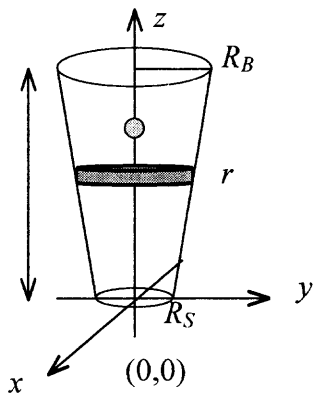

First, the volume is calculated. From the figure above, it follows that

$$Volume_{total} = V = \int_0^L \int_0^{2\pi} \int_0^{\alpha} r dr d\theta dz = \frac{\pi L}{3}\left(R_S^{\,2} + R_S R_B + R_B^{\,2}\right), \text{ where}$$

$\alpha = \left(\frac{R_B - R_S}{L}\right) z + R_S$ and R_S and R_B are the small and big radii of the frustrum

respectively. Assuming constant density of the solid, the density, ρ, is given by

$$\rho = \frac{M}{V} = \frac{3M}{\pi L\left(R_S^{\,2} + R_S R_B + R_B^{\,2}\right)}.$$

Next, the moments of inertia about the three axes are calculated.

$$I_x = \rho \int_0^L \int_0^{2\pi} \int_0^{\alpha} \int_0^{r} \left(r^2 \sin^2\theta + z^2\right) r\,dr\,d\theta\,d\theta\,dz = \frac{\pi\rho L R_B^{\,4}}{60}\left[3\left(\mu^4 + \mu^3 + \sigma\right) + \frac{2L^2}{R_B^{\,2}}\left(\mu^2 + 3\mu + 6\right)\right]$$

$$= \frac{M}{20\sigma}\left[3\left(R_S^{\,2}\sigma + R_S R_B + R_B^{\,2}\right) + 2L^2\left(\mu^2 + 3\mu + 6\right)\right]$$

And by symmetry, $I_y = I_x$.

$$I_z = \rho \int_0^L \int_0^{2\pi} \int_0^{\alpha} \int_0^{r} r^3\,dr\,d\theta\,d\theta\,dz = \frac{\pi\rho L}{10}\left(R_S^{\,4} + R_S^{\,3}R_B + R_S^{\,2}R_B^{\,2} + R_S R_B^{\,3} + R_B^{\,4}\right) = \frac{3M}{10\sigma}\left(R_S^{\,2}\sigma + R_S R_B + R_B^{\,2}\right)$$

where α and ρ are given above, $\mu = \frac{R_S}{R_B}$, and $\sigma = 1 + \mu + \mu^2$.

These equations must be adjusted via the parallel-axis theorem in order to provide moments of inertia about axes that run through the center of mass of the frustrum. The parallel-axis theorem states that $I = I_{cm} + Mh^2$, the moment of inertia about a given axis equals the sum of the moment of inertia about a parallel axis through the center of mass and the product of the mass and the distance separating these axes squared. In order to find the moments through the center of mass, the *z*-axis coordinate of the center of mass is determined below. (Clearly, the *x*- and *y*-coordinates of the center of mass are both zero by the symmetry of the solid.)

Since $z_{cm} = \frac{I_{xy}}{M}$, the required mass ($M$) and the moment about the *xy*-plane (I_{xy}) are found as follows: $Mass = M = \rho V = \frac{\rho\pi L}{3}\left(R_S^{\,2} + R_S R_B + R_B^{\,2}\right)$ and

$I_{xy} = \rho\pi \int_0^L z\left[\left(\frac{R_B - R_S}{L}\right)z + R_S\right]^2 dz = \frac{\rho\pi L^2}{12}\left(R_S^{\,2} + 2R_S R_B + 3R_B^{\,2}\right)$. Thus,

$z_{cm} = \frac{L}{4\sigma}\left(\mu^2 + 2\mu + 3\right)$, where μ and σ are defined as before.

Now apply the parallel-axis theorem ($I_{cm} = I - Mh^2$ where h is just z_{cm} for $I_{x,cm}$ and $I_{y,cm}$ and zero for $I_{z,cm}$) to get

$$I_{x,cm} = I_{y,cm} = \frac{3M}{80\sigma^2}\left[4\sigma\left(R_S{}^2\sigma + R_S R_B + R_B{}^2\right) + L^2\left(\mu^4 + 4\mu^3 + 10\mu^2 + 4\mu + 1\right)\right]$$

and

$$I_{z,cm} = \frac{3M}{10\sigma}\left(R_S{}^2\sigma + R_S R_B + R_B{}^2\right)$$

where the variables are as follows:

M = the segment mass (kg)

L = the segment length (m)

R_S = the small radius of the segment (m)

R_B = the big radius of the segment (m)

μ = the ratio of the small radius and the big radius

$\sigma = 1 + \mu + \mu^2$

APPENDIX B

OBTAINING THE CLOSEST ROTATION MATRIX FOR RIGID BODY MOVEMENT

Finding the *closest* rotation matrix, R, which will rotate a given segment's local marker data at time t onto its local marker positions at time $t+1$, involves solving a least-squares problem. Basically, the error between the local marker data at time $t+1$ and the rotated, time-t local marker data should be minimal (Arun, Huang, and Blostein 1987). Define the local i^{th}-marker data $\vec{y}^{\,i}{}_j = \vec{x}^{\,i}{}_j - \vec{x}_{cm,j}$, where $\vec{x}^{\,i}{}_j$ is a column vector of the i^{th} marker's VICON data at time j and $\vec{x}_{cm,j}$ is a column vector of the location of the center of mass (calculated from VICON data) at time j. Then the square of this error, Σ^2, is given by $\sum_{i=1}^{m} \left\| \vec{y}^{\,i}{}_{t+1} - R\vec{y}^{\,i}{}_t \right\|^2$, where m represents the number of markers on the segment. The goal is now to find R such that Σ^2 is minimal.

To begin this search, expand Σ^2 as follows:

$$\begin{aligned}
\Sigma^2 &= \sum_{i=1}^{m} \left(\vec{y}^{\,i}{}_{t+1} - R\vec{y}^{\,i}{}_t \right)^T \left(\vec{y}^{\,i}{}_{t+1} - R\vec{y}^{\,i}{}_t \right) \\
&= \sum_{i=1}^{m} \left(\vec{y}^{\,i}{}_{t+1}{}^T \vec{y}^{\,i}{}_{t+1} - \vec{y}^{\,i}{}_{t+1}{}^T R\vec{y}^{\,i}{}_t - \vec{y}^{\,i}{}_t{}^T R^T \vec{y}^{\,i}{}_{t+1} + \vec{y}^{\,i}{}_t{}^T R^T R\vec{y}^{\,i}{}_t \right) \\
&= \sum_{i=1}^{m} \left(\vec{y}^{\,i}{}_{t+1}{}^T \vec{y}^{\,i}{}_{t+1} + \vec{y}^{\,i}{}_t{}^T \vec{y}^{\,i}{}_t - 2\vec{y}^{\,i}{}_t{}^T R^T \vec{y}^{\,i}{}_{t+1} \right)
\end{aligned}$$

The last step follows from the fact that R is a rotation matrix, and therefore orthogonal (so that R^TR is the identity matrix), and because $\vec{y}^{\,i}{}_{t+1}{}^T R\vec{y}^{\,i}{}_t = \vec{y}^{\,i}{}_t{}^T R^T \vec{y}^{\,i}{}_{t+1}$

since each term is a scalar and a scalar's transpose is itself. Therefore, in order for Σ^2 to be minimal, the scalar quantity $\sum_{i=1}^{m} \bar{y}^i{}_t{}^T R^T \bar{y}^i{}_{t+1}$ should be maximal.

By using the fact that if a is a row vector and b is a column vector, then ab = $trace(ba)$ and by defining the matrix $C = \sum_{i=1}^{m} \bar{y}^i{}_{t+1} \bar{y}^i{}_t{}^T$, it follows that

$\sum_{i=1}^{m} \bar{y}^i{}_t{}^T R^T \bar{y}^i{}_{t+1} = trace\left(\sum_{i=1}^{m} R^T \bar{y}^i{}_{t+1} \bar{y}^i{}_t{}^T\right) = trace\left(R^T C\right)$. Since every matrix has a singular value decomposition, let the singular value decomposition of C be $P\Gamma Q^T$, where P and Q are orthogonal matrices and Γ is a diagonal matrix. Let the sought rotation matrix, R, be set equal to the product PQ^T. Note that R is orthogonal. Then the following reasoning will show that $trace\left(R^T C\right) = trace\left(QP^T P\Gamma Q^T\right) = trace\left(Q\Gamma Q^T\right)$ is maximal:

Set A equal to $Q\Lambda Q^T$ so that $AA^T = Q\Lambda Q^T Q\Lambda^T Q^T = Q\Gamma Q^T$, where Γ is $\Lambda\Lambda^T$. Then AA^T is positive definite. If a_i represents the i^{th} column of A and B is any orthogonal matrix of the same size as A, then $trace\left(AA^T\right) \geq trace\left(BAA^T\right)$ because

$trace\left(BAA^T\right) = trace\left(A^T BA\right) = \sum_i a_i{}^T \left(Ba_i\right) \leq \sum_i \left(\sqrt{a_i{}^T a_i}\sqrt{a_i{}^T B^T Ba_i}\right)$
$= \sum_i a_i{}^T a_i = trace\left(AA^T\right)$, where the inequality step above is justified by the Schwarz Inequality.

Thus, $trace\left(AA^T\right) = trace\left(Q\Gamma Q^T\right) = trace\left(R^T C\right)$ is maximal. If the determinant of R is +1, then it is a rotation and so choosing $R = PQ^T$ gives the *closest* rotation matrix for the rigid body rotation.

REFERENCES

Arun, K. S., T. S. Huang, and S. D. Blostein. 1987. "Least-Squares Fitting of Two 3-D Point Sets." *IEEE Trans. Pat. Anal. Mach. Intel.* PAMI-9: 698-700.

Asato, K. T., R. A. Cooper, R. N. Robertson, and J. F. Ster. 1993. "SMART Wheels: Development and Testing of a System for Measuring Manual Wheelchair Propulsion Dynamics." *IEEE Trans. Biomed. Eng.* 40:1320-1324.

Beckett, R., and K. Chang. 1968. "An evaluation of the kinematics of gait by minimum energy." *J. Biomech.* 1: 147-159.

Boninger, Michael L., Rory A. Cooper, Rick N. Robertson, and Thomas E. Rudy. 1997. "Wrist Biomechanics During Two Speeds of Wheelchair Propulsion: An Analysis Using a Local Coordinate System." *Arch. Phys. Med. Rehab.* 78: 364-371.

Choi, Tae Ho. 1997. "Development of a Mathematical Model of Gait Dynamics." Dissertation New Jersey Institute of Technology.

Cooper, Rory A. 1990. "A Systems Approach to the Modeling of Racing Wheelchair Propulsion." *J. Rehab. Res. Dev.* 27: 151-162.

Cooper, Rory A. 1990. "A Force/Energy Optimization Model for Wheelchair Athletics." *IEEE Trans. Sys. Man Cyber.* 20: 444-449.

Coutts, Kenneth D. 1990. "Kinematics of Sport Wheelchair Propulsion." *J. Rehab. Res. Dev.* 27: 21-26.

Dempster, W. T. 1955. "Space Requirements of the Seated Operator." *WADC Tech. Rept.* Wright-Patterson Air Force Base, Ohio. 55-159.

Goldstein, Herbert. 1980. *Classical Mechanics.* 2nd ed. Massachusetts: Addison Wesley.

Grood, E. S., and W. J. Suntay. 1983. "A Joint Coordinate System for the Clinical Description of Three-Dimensional Motions: Application to the Knee." *Trans. A.S.M.E.* 105: 136-144.

Hatze, H. 1977. "A complete set of control equations of the human musculo-skeletal system." *J. Biomech.* 10: 799-805.

Higgs, C. 1984. "Propulsion of racing wheelchairs." *Sports and Disabled Athletes.* C. Sherill, ed. Illinois: Human Kinetics. 165-172.

REFERENCES
(continued)

Hofstad, Michael, and Patrick E. Patterson. 1994. "Modelling the Propulsion Characteristics of a Standard Wheelchair." *J. Rehab. Res. Dev.* 31: 129-137.

Kuc, Roman. 1988. *Introduction to Digital Signal Processing.* New York: McGraw Hill.

Lacker, H. M., T. H. Choi, S. Schenk, B. Gupta, R. P. Narcessian, S. A. Sisto, S. Massood, J. Redling, P. Engler, F. Ghobadi, V. K. McInerney. 1997. Abstract: "A Mathematical Model of Human Gait Dynamics." *Gait & Posture.* 5: 176.

Mansour, J. M., M. D. Lesh, M. D. Nowak, and S. R. Simon. 1982. "A Three Dimensional Multi-Segmental Analysis of the Energetics of Normal and Pathological Human Gait." *J. Biomech.* 15: 51-59.

Mochon, S., and T. A. McMahon. 1980. "Ballistic walking." *J. Biomech.* 13: 49-57.

Nordin, Margareta, and Victor H. Frankel. 1989. *Basic Biomechanics of the Musculoskeletal System.* 2nd ed. Philadelphia: Lea & Febiger.

Press, William H., Saul A. Teukolsky, William T. Vetterling, and Brian P. Flannery. 1992. *Numerical Recipes in FORTRAN: The Art of Scientific Computing.* 2nd ed. New York: Cambridge University Press.

Rao, Sreesha S., Ernest L. Bontrager, JoAnne K. Gronley, Craig J. Newsam, and Jacquelin Perry. 1996. "Three-Dimensional Kinematics of Wheelchair Propulsion." *IEEE Trans. Rehab. Eng.* 4:152-159.

Ridgway, M., C. Pope, and J. Wilkerson. 1988. "A Kinematics Analysis of 800-meter Wheelchair Racing Techniques." *Adap. Phys. Act. Q.* 5: 96-107.

Robertson, Rick N., Michael L. Boninger, Rory A. Cooper, and Sean D. Shimada. 1996. "Pushrim Forces and Joint Kinetics During Wheelchair Propulsion." *Arch. Phys. Med. Rehab.* 77: 856-864.

Rodgers, M. M., S. Tummarakota, J. Lieh, and D. R. Schrag. 1994. Abstract: "Three-Dimensional Dynamic Analysis of Joint Reaction Forces and Moments During Wheelchair Propulsion." *Clin. Kinesiology.* Wint' 94: 98.

Ruggles, Deborah L., Thomas Cahalan, and Kai-Nan An. 1994. "Biomechanics of Wheelchair Propulsion by Able-Bodied Subjects." *Arch. Phys. Med. Rehab.* 75: 540-544.

REFERENCES
(continued)

Sanderson, David J., and H. J. Sommer III. 1985. "Kinematic Features of Wheelchair Propulsion." *J. Biomech.* 18: 423-429.

Schenk, S., W. Roman, R. Narcessian, M. Lacker, J. Redling, S. A. Sisto, and M. Gerdes. 1998. Abstract: "Mechanical Energy Efficiency of a Wheelchair Racing Stroke." *Gait & Posture*. 7: 152.

Seireg, A., and R. Arvikar. 1989. *Biomechanical Analysis of the Musculoskeletal Structure for Medicine and Sports*. New York: Hemisphere Publishing Corporation.

Shimada, Sean D., Rick N. Robertson, Michael L. Bonninger, and Roray A. Cooper. 1998. "Kinematic Characterization of Wheelchair Propulsion." *J. Rehab. Res. Dev.* 35: 210-218.

Siegler S., R. Seliktar, and W. Hyman. 1982. "Simulation of human gait with the aid of a simple mechanical model." *J. Biomech.* 15: 415-425.

Söderkvist, Inge, and Per-Åke Wedin. 1993. "Determining the Movements of the Skeleton Using Well-Configured Markers." *J. Biomech.* 26: 1473-1477.

Strang, Gilbert. 1988. *Linear Algebra and Its Applications*. 3rd ed. New York: Saunders College Publishing, Harcourt Brace Jovanovich College Publishers.

van der Woude, L. H. V., H. E. J. Veeger, R. H. Rozendal, G. J. van Ingen Schenau, F. Rooth, and P. van Nierop. 1988. "Wheelchair Racing: Effects of Rim Diameter and Speed on Physiology and Technique." *Med. Sci. Sports Exer.* 20: 492-500.

van der Woude, L. H. V., H. E. J. Veeger, and R. H. Rozendal. 1989. "Propulsion Technique in Hand Rim Wheelchair Ambulation." *J. Med. Eng. Tech.* 13: 136-141.

Vanlandewijck, Yves C., Arthur J. Spaepen, and Roeland J. Lysens. 1994. "Wheelchair Propulsion Efficiency: Movement Pattern Adaptations to Speed Changes." *Med. Sci. Sports Exer.* 26: 1373-1381.

Vaughan, Christopher L., Brian L. Davis, and Jeremy C. O'Connor. 1992. *Dynamics of Human Gait*. Illinois: Human Kinetics Publishers.

Veeger, H. E. J., L. H. V. van der Woude, and R. H. Rozendal. 1989. "Wheelchair Propulsion Technique at Different Speeds." *Scan. J. Rehab. Med.* 21:197-203.

REFERENCES
(continued)

VICON 370 Version 2.5 User's Manual. 1998. Oxford: Oxford Metrics Limited.

Wang, Yong Tai, Helga Deutsch, Martin Mose, Brad Hedrick, and Tim Millikan. 1995. "Three-Dimensional Kinematics of Wheelchair Propulsion Across Racing Speeds." *Adap. Phys. Act. Q.* 12: 78-89.

Wells, Dare A. 1967. *Schaum's Outline Series: Theory and Problems of Lagrangian Dynamics*. New York: McGraw-Hill Book Company.

Winter, D. A. 1984. "Biomechanics of Human Movement with Applications to the Study of Human Locomotion." *CRC Crit. Rev. Biomed. Eng.* 9:287-314.